UNIVERSITY OF OKLAHOMA

GRADUATE COLLEGE

MAGNETOSTRATIGRAPHY OF THE PRE-COLORADO RIVER INTEGRATION LOST CABIN BEDS, COTTONWOOD VALLEY, ARIZONA

A THESIS

SUBMITTED TO THE GRADUATE FACULTY

in partial fulfillment of the requirements for the

Degree of

MASTER OF SCIENCE

By

JONATHAN SCHWING
Norman, Oklahoma
2019

MAGNETOSTRATIGRAPHY OF THE PRE-COLORADO RIVER INTEGRATION LOST CABIN BEDS, COTTONWOOD VALLEY, ARIZONA

A THESIS APPROVED FOR THE
CONOCOPHILLIPS SCHOOL OF GEOLOGY AND GEOPHYSICS

BY

Dr.Shannon Dulin, Chair

Dr. Gerilyn S. Soreghan

Dr. R. Douglas Elmore

ACKNOWLEDGEMENTS

I would like to acknowledge my thesis committee who have helped me through the revisions of this thesis. Special thanks to my advisor Dr. Shannon Dulin for providing me with direction, guidance, and encouragement throughout my research. Fellow graduate student Ian Tran was a super helpful field partner, assisting with the collection of the samples from this study. Not to mention, some great campfire dinners! Thank you to the University of Oklahoma's School of Geology & Geophysics for providing tuition waivers and TA funding over the past couple years.

A big thanks to the members of the United States Geological Survey's Flagstaff AZ team for all the help you have provided over the past couple years. A special thank you to Dr. Ryan Crow for always being willing to help me with fieldwork, sample collection, and for all the advice you've provided with this project. Additionally, I would like to thank you Mark Stelton and the U.S.G.S. Menlo Park office for processing and $^{40}Ar/^{39}Ar$ dating all the sanidine samples for my thesis. Thank you to Kai Smith-Crain for assisting with the crushing/sieving and acid treatment of Lost Cabin Wash ash samples.

An enormous thank you to my lovely wife Chrissy. Between your loving support and help with the multiple iterations of thesis revisions, you have kept me grounded throughout this process. Thank you for always encouraging me to continually work hard and put my best foot forward. Throughout the last 2 years we have started a life together and I can't wait to see what the next chapter holds. You are my rock. I love you! Last but not least... Thanks to my pups Elsa and Lily for always excitedly greeting me at the door no matter how stressful the day was.

Table of Contents

LIST OF TABLES

LIST OF FIGURES

ABSTRACT

The Miocene Lost Cabin beds of Cottonwood Valley, Arizona, represent a north-northeasterly fine-grained axial valley basin deposit fed by sediments from the Newberry and Black Mountains to the west and east, respectively. Cottonwood Valley formed within the Colorado River corridor during a period of volcanism and north moving E-W extension spanning the early to middle Miocene. This study uses magnetostratigraphy, rock magnetism, and $^{40}Ar/^{39}Ar$ dating from detrital sanidine to determine the timing of deposition of the Lost Cabin beds in relation to the arrival of Colorado River sediments. One hundred and seventy samples were used in this study from a total of thirty-nine sites. Magnetite and hematite are identified as predominate carriers of magnetic remanence, with minor contributions from titanomagnetite, titanomaghemite, and pyrrhotite. Rock magnetic measurements were consistent with identifying magnetizations that are held in magnetite and hematite. Normal and reverse polarities yielded a total of three geomagnetic polarity intervals within the Lost Cabin bed sediments. $^{40}Ar/^{39}Ar$ dating yielded one site with a young sanidine grain that produced an age of 5.49 ± 0.788 Ma. Magnetostratigraphy was correlated to the geomagnetic polarity timescale by using three ash beds with dates that spanned from 5.59 ± 0.05 Ma to 5.35 ± 0.07 Ma. Polarity intervals were identified as Subchrons C3r, and C3n.4n (Thvera), within the Gilbert Chron. Results from this study suggest a post 5.235 Ma arrival date of the Colorado River waters within Cottonwood Valley.

INTRODUCTION

The timing and depositional models of the Colorado River integration have historically been a topic of debate. Early Colorado River deposits were first described by Metzger (1968) and are observed throughout the Colorado River corridor as a basal carbonate, which is formally named the Bouse Marl. Proposed depositional models vary from purely lacustrine deposition (Spencer & Patchett, 1997; House et al., 2008; Pearthree & House, 2014) to an estuarian model in which lacustrine/fluvial waters meet an estuary in the southern Blythe Basin (Miranda-Martinez et al., 2017; McDougall & Miranda-Martinez, 2014; McDougall, 2008) (Fig. 1). Most models agree that upstream Bouse Marl deposits record a time during which Colorado River waters filled Basin and Range valleys separated by high elevation paleo divides, before spilling over in a cascading manner to downstream valleys (House et al., 2008). Early Colorado River integration would have followed a similar westerly direction to the modern river through the Grand Canyon, before making a sharp turn to the south past modern-day Lake Mead. The early Colorado River waters would have continued filling and spilling into valleys from north to south in the following manner: Cottonwood Valley (CV), Mohave Valley, Chemehuevi Valley, Blythe Basin, and eventually to the Fish Creek-Vallecito Basin of the Salton Trough in California (Fig. 1).

It is important to understand the timing of deposition, in order to further refine the mechanisms and timing of Colorado River integration. Previous geochronological work in the lower Colorado River corridor's Blythe Basin has produced contradictory results regarding the exact arrival of Colorado River sediments. The work of Sarna-Wojcicki et al. (2011) and Harvey (2014) used tephrochronology to date an ash bed intercalated with Bouse Marls, suggesting Colorado River waters arrived by 4.83 Ma. Dorsey et al. (2011) used magnetostratigraphy and

sedimentology of the southernmost Colorado River basin (Fish Creek-Vallecito; (Fig. 1)), to suggest that the Colorado River had integrated to the Salton Trough terminus by 5.23 Ma.

To resolve this discrepancy in integration timing, this study conducts a magnetostratigraphic study of an upper Colorado River corridor site found upstream within Cottonwood Valley (CV; Fig. 1). The Miocene Lost Cabin beds in CV, AZ, contain abundant ash beds and flat lying fine-grained sediments, which is ideal for a magnetostratigraphic study. Mapped stratigraphic relationships documented in the CV show Bouse Marl sediments overlying Lost Cabin beds, suggesting that deposition of the Lost Cabin beds pre-date the inception of Colorado River development, and thus provide a lower constraint on the timing of northern basin fluvial integration. Two ash beds within the Lost Cabin beds have yielded ages of 5.59 ± 0.05 Ma and 5.35 ± 0.07 Ma from tephrochronology and sanidine $^{40}Ar/^{39}Ar$ single-grain analysis, respectively (House et al., 2008; Crow, 2018). Paleomagnetism in this study is used to compare geomagnetic polarity within Lost Cabin bed sediments against documented Geomagnetic Polarity Timescale (GPTS) polarity chrons. Absolute dates provided from previously dated ash beds which both lie with the Cr3 reverse-polarity subchron of the Gilbert chron will be used to provide boundaries for GPTS polarity. If paleomagnetism reveals Lost Cabin bed sediments to have reverse polarity within the boundaries of 5.59 ± 0.05 Ma to 5.35 ± 0.07 Ma and a reverse to normal transition was captured above, it would further suggest that Lost Cabin bed sediments were deposited in the late Miocene throughout the 5.235 Ma reversal between the C3r and C3n.4n (Thvera) subchrons. This suggests that Colorado River fluvial integration in the upstream northern corridor would not have commenced until after 5.235 Ma.

2 BACKGROUND

2.1 GEOLOGY OF COTTONWOOD VALLEY

Modern-day Cottonwood Valley (CV) forms a north to north-west trending axial valley along the Colorado River's extensional corridor between the borders of Nevada and Arizona. This study's field area is concentrated in the southern CV along Lake Mohave, bound by the detachment fault controlled granitic Newberry Mountains to the west and the westerly dipping volcanic and sedimentary succession of the Black Mountains accommodation zone to the east (Faulds et al., 2001). The CV basin formed during a period of widespread regional east-west crustal extension that lasted from 23 to 11 Ma, with peak extension occurring from 16.5 – 15.5 Ma (Simpson et al., 1991; Faulds et al., 1999). Volcanic sediments within CV were dated using $^{40}Ar/^{39}Ar$, bracketing localized extension between 16.2 and 11 Ma (Faulds et al., 1995). This early to middle Miocene period of east-west extensional tectonics was coeval with volcanism that followed the northern trend of crustal extension. Major episodes of localized Miocene tephra ash falls in the CV include the 18.5 Ma Peach Springs Tuff (Glazner et al., 1986; Nielson et al., 1990), the 15.2 Ma tuff of Bridge Spring (Anderson et al., 1972; Morikawa, 1994; Faulds et al., 1995) , and the 15.0 Ma tuff of Mount Davis (Faulds & Bell, 1999; Faulds et al., 2001). These early to middle Miocene volcanic sediments provide the surrounding bedrock within CV and are important in dating lower constraints to Colorado River integration.

The Lost Cabin beds within the CV are an informally named sedimentary succession first identified by House et al. (2008), that prior to this study, had not been formally described in detail. The Lost Cabin beds are interpreted as a late Miocene enclosed basin axial-valley fill deposit with sediments fed from the Newberry Mountain fan system to the west and the Black Mountain fan system to the east (Fig. 2) (House et al., 2008). Mapped deposits of lower coarse-

grained Lost Cabin bed sediments lie unconformably on top of tilted early to middle Miocene fanglomerates and interfinger with granitic material from the Newberry Mountain fanglomerates. The upper Lost Cabin beds grade upward to finer-grained facies of sandstones, siltstones, and mudstones, before laterally interbedding with the coarse-grained sediments of the Black Mountain fanglomerate (House et al., 2008).

Lost Cabin beds within the CV are stratigraphically overlain by basal marl and siliciclastic sediments of the Pliocene Bouse Formation (Fig. 3) (Metzger, 1968). The Bouse Formation signals the first sign of a through flowing Colorado River (Spencer & Patchett, 1997), and is understood to represent a cascading lacustrine system that flooded and spilled into subsequent downstream basins as the waters continued to the Gulf of California (House et al., 2008). Following the draining of the (~550 m above sea level) paleo-Lake Mohave, abrupt changes in depositional baseline resulted in progradation of post-Bouse Black Mountain Fanglomerate deposits, which cover much of the Lost Cabin bed and Bouse sediments in this study area (Fig. 4).

2.2 PREVIOUS GEOCHRONOLOGICAL STUDIES

The timing of the first signs of upstream Colorado River integration have been previously bracketed by the studies of Spencer at al. (2001) and Faulds et al. (2016). The Hualapai limestone to the north of the CV near modern day Lake Mead is interbedded with a tuff which yielded a $^{40}Ar/^{39}Ar$ biotite age of 5.97 ± 0.07 Ma at 2σ uncertainty (Spencer at al., 2001). The Hualapai limestone predates clastic/gravel input of an integrated Colorado River. Slightly farther upstream, a basalt flow at Sandy Point within the Grand Wash Trough overlies Colorado River gravel and yielded an $^{40}Ar/^{39}Ar$ age of 4.49 ± 0.23 Ma (Faulds et al., 2016). These studies

indicate that first arrival of the Colorado River in the northern most basins and Grand Wash Trough is bracketed between 6 Ma (Hualapai LS) and 4.5 Ma (Sandy Point Basalt).

The next depositional basin south of the Grand Wash Trough/Lake Mead area is Cottonwood Valley (CV). Within the CV the Lost Cabin beds contain Miocene ash beds in the ~100 m of exposed section, two of which have been dated at 5.59 ± 0.05 Ma and 5.35 ± 0.07 Ma via glass shard tephrochronology and sanidine $^{40}Ar/^{39}Ar$ young grain analysis, respectively (House et al., 2008). The 5.59 ash was identified as the Wolverine Creek Tuff, an ash fall correlated to the Yellowstone-Snake River Plain hotspot track. The Wolverine/Conant Creek Tuff has been identified interbedded with the Hualapai Limestone to the north, indicating coeval sedimentation of the Lost Cabin beds and Hualapai Limestone (Faulds et al., 2016). Colorado River waters would continue southward, filling and spilling into Mohave Valley, Chemehuevi Valley, and the greater Blythe basin, sequentially.

South of the CV, within the Blythe Basin, Bouse Marl deposits are interbedded with coeval ash beds at Amboy and Buzzards Peak. These ash beds are geochemically correlated via glass tephrochronology with the 4.83 ± 0.011 Ma Lawlor Tuff, which erupted from the northern San Francisco Bay Area (Sarna-Wojcicki et al., 2011). Additionally, comparative zircon tephrochronology confirmed a correlation between the ash and the 4.83Ma Lawlor Tuff (Harvey, 2014). These dates suggest that Colorado River waters were filling lower corridor basins by ~4.8 Ma; and that Colorado River sands would not reach the Salton Trough terminus until post 4.80 Ma, when all paleo-lakes were drained and replaced by the through flowing Colorado River fluvial system (Spencer et al., 2013).

Within the Salton Trough, the Wind Caves Member of the Latrania Formation, is linked to Colorado River sediment based on petrographic similarities between the Wind Caves and

Colorado River zircon and sand grains (Dorsey et al., 2011). Two overlying tuff beds from the overlying Tapiado Formation were dated at 2.60 ± 0.06 Ma and 2.65 ± 0.05 Ma by high resolution U-Pb isotopic analysis of 35 individual zircon grains (Dorsey et al., 2011). Two paleomagnetic studies were used to map the magnetostratigraphy of nearly 5km of stratigraphic section encompassing the Tapiado/Hueso Formations down to the Wind Caves Member of the Latrania Formation (Opdyke at al., 1977; Dorsey et al., 2011). The lower section of the Wind Caves was identified as being within a reverse polarity zone that correlates to the Cr3 subchron (5.23 – 5.89 Ma), from Candle and Kent (1995). This clastic arrival date presents a discrepancy with previous geochronologic dating from Sarna-Wojcicki et al. (2011) and Harvey (2014), which places pre-clastic Colorado River water arrival dates at ~4.8 Ma.

3 METHODS

3.1 FIELD SAMPLING METHODS

Primary magnetostratigraphic sample collection was conducted in January 2018, along a southern wall exposure of Lost Cabin beds within the Lost Cabin Wash (Fig. 5). Paleomagnetic sampling locations were spaced at 1 m vertical intervals within the fine-grained facies, with increased sampling density near ash beds, which provide absolute dating constraints for comparison of magnetic polarity data. The southern wall of the Lost Cabin beds was measured with a 1.5 m Jacob's staff, and logged in detail. Latitude and longitude coordinates for all paleomagnetic samples, ash beds, and sediment samples were logged using a handheld Garmin GPS. A Trimble high-precision GPS was used for elevations at key sites. Samples were collected using both hand-oriented blocks, and a portable gas-powered chainsaw modified with a Pomeroy coring device. A Brunton compass was used to orient block samples and a Pomeroy orienting fixture was used to orient cores. Due to the poor lithification of sediments, most samples were

collected as oriented blocks. Additionally, samples were collected within fine-grained mudstones and siltstones, in sections that did not contain cross-beds and/or large clasts.

Additional sites were collected in January 2019 to infill sample sites within the Lost Cabin Wash magnetostratigraphic section and to expand the sampling coverage to proximal wash systems containing dated ash beds and Bouse-aged sediments. These sample sites include the Wolverine Creek ash site, the High Wall Wash ash site, the Golden Section, and the Bouse Incision site located on the north wall of Lost Cabin Wash (Fig. 5). Sampling at the new locations was completed at a 0.1 to 0.5 m vertical resolution, collecting oriented blocks above and below ash deposits to provide a fine scale mapping of stratigraphic polarity.

3.2 PALEOMAGNETISM

3.2.1 SAMPLE PREPARATION

Owing to the friable nature of the sediment, special care was taken to cut the block samples into usable specimens. A band saw with a demagnetized steel blade was used for rough cutting the oriented blocks, and a belt sander was used for final shaping of samples. All specimens were cut into standard (~2.5 cm) cubes for subsequent paleomagnetic analysis.

To ensure that samples would remain intact though the full measure of thermal steps to 700° C, samples were coated with a 50:50 mix of kaolin powder and sodium silicate solution before thermal demagnetization.

3.2.2 DEMAGNETIZATION

Natural remanent magnetizations (NRMs) were measured using a 2G-Enterprises cryogenic magnetometer with DC squids in the shielded paleomagnetic laboratory at the University of Oklahoma. Prior to thermal and/or alternating field (AF) demagnetization, 69 of the 195 samples were subjected to low-temperature demagnetization (LTD). The samples were

submerged in liquid nitrogen, allowed to warm to room temperature in a zero-field room, measured for NRM, then re-submerged in liquid nitrogen a total of three times to aid in the removal of unstable remanence from multi-domain (MD) grains (Dunlop and Argyle, 1991). Alternating field demagnetization consisted of 12 steps (10 mT each) from 10 mT to 120 mT. Thermal demagnetization subjected samples to a total 20 steps, with 100°C steps from 100° to 300° C, and 25 steps from 325° to 700° C.

Magnetization components from all sites were determined using orthogonal vector projections (Zijderveld 1967) and equal area projections. Super IAPD (http://www.geodynamics .no/resources.html) was also used for principal component analysis (PCA) (Kirschvink, 1980) to determine magnetic components. Site means were performed in Super IAPD utilizing Fisher statistics of specimens and site means (Fisher, 1953).

3.2.3 ELONGATION / INCLINATION ANALYSIS

The inclination shallowing module of paleomagnetism.org (Koymans et al., 2016) and Mark Hounslow's PMagTool software (https://www.lancaster.ac.uk/ staff/hounslow/resources /software/pmagtool.htm) was used to correct for shallowed characteristic remanent magnetization (ChRM) inclinations that can occur in compacted sedimentary rocks (Tauxe and Kent, 2004). For a given set of inclinations/declinations, the module calculates the elongation parameter ($\tau 2/\tau 3$) of the orientation matrix. After sample inclination values are entered in the program, the module calculates if the actual elongation is lower than the expected elongation as described by the TK03.GAD field model (Tauxe and Kent, 2004; Tauxe et al., 2008; Koymans et al., 2016). If the inclination value is found to be lower than expected, the flattening function of King (1955) is applied to unflatten the inclination to a maximum factor of 0.2. This procedure is completed by computing 5000 non-parametric bootstraps and continued iteratively until an intersection with

the TK03-GAD field model is found (Koymans et al., 2016). The procedure was completed separately for normal and reversed polarity ChRM components, creating distinct unflattened components with associated α_{95} values. Reversed polarity samples were then flipped to their antipode and bootstrapped with the normal components to provide an inclination mean with associated α_{95} boundaries. By bootstrapping normal and reverse components together, the program creates an artificial elongation that effectively corrects shallowed inclination values. The mean value of the antipodal total site inclination was then compared with the α_{95} values of the normal and reversed bootstraps to ensure that it plotted within the acceptable boundaries.

3.2.4 REVERSAL TEST

A reversal test was completed on a total of 59 normal and 110 reverse polarity ChRM components by using the reversal test module of Mark Hounslow's PMAGTOOL program, after the methods of (McFadden & McElhinny, 1990). This reversal test works by examining the critical angle (95% c.i.) between two sample mean directions to determine rejection. A positive reversal test is classified as 'Ra' if the γ_c (critical angle) is $\leq 5°$, 'Rb' is $5° < \gamma_c \leq 10°$, 'Rc' if $10° \leq \gamma_c \leq 20°$, and 'Ro' (indeterminate) if $\gamma_c > 20°$. The attribute 'R-' is used to indicate a negative reversal test (McFadden & McElhinny, 1990). The mean reversed polarity of the ChRM was flipped to its antipode to ensure that the α_{95} values of the mean directions overlapped.

3.3 ROCK MAGNETISM

3.3.1 ISOTHERMAL REMANENT MAGNETIZATION (IRM)

To determine the magnetic mineralogy of key sample lithologies, isothermal remanent magnetization (IRM) acquisition was performed using an ASC Scientific Impulse Magnetometer at the University of Oklahoma. An IRM is acquired by first demagnetizing the samples, then applying an increasing magnetic field in a stepwise manner along the z-axis of a specimen. This

was completed by first demagnetizing all samples at 120 mT using an AF degaussing system, then measuring individual NRMs. The samples were then subjected to 30 steps of increasing IRM acquisition from 10 to 2500 mT using the following scheme (0, 10, 15, 20, 25, 30, 35, 40, 50, 60, 70, 80, 100, 110, 125, 140, 150, 175, 200, 250, 350, 400, 500, 750, 1000, 1250, 1500, 1750, 2000, 2250, 2500 mT). Acquisition curves were built by plotting magnetization vs. acquisition steps in EXCEL. The acquisition curve shapes of specimen IRMs depends on the coercivities of magnetic carriers within the sample, which is used to infer magnetic mineralogy.

3.3.2 LOWRIE METHOD / TRIAXIAL DECAY

After samples were subjected to IRM analysis, they were demagnetized by applying a 120 mT field within the AF degausser. Following the Lowrie method (Lowrie, 1990), IRMs were imparted on samples in three mutually orthogonal directions (X, Y, Z) at 120, 500, and 2500 mT, respectively. The NRMs were then measured and samples were subsequently thermally demagnetized in a stepwise manner from 100° to 700° C. The Lowrie method is used to interpret mineralogy by subdividing the remanence carrying minerals within a specimen by hard, medium, and soft coercivities. The coercivity data are then combined with thermal unblocking temperatures, yielding insights to magnetic mineralogy.

3.3.3 OPTICAL MICROSCOPY AND S.E.M. ANALYSIS

Petrographic analysis was conducted on 10 thin sections from the Lost Cabin Wash section and the Bouse Marl site. Transmitted and reflected light microscopy was conducted using the Zeiss Axio Imager.Z1 petrographic microscope. This was completed to investigate detrital vs. authigenic magnetic carriers, and to investigate and mark the locations of opaque minerals for subsequent detailed scanning electron microscope (SEM) analysis.

A total of 4 thin sections from the Lost Cabin Wash (LCW) section and 2 stubs with loose grains of detrital ash from the High Wall Wash site (HWW) were analyzed using the FEI Quanta 250 SEM equipped with a Bruker XFlash 6I100 x-ray detector (EDX). Samples were first sputter coated with a gold/palladium alloy to prevent sample charging before being placed in the SEM. Opaque grains identified using the Zeiss reflected light microscope were systematically photographed and mapped with the EDX, which allowed mineralogy to be inferred based on elemental composition. All grains below the resolution of conventional light microscopy were photographed and analyzed using SEM and EDX.

3.4 SANIDINE Ar^{40}/Ar^{39} ASH DATING

3.4.1 ASH PULVERIZATION AND SIEVING

Ash samples were prepared with the assistance of the USGS Flagstaff office and Northern Arizona University. The goal was to isolate the sanidine fraction from the detrital population to then irradiate and determine radioactive age, therefore providing anchor ages for magnetostratigraphy. Samples were crushed into a fine powder using a clean mortar and pestle. The samples were then placed into separate bags labeled in the following format: SampleNumber//YYYYMMDD//# - Last Procedure Performed.

Samples were placed into sieves that were arranged according to mesh size (ex: >20µ, 20-40µ, 40-60µ, 60-120µ, <120µ). Once samples had been properly distributed to the allotted mesh size, they were placed into bags labeled in the following format: SampleNumber//YYYYMMDD//# - Mesh Size.

3.4.2 HF AND HCL ETCHING

Crushed and sieved samples were placed into a clean glass beaker, filled with DI water, and placed into an ultrasonic bath for 5 to 10 minutes. Water was then decanted from the beaker

and the sample was placed under a fume hood before pouring a 15% solution HCL in the beaker until samples were submerged. Samples were then subjected to an ultrasonic bath for 5 to 10 minutes, or until a reaction stopped with ash.

The sample was then transferred to a plastic beaker using a DI spray bottle before having the water decanted off to HCL waste. A 5% solution HF was carefully poured into a beaker until samples were submerged. Then the beaker was placed into an ultrasonic bath for 5 to 10 minutes. Samples were then placed into a glass beaker and washed with DI water three times to remove HF solution. The samples were then transferred to a final beaker, filled with DI water, and placed for 5 minutes in an ultrasonic bath for 2 to 3 times. Acetone spray was then used to rinse the samples three times, before having the samples sit under a heat lamp to dry. Dried samples were then placed into bags labeled with the following format: SampleNumber//YYYYMMDD//# -- Mesh Size – Procedure.

3.4.3 PICKING AND WASHING

A small amount of ash sample was placed on a glass microscope slide with an equal amount of wintergreen oil was placed onto sample to help distinguish sanidine grains using the Becke line test. Sanidine grains have a yellow Becke line that moves into the wintergreen oil when lowering the stage (Fig. 6a). All grains were examined in cross polarized light (XPL) to make sure that grains went uniformly extinct and displayed no signs of crystal twinning. Polysynthetic twinning in plagioclase grains are problematic for single grain age determination since each twin plane represents distinct parallel crystals. Additionally, plane polarized light (PPL) was used to ensure that grains were free of any major internal defects (Fig. 6b). Internal defects via glass or mineral inclusions can cause error in age determination via single grain

irradiation. All grains that were singled out were placed on clean card stock, using tweezers, and continued until at least 130 grains were collected.

Samples were then moved to a Büchner (vacuum) flask on round filter paper. DI water was added to the flask and sanidine grains were soaked for 15 minutes to remove wintergreen oil. A filtration pump was then turned on to remove DI water from the flask. Samples and filter paper were then removed and transferred to a heat lamp for 5 to 10 minutes until the filter paper was dry. Grains were then taken to a backlit binocular microscope, placed into a small metal capsule, and sealed for final analysis. All finished samples were labeled in the following format: SampleNumber//YYYYMMDD//Aliquot.

3.4.4 ANALYSIS

Ar^{40}/Ar^{39} analysis was performed on a Nu Instruments Noblesse mass spectrometer at the USGS's Menlo Park facility. Argon was removed from single sanidine grains in a single heating step using a New Wave CO_2 laser. All Ar^{40}/Ar^{39} ages were calculated using the decay constants recommended by Steiger and Jäger (1977). Uncertainties in Ar^{40}/Ar^{39} are reported at the 1σ level, and include propagated uncertainties in counting statistics, J values, and correction factors.

3.5 MAGNETOSTRATIGRAPHY

ChRMs were determined utilizing principle component analysis and then classified according to the trend and reliability of demagnetized components. Sites in which the ChRM decayed linearly to the origin were classified as Class "A" data (Fig. 7a). Sites in which the ChRM clustered near the origin were defined as Class "B" data (Fig. 7b). Polarity was interpreted in both Class A and B sites from the inclination of the ChRM, where a negative inclination indicates a reversed polarity and a positive inclination indicates a normal polarity. Polarities that displayed irregular or flipped declination and inclination data were labeled as

ambiguous. Sites that displayed a rapid demagnetization on Zijderveld plots or showed signs of overlapping components were defined as Class "C" data (Fig. 7c). Polarity was determined in these sites using a combination Zijderveld plots, demagnetization curve trends and equal area projections. Sites in which no polarity could be determined due to overlapping components or weak magnetization were defined as Class "D" data (Fig. 7d).

4 RESULTS

4.1 STRATIGRAPHY

The base of Lost Cabin beds within Lost Cabin Wash are interfingered with repeating successions of very poorly sorted mixture of immature granitic and volcanic cobbles sourced from the Newberry Mountains to the west. The cobble-sized grain-supported sections were observed to fine-upwards gradationally to coarse-grained feldspathic litharenites. Fining-upward sequences repeat until 296.3 m above sea level where the first evidence for Lost Cabin beds is observed. The base of the Lost Cabin beds contains a laterally continuous 0.5 m thick variegated mudstone interbedded with a thin ash bed. Abundant vertical burrowing is observed throughout the mudstone layer. The mudstone is overlain by a medium to coarse-grained litharenite. The base of the litharenite exhibits evidence of an erosive contact with the underlying mudstone and contains cross-beds with 50 cm scoria and ash cobbles. In addition to cross-beds, the litharenites are cut by abundant mud and pebble-filled channels. The Lost Cabin beds alternate between erosive litharenite and laterally extensive fine-grained sediments until ~311 m above sea level, where the cross-bedded sedimentary structures give way to planar bedding and abundant iron-oxide coated litharenites, mudcracks, and 0.5 to 3 cm carbonate nodules. A 10 cm laterally extensive soil carbonate layer is observed in both the south and north walls of the Lost Cabin beds within Lost Cabin Wash at 322 m above sea level. The soil carbonate layer is overlain by a

0.5 m reddened paleosol. The paleosols are covered by a repeating succession of coarse to medium-grained litharenites and pebble to cobble sized layers of volcanic material sourced from the Black Mountains to the east. The interfingering of Lost Cabin beds continues before giving way to Black Mountain Fanglomerates at 345 m above sea level. The uppermost level of Lost Cabin beds within Lost Cabin Wash contain erosive fluvial unconformities, filled with green claystones and coarse fanglomerate material.

Outcrops of the Bouse Marl occur throughout CV, with basal elevations ranging from 350 to 550 m above sea level. The marl comprises flat-lying blocky uniform sections of white sandy calcareous mudstone, draping the underlying Black Mountain volcanic fanglomerate deposits. Bouse Marl beds within the study area are devoid of sedimentary structure or trace/fossils. The bulk lithology of Bouse Marls grades upwards to green claystone, with laterally discontinuous sections of fluvially incised beds composed of well-rounded Colorado River quartz arenites with iron-oxide syntaxial overgrowths. Uppermost Bouse sediments featured fractured red mudstones, that were filled with secondary calcite in fracture zones.

The Lost Cabin beds show evidence of an unconformable upper contact within all wash systems. The contact contains a visibly reworked and cross-bedded section of Black Mountain fanglomerate and Lost Cabin bed material, within a carbonate-clay matrix. This reworked section is followed by ~10 to 50 m of high-energy graded deposits of cross and planar bedded fanglomerate, fed from the Black Mountains to the east, as evident by the volcanic lithology.

4.2 PALEOMAGNETISM

4.2.1 SAMPLE SITE VRM/ChRM

The paleomagnetic directions used for this study were estimated by utilizing PCA vector analysis with maximum angular deviations (MADs) that ranged from 1.1° to 15°. Thermal and AF stepwise demagnetization revealed well-defined primary characteristic remanent magnetizations (ChRMs) from a total of 170 samples (111 reverse, and 59 normal) from 39 sites. These sites contain class "A", "B", and "C" quality data (Fig. 7; Table 2). A total of 10 sites were excluded from site-mean direction due to the class "D" unpickable nature of the samples (Fig. 7; Table 2). Thermal unblocking (T_{ub}) ranges for modern viscous remanent magnetizations (VRMs) ranged from 100-200°C and the T_{ub} for ChRMs ranged from 300-700°C. For AF demagnetization unblocking for VRMs ranged from 10-20 mT and ChRMs occurred from 30-90 mT.

A total of 77 specimens were used to determine site mean directions for VRMs. Samples subjected to LTD steps resulted in the Modern component of the magnetization being destroyed due to reorganization of MD magnetite (Dunlop and Argyle, 1991). Site mean directions of the VRM cluster in the northern hemisphere on an equal area projection (Fig. 8a). The VRM was picked to compare with the Modern values and ensure that the ChRM was correctly characterized. The mean VRM direction is Dec.=13.5°, Inc.=59.5°, α_{95}=4.2, N=77, R=72.14, & k=15.64 (Fig. 8b). Site mean directions of ChRM normal polarity directions are shown on an equal area projection (Fig. 9a). The mean ChRM direction is Decl.=10.8°, Incl.=57.2°, α_{95}=5.7, N=59, R=53.94, & k=11.46 (Fig. 10a). Site mean directions of ChRM reverse polarity directions are shown on an equal area projection (Fig. 9a). The mean ChRM direction is Dec.=178°, Inc.=-43.1°, α_{95}=4.3, N=111, R=100.94, & k=10.94 (Fig. 10a). Table 2 contains the site mean directions and Fisher (1953) statistics of all sites used in this paleomagnetic study.

4.2.2 ELONGATION / INCLINATION ANALYSIS

Elongation-inclination analysis was performed on normal and reverse polarity directions to correct for inclination shallowing. Uncorrected inclination values before analysis were 57.2° and -43.1°. Elongation-inclination analysis resulted in a corrected inclination of 56° with an 95% confidence interval of 49° to 64° (Fig. 11). The bootstrapped mean inclinations of standalone reverse and normal paleomagnetic directions (-60.05, 58.77) fall within the boundaries of the combined 95% ci. This confirms that the corrected value for the combined direction is statistically significant, thus inclinations were corrected to 56° for both directions.

4.2.3 REVERSAL TEST

Inclination corrected site means for normal and reverse polarities passed the reversal test using the McFadden and McElhinney (1990) method (Fig. 10b). Direction data used for normal polarity is Dec.=10.8°, Inc.=56°, N=59, α_{95}=5.7 k=11.52. Direction data used for reverse polarity is Dec.=178°, Inc.= -56°, N=111, α_{95}=4.3 k=10.71. The data resulted in a "Rb" classification, with an observed gamma of 7.15 and a critical gamma of 7.18. Additionally, the α_{95} of reverse and normal site means overlapped when the reverse component was flipped to its antipode.

4.3 ROCK MAGNETISM

4.3.1 ISOTHERMAL REMANENT MAGNETIZATION (IRM)

IRM acquisition of 5 Lost Cabin bed samples (LCW0, LCW5, LCW10, LCW15, LCW20) from the Lost Cabin Wash section yielded curves that reached maximum saturation (0.1 – 0.15 mA/M) by 500 mT (Fig. 12). IRM acquisition of Bouse Marl within the Lost Cabin Wash (LCW Marl 2-1B) exhibited a sharp rise to 500 mT (0.00114 mA/M), then continued to increase in saturation to 2500 mT (0.00119 mA/M) (Fig. 13). IRM acquisition of High Wall Ash (HWW 8-1) from the High Wall Wash site yielded a sharp rise to 400 mT (0.0525 mA/M), then continued

to increase in saturation to 2250 mT (0.0548 mA/M) (Fig. 14). IRM acquisition of (WC 4-3) from the Wolverine Creek Ash site exhibited a sharp increase to 400 mT (0.0063 mA/M), then continued to increase in saturation to 2250 mT (0.00672 mA/M) (Fig. 15).

4.3.2 LOWRIE METHOD / TRIAXIAL DECAY

Triaxial decay curves are labeled with soft (120 mT), medium (500 mT), and hard (2500 mT) coercivity components, and are used to identify magnetic mineral unblocking (T_{ub}) temperatures within magnetic grains in samples. All triaxial decay curves are presented in standard & logarithmic formats to aid in interpretation.

Lost Cabin Wash samples LCW0-4 (Fig. 16), LCW10-1 (Fig. 17), and LCW15-1 (Fig. 18) show similar characteristics between all three components. All three samples exhibit a sharp decrease in remanence to 400°C (Figs. 16, 17, and 18). On samples LCW0-1 and LCW15-1, there is a small inflection at ~350°C (Figs. 16 and 18) in which the medium component rises in remanence, then continues to track with the soft component down to 400°C. All three samples then exhibit a continued remanence loss in the soft and medium components to 600°C. The hard component exhibits a similar decrease in remanence to 650°C.

Bouse Marl sample LCW Marl2-1B exhibited a sharp decrease in remanence in all three (soft, medium, and hard) components to 300°C (Fig. 19). The soft component then decreased to 375°C before coercivity flatlined. The medium component revealed a slow and steady decrease in remanence to 500°C, while the hard component continued to display unblocking to 600°C.

High Wall Wash ash sample HWW8-1 exhibits a sharp drop in the soft and medium components from 200-300°C (Fig. 20). The soft component then begins to increase in intensity to 550°C, before becoming indistinguishable from the medium component to 600°C. The hard

component appears to become the dominate magnetic component above 300°C, and unblocks by 550°C before exhibiting a sharp decrease to 700°C.

Wolverine Creek Ash site sample WC4-3 displayed an unblocking in all three components at 475°C (Fig. 21). The soft and medium components became indistinguishable past 475°C and exhibited a sharp decrease from 500-600°C. The hard component showed the same decrease from 500-600°C, then unblocks by 675°C.

4.3.3 OPTICAL MICROSCOPY AND SEM ANALYSIS

Thin section analysis from the Lost Cabin Wash section revealed a magnetic mineralogy of detrital hematite, magnetite, and titanomagnetite. Observed grains of abundant magnetite/titanomagnetite ranged from ~2-100µm (Fig. 22). SEM EDX analysis revealed that samples contained a mix of iron oxide, and titano-iron oxide grains (Fig. 23). The habits of these iron oxides suggest magnetite and titanomagnetite. Many grains contain exsolved titanomagnetite partitioned between ilmenite and magnetite (Fig. 24). In addition to magnetic grains, the samples contain angular grains of quartz, feldspar, biotite, muscovite, zircon, apatite, and volcanic rock fragments suspended in a clay matrix.

Thin section analysis from the Lost Cabin Wash Bouse Marl samples revealed a magnetic mineralogy of authigenic magnetite and hematite. Optical microscopy indicates abundant hematite coating pore spaces. Additionally, black dendritic manganese oxides are present, confirmed by EDX analysis (Fig. 25). Few primary detrital magnetite/titanomagnetite grains occur within marl samples. The abundance of authigenic minerals suggests that magnetism within Bouse Marl samples is held within a CRM. Most iron oxide is concentrated within micro pore spaces (Fig. 26), clustered within spheres of ~1µm framboids, likely altered from authigenic

pyrite (Fig. 27). The Bouse Marl is composed of 95% calcite grains, with 5% of the sample containing detrital sub-rounded quartz, feldspar, biotite, and zircon.

Grain analysis from the High Wall Wash samples reveal a bulk magnetic mineralogy of detrital titanomagnetite and pyrrhotite (Fig. 28). Observed grains of titanomagnetite range from 10-60µm and contain no pure magnetite grains within the observed samples (Fig. 29). In addition to pyrrhotite, abundant barium sulfides (barite) occurs throughout the samples. The bulk mineralogy was composed of angular quartz, feldspar, apatite and zircon.

4.4 SANIDINE Ar^{40}/Ar^{39} ASH DATING

LCW-ASH2 was collected within a detrital ash bed 3 m above the base of the Lost Cabin beds (~297m above sea level) in the Lost Cabin Wash. A total of 60 sanidine grains from 2 aliquots (13 and 16) were analyzed. Figure 30 shows calculated ages and associated error bars from sanidine grains. A histogram shows that grains have ages ranging from 17-18 Ma (Fig. 30). Table 3 lists sample ages, decay factors, and relative uncertainties for LCW-ASH2.

LCW-ASH3 was collected from a cobble of detrital ash found 7.5 m above the base of the Lost Cabin beds (~303.5 m above sea level) in Lost Cabin Wash. A total of 27 sanidine grains from 1 aliquot was analyzed. Figure 31 shows calculated ages and associated error bars from sanidine grains. A histogram with shows that grains have ages ranging from 16-17 Ma (Fig. 31). Table 4 lists sample ages, decay factors, and relative uncertainties for LCW-ASH3.

RC15-LCW-111 was collected within a thin ash bed found 16.8 m above the base of the Lost Cabin beds (314.5 m above sea level) in LCW. A total of 99 sanidine grains from 2 aliquots (9 and 10) were analyzed. Figure 32 shows calculated ages and associated error bars from sanidine grains. A histogram shows that grains have ages ranging from 14-18 Ma (Fig. 32).

There were several young grains within this population, with the youngest yielding an age of 5.489 Ma ± 0.788 Ma. Table 5 lists sample ages, decay factors, and relative uncertainties.

5 INTERPRETATIONS

5.1 STRATIGRAPHY

The axial-valley Lost Cabin beds are an informally named stratigraphic section of flat-lying successions of litharentite, quartzarenite, siltstone, and mudstone packages, punctuated by late Miocene ash beds. The Lost Cabin Wash section contains repeating units of fine-grained laterally extensive mudstone and siltstone, separated by erosive fluvially cross-bedded litharenite, with elevations from 296 to 324 m above sea level. This relationship suggests that the closed axial valley between the Newberry and Black Mountains underwent repeated climatically driven events in which sedimentation in the valley alternated between fluvial and lacustrine. Fossil biota are sparse, but abundant vertical burrows occurred throughout fine-grained facies within the lower 15 m of section. Mudstone in the lower section locally exhibits mudcracks and minor carbonate nodules, consistent with times of arid climate exposure. Carbonate nodule frequency increased with maximum arid climate facies indicators observed within the top 10 m of section. Wet climate indicators of laterally extensive muds, worm burrow trace fossils, and fluvially incised beds generally decrease in intensity within the first 20 m of measure section, before giving way to arid climate indicators of abundant carbonate nodules, hematite leaching, mudcracks, and paleosols. The upper section includes a 10 cm carbonate soil layer that is laterally continuous on both sides of the wash system. Sedimentary structures within the upper section are filled with gradational planar bedded silts and litharenites. The sedimentary structures and relationships documented within Lost Cabin Wash indicate climatically driven sedimentation within the axial valley of the Newberry & Black Mountains throughout the late Miocene to early

Pliocene. For full unabridged stratigraphic column of Lost Cabin beds from Lost Cabin Wash, refer to Appendix.

5.2 MAGNETIC MINERALOGY

Magnetic mineralogy was interpreted from a combination of data from demagnetization trends, Lowrie (1990) triaxial decay patterns, IRM acquisition curves, petrographic microscopy, and SEM analysis of prepared thin section and detrital sediment samples.

Magnetite is interpreted as being present in most samples of this study and is an important remanence carrier of the detrital remanent magnetization (DRM). Magnetite has a Curie temperature of 580°C, and a maximum coercivity of 0.3 to 0.5 T (Dunlop & Özdemir, 1997). Evidence for magnetite can be observed in the IRM plots of Lost Cabin Wash samples (Fig. 12), Bouse Marl2-1B (Fig. 13), and Wolverine Creek Ash WC4-3 (Fig. 15), where samples have a rapid increase in saturation curves with an inflection point around 300 to 500 mT. In the Lowrie triaxial decay plots of Lost Cabin Wash samples (Figs. 16-18), Bouse Marl2-1B (Fig. 19), and Wolverine Creek WC4-3 (Fig. 21) the soft (125 mT) and medium (500 mT) components stop decaying past 580°C, the Curie temperature of magnetite. A wide range of pure magnetite grain sizes were observed during SEM analysis ~2-50μm (Fig. 22), interpreted as a combination of single domain (SD) and multi-domain (MD) magnetite grains. Select samples that were exposed to low temperature demagnetization (LTD) showed a large decrease in the NRM, interpreted to reflect large populations of MD magnetite grains relative to other samples. In addition to pure magnetite grains, some magnetic grains exhibited exsolved textures between ilmenite and magnetite (Fig. 24). This texture reflects oxidation wherein growth of ilmenite lamellae on two or more sets of spinel planes subdivide the crystals into sheet or rod-like subgrains of magnetite

(Strangeway et al., 1968). If the magnetite subgrains are small enough (<1 μm), they will interact as SD particles with high coercivity (Dunlop & Özdemir, 1997).

Hematite is interpreted to be present in many samples. Hematite displays high magnetic coercivity >10 T (Özdemir & Dunlop, 2014), and a Néel temperature of 675°C (O'Reilly, 1984). Evidence for hematite appears in the IRM plots of Marl 2-1B (Fig. 13), HWW8-1 (Fig. 14), and WC4-3 (Fig. 15), where samples show signs of saturation at higher field strengths >500 mT. With Lowrie triaxial plots, the hard (2500 mT) component records the presence of hematite in all samples. Thermal demagnetization shows the hard component continuing to demagnetize past 580°C, which points to a high temperature, high unblocking magnetic mineral interpreted as hematite (Figs. 16-21).

Titanomagnetite is a common magnetic mineral produced from volcanic rocks and is interpreted as being present in all samples found within the CV. Titanomagnetite has a low magnetic coercivity at ~8 mT and can be identified by its Curie temperature of 150°C (Dunlop & Özdemir, 1997). Evidence for titanomagnetite can be observed in the Lowrie triaxial plots where the soft (125 mT) and medium (500 mT) components display rapid demagnetization trends from 100 to 200°C (Figs. 16-18). Titanomagnetite is common in thin sections and detrital samples (Figs. 23,28, and 29). The Curie temperature of titanomagnetite can reach 200-400°C owing to oxidation or maghemitization of primary grains. The thermal signature of an oxidized titanomagnetite is a 'hump' near 400°C in a Lowrie plot, which appears when titanomaghemite inverts to a multiphase mixture of ilmenite and strongly magnetic magnetite (Dunlop & Özdemir, 1997). Examples of this 'hump' appear in triaxial plot data in Figs. 19 and 21.

Pyrrhotite is interpreted to be present only in the HWW8-1 sample. Pyrrhotite commonly displays low coercivities ~200 mT (Hernandez, et al., 2007), and exhibits a Curie temperature

from 270 - 325°C dependent on magnetic structure (Dekkers at al., 1989). Evidence for pyrrhotite appears in IRM acquisition curves in which the sample rapidly reaches saturation at 200 mT (Fig. 14). Lowrie triaxial decay curves exhibit a rapid demagnetization from 200-300°C, then a small increase of the soft component to 550°C. During thermal demagnetization, pyrrhotite transforms irreversibly to magnetite (Bina & Daly, 1994). At higher temperatures (>580°C), the pyrrhotite transforms to hematite, either directly or by oxidation of the newly created magnetite (Dekkers, 1990). Additionally, abundant iron and barium sulfides occur in HWW sediments (Fig. 28). The presence of pyrrhotite and barite in only the High Wall Wash samples suggests that the volcanic ash was deposited from a secondary, distally sourced eruption with a sulfur-rich geochemistry; or that the pyrrhotite was sourced from a localized detrital input from the Black Mountains to the east.

5.3 MAGNETIC REMANENCE

Ancient sedimentary rocks commonly record a low-temperature, low-coercivity viscous remanent magnetization (VRM) of the Modern magnetic field (Dunlop & Özdemir, 1997). To ensure the removal of the Modern VRM, stable low temperature components were picked from a total of 77 samples (Table 1). The mean declination/inclination values from the VRM is D=13.5° I=59.5° (Fig. 8b), while Modern values are D=11.25° I=60.68°. Because of the 1-2° similarity between measured values and Modern, the VRM represents a viscous overprint of the modern magnetic field. The low unblocking temperatures (100-200°C) and multidomain nature of titanomagnetite makes it a common VRM carrier in sedimentary rocks (Dunlop & Özdemir, 1997).

The ChRM within the Lost Cabin Wash section is interpreted as a detrital remanent magnetization (DRM) from primary magnetite, titanomagnetite, titanomaghemite, and detrital

hematite. These primary grains would have been sourced from the Black and Newberry Mountains, and deposited within the distal fine-grained axial valley. The ChRM was resolved using both alternating field (AF) and thermal demagnetization (Table 2). The consistent inclination shallowing yielded from reverse-polarity samples supports that the interpreted ChRM is a primary DRM. Sites that that exhibited high unblocking temperatures (>580°C) held the same direction as those with lower unblocking temperatures. These higher-temperature components are interpreted as being a primary magnetization from detrital hematite grains which were readily observed in thin section.

The ChRM within the Wolverine Creek Ash site is attributed to a DRM in primary magnetite and detrital hematite. The Wolverine Creek ash was sourced from the Snake River Plane-Yellowstone Hotspot, indicating a distally sourced magnetic mineralogy. The ChRM was resolved using both alternating field (AF) and thermal demagnetization (Table 2). These results point to a stable magnetite component which unblocked at 580°C. The strong magnetic component observed in the Lowrie triaxial data (Fig. 21) is attributed to hematite. Most samples exhibited demagnetization behavior >580°C with the same ChRM observed in lower temperature and AF decay, indicating both magnetite and detrital hematite as remanence carriers.

Bouse Marl samples have magnetic components held in hematite and secondary magnetite after pyrite. AF and thermal demagnetization indicate that Bouse Marl samples within the CV are poor carriers of stable magnetizations. This is indicated by the lack of stable magnetic components and magnetizations that were an order-of-magnitude weaker than Lost Cabin Wash samples. Optical and reflected light microscopy shows that samples are predominantly composed of a carbonate siltstone with sparse opaque minerals. Samples exhibit minor hematite reddening and secondary magnetite after pyrite framboids within pore networks (Fig. 26). Because a ChRM

could not be isolated due to the lack of stable magnetic directions in the weak samples, all Bouse Marl samples were excluded from sample site statistics.

The ChRMs within the High Wall Wash Ash site is unique in that DRMs are held in a wide range of magnetic mineralogies; including titanomagnetite, magnetite, hematite and pyrrhotite. Although tephrochronology hasn't identified a source for the High Wall Wash ash, the abundance of iron and barium sulfides in SEM analysis points to an allochthonous source mineralogy within ash sediments. The rapid remanence loss at 100°C is attributed to a low coercivity titanomagnetite component (Fig. 20). This is followed by another drop from 200-300°C interpreted to represent the Curie temperature of the pyrrhotite component. Past 300°C the hard component (hematite) is the primary remanence carrier. The HWW site exhibits anomalous behavior in which AF and thermal demagnetization results differed in results/magnetic polarity (Table 2). This discrepancy is interpreted to reflect AF demagnetization being more effective than thermal demagnetization at resolving the ChRM in the low-coercivity titanomagnetite and pyrrhotite. Large steps were performed during thermal demagnetization to prevent samples from disaggregating, which led to a quick destruction of the primary magnetization by 300°C, leaving hematite as the only magnetic remanence carrier. The HWW site has a well-developed paleosol with hematite reddened samples, of which some samples contained components >580°C. The hematite component is interpreted as being a secondary ChRM acquired during prolonged sediment exposure as indicated by the paleosol. Most HWW samples also exhibited ambiguous components past 500°C. This is interpreted as being a result of pyrrhotite converting to magnetite. If the field in the furnace is not perfectly zeroed, the resulting thermochemical remanent magnetization (TCRM) can obscure the NRM of the primary magnetite over its main unblocking range (Dunlop & Özdemir, 1997).

5.4 ASH DATING

Ash sample LCW-ASH2 was collected near the base of the Lost Cabin beds in the Lost Cabin Wash with the hopes of providing a lower age bracket for magnetostratigraphy. The bulk distribution of sanidine grains 55/60 have ages ranging from 16 to 18 Ma (Fig. 30). The ash sample was collected within a fluvially cross-bedded section and was laterally traceable for at least 7.75 m along the exposed wall. Due to the limited lateral continuity and high energy sedimentary structures such as large-scale crossbeds bounding the ash, this sample location likely represents a reworking of older detrital sanidine grains from proximal early-mid Miocene volcanism within the CV.

Ash sample LCW-ASH3 was also collected near the base of the Lost Cabin beds in the Lost Cabin Wash from a 130mm diameter detrital ash cobble with the intention of providing a maximum depositional age of the Lost Cabin beds. The bulk distribution of sanidine grains 18/27 have ages centered on ~16 Ma (Fig. 31). This sample, like LCW ASH2, was collected from a section of strata that contains high-energy sedimentary structures with large ash and scoria clasts. This sample likely represents an older detrital ash cobble from early-middle Miocene volcanism, that was carried downstream from the Black Mountains to the east.

Ash sample RC15-LCW-111 was collected ~15 m from the base of the Lost Cabin beds in Lost Cabin Wash by Ryan Crow of the USGS. The ash sample was identified and collected from a ~1-2 cm laterally continuous bedded deposit on the south wall. The bulk distribution of sanidine grains 71/99 have ages ranging from ~14 to 18 Ma (Fig. 32). The RC15-LCW-111 site yielded one young sanidine grain of 5.489 Ma ± 0.788 Ma, which signifies a younger early Miocene ashfall event. The larger older grain distribution likely represents detrital sanidine contamination/reworking from early-mid Miocene volcanism within the CV.

The results from the three ash samples analyzed via sanidine $^{40}Ar/^{39}Ar$ age dating all point to a distribution of ages from 14 to 18 Ma, with the largest number of grains centered ~16 Ma. Previous $^{40}Ar/^{39}Ar$ dating of the High Wall Wash ash site yielded similar early to middle Miocene results, in addition to the 18 young grains that have a weighted mean age of 5.35 ± 0.7 Ma (Fig. 33). These results point to the majority of larger sanidine grains that were picked from the samples being detrital in origin, eroded from older proximal volcanic ash deposits within the CV. These results agree with the work of Faulds et al. (1995), which used $^{40}Ar/^{39}Ar$ to date tilted volcanic sediments within the CV to bracket maximum localized extension and volcanism between 16.2 and 11 Ma. Sanidine grains around 18 Ma are likely to be related to the 18.5 Ma Peach Springs Tuff that blanketed the Colorado River corridor (Glazner et al., 1986; Nielson et al., 1990). Tephrochronology has indicated that the 5.59 ± 0.05 Ma Wolverine Creek ash in the CV originated from the Snake River plain/Yellowstone track in Wyoming (House et al., 2008), and the 4.83 Ma Lawlor Tuff in Blythe basin to the south originated from the northern San Francisco Bay Area (Sarna-Wojcicki et al., 2011). These results indicate that most late Miocene ash deposits within the lower Colorado River corridor originate from large-scale, distal ashfall events. The farther these distal ash deposits had to travel, the higher likelihood that larger sanidine grains would have fallen out of the column leaving mostly smaller (~1-2μm) grains that would be under the resolution of traditional light microscopy used for sanidine grain removal. This could explain the low number of young grains found in the High Wall Wash (18 grains) and RC15-LCW-111 (1 grain) sample from this study.

5.5 MAGNETOSTRATIGRAPHY

A total of 99 samples from 23 sites (Table 2) were used to determine polarity within the Lost Cabin Wash section. Sample sites LCW0 to LCW20 record a consistent southern

hemisphere reverse component and sample sites LCW21 to LCW30 record a consistent northern hemisphere normal component (Fig. 34). Sites LCW20 to LCW21 were sampled with Pomeroy drill at the decimeter scale to more precisely locate the stratigraphic level of the paleomagnetic reversal, which lies between sites LCW-T6 and LCW-T8 (Table 2) at an elevation of 320.9 m above sea level (Fig. 34). Ash sample RC15-LCW-111 with a single young sanidine grain dated at 5.489 Ma ± 0.788 Ma was found below the reversal site at an elevation of 314 m above sea level (Fig. 35).

A total of 23 samples from 7 sites (Table 2) were used to determine polarity from the Wolverine Creek Ash site and to validate polarity with tephrochronology data which points to an age of 5.59 ± 0.05 Ma (Fig. 36). The ChRM resolved from AF and thermal demagnetization shows a consistent southern hemisphere reverse polarity throughout the sample sites. The reverse polarity further validates the 5.59 Ma age found via tephrochronology and provides a C3r subchron lower age constraint of Lost Cabin beds within CV.

A total of 39 samples from 11 sample sites (Table 2) were used to determine polarity from the High Wall Wash ash site and to cross validate polarity with tephrochronology data which points to an age of 5.35 ± 0.07 Ma (Fig. 37). Sample sites HWW1 to HWW 4 contain abundant 1-3 cm volcanic clasts and were removed from site statistics on account of samples being too coarse. AF demagnetization data were used to determine polarity, which is interpreted to contain southern hemisphere reverse components from HWW5 to HWW8, and northern hemisphere normal components for samples HWW9 to HWW12. The reversal is located at an elevation of 322 m above sea level directly above the previously dated reworked ash. Due to the location of the reversal above the ash, and the total elevation 322 m above sea level, the reversal found in High Wall Wash is interpreted to be the same reverse-normal transition as that recorded in Lost

Cabin Wash at 320.9 m above sea level. Based on three dated ash beds and a single reversal recorded in two wash systems, I infer that this geomagnetic reversal records the (5.235 Ma) transition from the C3r subchron to C3n.4n (THVERA) subchron of the Gilbert Chron using the GPTS c-sequence marine magnetic anomaly distances and ages model of Ogg (2012) (Fig. 34)(Table 2).

Samples were collected from 3 sites at the Golden Section sample locality to better understand the polarity of this critical pre-Bouse integration site. The Golden Section is unique as being the only site in CV where the Bouse Marl is observed directly on Lost Cabin beds. This location contains the lowest recorded Bouse Marl deposit within the CV and one of the highest elevations of the fine-grained facies deposits of the Lost Cabin beds within the study area (Fig. 38). The Lost Cabin beds at the Golden Section do not resemble any of the lithological characteristics of the arid to coarse upper facies that have been mapped and described in both Lost Cabin Wash and High Wall Wash. The Golden Section features wavy bedded, fine-grained sands with localized layers of green muds interbedded within upper Lost Cabin beds. Two samples from site GS3 and three samples from GS4 show that the sediments contain a reverse polarity (Table 2). The site is ~32 m above the reversal site in High Wall and Lost Cabin wash. Because of the lithological/facies difference, elevation discrepancy between reverse polarity sites, and age of Bouse Marl deposits downstream at Buzzards Peak (4.83 Ma), I infer that this section represents subchron C3n.3r of the Gilbert chron (Ogg, 2012). This suggests that the Colorado River waters reached the upper corridor in Cottonwood Valley between 4.799 and 4.997 Ma. In addition to the Golden Section, a site within the Lost Cabin Wash contains an unconformable fluvial deposit that truncates normal-polarity beds on the north wall (Fig. 39). The base of the fluvial cut contains a detrital cobble of Bouse Marl, indicating that this site

records a post-lacustrine erosional event during the draining of paleo-Lake Mohave. Four samples from one site have been tested which yielded a reverse polarity. This is distinct from the surrounding normal polarity Lost Cabin beds and indicates these sediments record a later geologic event.

Stratigraphic correlation of all sample sites within the CV have been plotted on Figure (40). All elevation data were measured via high precision GPS and are presented in m above sea level. All three ash beds are labeled with a dashed line and displayed with age and elevation data. Polarity reversals are indicated by magnetic polarity bars in which black equals normal polarity and white equals reverse polarity. All polarity results are tied to the Geomagnetic Polarity Timescale (GPTS) with subchron/chron data provided from Ogg (2012). The reversal sites from Lost Cabin Wash and High Wall Wash are within 1 m of elevation of one another, which is expected on a laterally migrating alluvial fan. Due to similar elevations and a dated 5.35 ± 0.07 Ma ash bed, I infer that these two reversal sites represent the same Cr3 to Thvera subchron transition. According to Fauld at al. (2001), Cottonwood Valley has been relatively tectonically dormant since 12 Ma; modern elevations might closely reflect elevations during deposition. Utilizing elevation data from the dated Wolverine Creek 5.59 ± 0.05 Ma ash and the new ash site RC15-LCW-111 with an age of 5.489 Ma ± 0.788 Ma, an average sedimentation was calculated to be 0.0276 cm/yr. Furthermore, elevation data between the RC15-LCW-111 site and the Cr3 to Thvera transition site yields an average sedimentation rate of 0.0025 cm/yr. The decrease in average sedimentation rates agrees with observed facies trends in which Lost Cabin sediments record a transition from fluvial (high sediment influx) to arid (low sediment influx) facies from bottom to top (Fig. 34).

6 CONCLUSIONS

Magnetostratigraphic relationships discovered within Cottonwood Valley suggest that Lost Cabin bed sediments accumulated during the late Miocene to early Pliocene. A total of three ash beds were used in this study to provide absolute dates to correlate magnetic polarity to the geomagnetic polarity timescale (GPTS). All three ash dates (5.59, 5.49, and 5.35 Ma) occur within reverse-polarity sediments, interpreted as belonging to the C3r subchron of the Gilbert chron. Two sites within CV recorded a reverse to normal magnetic reversal. This magnetic reversal is interpreted as recording the C3r to C3n.4n (Thvera) subchron transition which has an age of 5.235 Ma. Both reversal sites are within 1 m difference in elevation with one site occurring directly above an ash bed dated via $^{40}Ar/^{39}Ar$ at 5.35 ± 0.07 Ma. The work of this study provides critical upstream constraints on integration of the early Colorado River system. Stratigraphic, paleomagnetic, and $^{40}Ar/^{39}Ar$ data suggest that Colorado River sediments did not fill the northernmost Cottonwood Valley until after 5.235 Ma.

I propose that future geochronological studies within Cottonwood Valley focus on conducting a more robust sampling of pre- and post-Bouse sample site localities identified by this study. These include the Golden Section site, Bouse incision site, and the abundant syn-Bouse sediments within proximal wash systems. Lithologic relationships and reverse polarity samples at the Golden Section and Bouse incision sites suggests a post 5.235 Ma event in which Colorado River waters filled and receded from Cottonwood Valley. Based on 4.83 ± 0.011 Ma Lawlor Tuff found in Bouse Marl sediments to the south, this reverse polarity in pre- and syn-Bouse aged beds likely point to the C3n.4n magnetic subchron which spanned from 4.799 to 4.997 Ma. However, additional paleomagnetic sampling should be completed to test this hypothesis.

REFERENCES

Anderson, R. E., Longwell, C. R., Armstrong, R. L., & Marvin, R. F. (1972). Significance of K-Ar Ages of Tertiary Rocks from the Lake Mead Region, Nevada-Arizona. *Geological Society of America Bulletin, 83*(2), 273-288.

Bina, M., & Daly, L. (1994). Mineralogical change and self-reversed magnetizations in pyrrhotite resulting from partial oxidation; geophysical implications. *Physics of the Earth and Planetary Interiors, 85*(1-2), 83-99.

Cande, S. C., & Kent, D. V. (1995). Revised calibration of the geomagnetic polarity timescale for the Late Cretaceous and Cenozoic. *Journal of Geophysical Research: Solid Earth,100*(B4), 6093-6095.

Crow, Ryan (2018). Personal Correspondence.

Dekkers, M. J., Mattéi, J., Fillion, G., & Rochette, P. (1989). Grain-size dependence of the magnetic behavior of pyrrhotite during its low-temperature transition at 34 K. *Geophysical Research Letters, 16*(8), 855-858.

Dekkers, M. J. (1990). Magnetic monitoring of pyrrhotite alteration during thermal demagnetization. *Geophysical Research Letters, 17*(6), 779-782.

Dorsey, R. J., Housen, B. A., Janecke, S. U., Fanning, C. M., & Spears, A. L. (2011). Stratigraphic record of basin development within the San Andreas fault system: Late Cenozoic Fish Creek-Vallecito basin, southern California. *Geological Society of America Bulletin, 123*(5-6), 771-793.

Dunlop, D. J., & Argyle, K. S. (1991). Separating multidomain and single-domain-like remanences in pseudo-single-domain magnetites (215–540 nm) by low-temperature demagnetization. *Journal of Geophysical Research, 96(B2)*, 2007.

Dunlop, D. J., & Özdemir, O. (2013). *Rock magnetism fundamentals and frontiers*. Cambridge: Cambridge Univ. Press.

Faulds, J.E., & Bell, J.W., (1999). Geologic map of the Nelson SW Quadrangle, Clark County, Nevada: *Nevada Bureau of Mines and Geology Open-File Report 99-15*, scale 1:24,000.

Faulds, J.E., Feuerbach, D.L., Miller, C.F., & Smith, E.I., (2001). Cenozoic evolution of the Northern Colorado River Extensional Corridor, southern Nevada and northwestern Arizona: *American Association of Petroleum Geologists Publication, 78*, 239-271.

Faulds, J. E., Feuerbach, D. L., Reagan, M. K., Metcalf, R. V., Gans, P., & Walker, J. D. (1995). The Mount Perkins block, northwestern Arizona: An exposed cross section of an evolving, preextensional to synextensional magmatic system. *Journal of Geophysical Research: Solid Earth, 100(B8)*, 15249-15266.

Faulds, J. E., Schreiber, B. C., Langenheim, V. E., Hinz, N. H., & Shaw, T. H. (2016). Paleogeographic Implications of Late Miocene Lacustrine And Nonmarine Evaporite Deposits In The Lake Mead Region: Immediate Precursors To The Colorado River. *Geosphere, 12(3),* 721-767.

Faulds, J.E., Smith, E.I., and Gans, P., (1999). Spatial and temporal patterns of magmatism and extension in the northern Colorado River extensional corridor, Nevada and Arizona: A preliminary report: *Nevada Petroleum Society Guidebook,* 171-183.

Fisher, R. (1953). Dispersion on a Sphere. *Proceedings of the Royal Society A: Mathematical, Physical and Engineering Sciences, 217(1130),* 295-305.

Glazner, A., Miller, D., Nielson, J., & Howard, K. (1986). Correlation of the Peach Springs Tuff, a large-volume Miocene ignimbrite sheet in California and Arizona. *Geology, 14,* 840-843.

Harvey, J. C. (2014). Zircon age and oxygen isotopic correlations between Bouse Formation tephra and the Lawlor Tuff. *Geosphere, 10*(2), 221-232.

House, P.K., Crow, R.S., Pearthree, P.A., Brock-Hon, A.L., Schwing, J.E., Thacker, J., Gootee, B., Felger, T.J., (2018). *Surficial Geologic Map of the Spirit Mountain SE 7.5' Quadrangle and Surrounding Areas, Arizona and Nevada* (Unpublished).

House, P.K., Pearthree, P.A., and Perkins, M.E., (2008). Stratigraphic evidence for the role of lake spillover in the inception of the lower Colorado River in southern Nevada and western Arizona, in Reheis, M.C, Hershler, R., and Miller, D.M. (eds.), Late Cenozoic Drainage History of the Southwestern Great Basin and Lower Colorado River Region: Geologic and Biotic Perspectives: *Geological Society of America Special Paper 439,* 335–353.

King, R. F. (1955). The Remanent Magnetism of Artificially Deposited Sediments. *Geophysical Journal International, 7,* 115-134.

Kirschvink, J. L. (1980). The least-squares line and plane and the analysis of palaeomagnetic data. *Geophysical Journal of the Royal Astronomical Society, 62,* 699-718.

Koymans, M. R., Langereis, C. G., Pastor-Galán, D., & Hinsbergen, D. J. (2016). Paleomagnetism.org: An online multi-platform open source environment for paleomagnetic data analysis. *Computers & Geosciences, 93,* 127-137.

Lowrie, W. (1990). Identification of ferromagnetic minerals in a rock by coercivity and unblocking temperature properties. *Geophysical Research Letters, 17*(2), 159-162.

McDougall, K., (2008). Stratigraphic evidence for the role of lake spillover in the inception of the lower Colorado River in southern Nevada and western Arizona, in Reheis, M.C, Hershler, R., and Miller, D.M. (eds.), Late Cenozoic Drainage History of the Southwestern Great Basin and Lower Colorado River Region: Geologic and Biotic Perspectives: *Geological Society of America Special Paper 439,* 355–373.

Mcdougall, K., & Martínez, A. Y. (2014). Evidence for a marine incursion along the lower Colorado River corridor. *Geosphere, 10(5),* 842-869.

Mcfadden, P. L., & Mcelhinny, M. W. (1990). Classification of the reversal test in palaeomagnetism. *Geophysical Journal International, 103*(3), 725-729.

Metzger, D.G., (1968). The Bouse Formation (Pliocene) of the Parker-Blythe-Cibola area, Arizona and California: *U.S. Geological Survey Professional Paper 600-D,* D126-D136.

Miranda-Martínez, A. Y., Carreño, A. L., & Mcdougall, K. (2017). The Neogene genus Streptochilus (Brönnimann and Resig, 1971) from the Gulf of California. *Marine Micropaleontology, 132,* 35-52.

Morikawa, S.A., (1994). *The Geology of the Tuff of Bridge Spring, southern Nevada and northwestern Arizona* (M.S.thesis University of Nevada, Las Vegas).

Nielson, J. E., Lux, D. R., Dalrymple, G. B., & Glazner, A. F. (1990). Age of the Peach Springs Tuff, southeastern California and western Arizona. *Journal of Geophysical Research, 95*(B1), 571.

Ogg, J.G., (2012). Geomagnetic Polarity Time Scale. In: Gradstein, F.M., Ogg, J.G., Schmitz, M., Ogg, G. (Eds.), *The Geologic Time Scale 2012. Elsevier, Amsterdam,* 85-114.

Opdyke, N., Lindsay, E., Johnson, N., & Downs, T. (1977). The Paleomagnetism and Magnetic Polarity Stratigraphy of the Mammal-Bearing Section of Anza Borrego State Park, California. *Quaternary Research, 7(03),* 316-329.

OReilly, W. (1984). *Rock and mineral magnetism*. Glasgow: Blackie.

Özdemir, Ö, & Dunlop, D. J. (2014). Hysteresis and coercivity of hematite. *Journal of Geophysical Research: Solid Earth, 119(4),* 2582-2594.

Pearthree, P. A., & House, P. K. (2014). Paleogeomorphology and evolution of the early Colorado River inferred from relationships in Mohave and Cottonwood valleys, Arizona, California, and Nevada. *Geosphere, 10(6),* 1139-1160.

Reheis, M., Hershler, R., & Miller, D. (2008). Late Cenozoic Drainage History of the Southwestern Great Basin and Lower Colorado River Region: Geologic and Biotic Perspectives. *Geological Society of America Special Paper 439*.

Sarna-Wojcicki, A. M., Deino, A. L., Fleck, R. J., Mclaughlin, R. J., Wagner, D., Wan, E., . . . Perkins, M. (2011). Age, composition, and areal distribution of the Pliocene Lawlor Tuff, and three younger Pliocene tuffs, California and Nevada. *Geosphere, 7(3),* 599-628.

Simpson, C., Schweitzer, J., & Howard, K. A. (1991). A reinterpretation of the timing, position, and significance of part of the Sacramento Mountains detachment fault, southeastern California. *Geological Society of America Bulletin, 103(6),* 751-761.

Spencer, J. E., & Patchett, P. J. (1997). Sr isotope evidence for a lacustrine origin for the upper Miocene to Pliocene Bouse Formation, lower Colorado River trough, and implications for timing of Colorado Plateau uplift. *Geological Society of America Bulletin, 109(6)*, 767-778.

Spencer, J. E., Patchett, P. J., Pearthree, P. A., House, P. K., Sarna-Wojcicki, A. M., Wan, E., . . . Faulds, J. E. (2013). Review and analysis of the age and origin of the Pliocene Bouse Formation, lower Colorado River Valley, southwestern USA. *Geosphere, 9(3)*, 444-459.

Spencer, J.E., Peters, L., McIntosh, W.C., and Patchett, P.J., (2001). 40Ar/39Ar geochronology of the Hualapai Limestone and Bouse Formation and implications for the age of the lower Colorado River, in Young, R.A., and Spamer, E.E., eds., The Colorado River: Origin and evolution: *Grand Canyon Association Monograph 12*, 89–91

Steiger, R., & Jäger, E. (1977). Subcommission on geochronology: Convention on the use of decay constants in geo- and cosmochronology. *Earth and Planetary Science Letters, 36(3)*, 359-362.

Strangway, D. W., Larson, E. E., & Goldstein, M. (1968). A possible cause of high magnetic stability in volcanic rocks. *Journal of Geophysical Research, 73(12)*, 3787-3795.

Tauxe, L., Kodama, K. P., & Kent, D. V. (2008). Testing corrections for paleomagnetic inclination error in sedimentary rocks: A comparative approach. *Physics of the Earth and Planetary Interiors, 169(1-4)*, 152-165.

Tauxe, L., & Kent, D. V. (2013). A Simplified Statistical Model for the Geomagnetic Field and the Detection of Shallow Bias in Paleomagnetic Inclinations: Was the Ancient Magnetic Field Dipolar? *Timescales Of The Paleomagnetic Field Geophysical Monograph Series*, 101-115.

Zijderveld, J.D.A., (1967). A. c. demagnetization of rocks: analysis of results. In Collinson, D.E. et al., eds., *Methods in Paleomagnetism. New York, Elsevier Science*, 254-286.

TABLES

TABLE 1: SITE MEAN DIRECTIONS – VRMs

SAMPLE	DECLINATION	INCLINATION
BC6-1	23.41023	54.8074
BC6-3	42.89904	58.1288
BC6-4	42.29037	48.5921
HWW 11-1	20.03098	66.35596
HWW 11-2	8.278374	52.53655
HWW 6-7	24.17158	58.2575
HWW 6-7	24.17158	58.2575
HWW 9-6	345.0086	67.05962
LCW0-1	11.82833	57.4917
LCW0-2	7.265929	68.0302
LCW0-4	45.15214	40.13351
LCW10-1	285.3408	61.05331
LCW10-2	330.1109	33.11557
LCW10-3	327.2247	54.71931
LCW11-1	23.32776	42.29621
LCW11-3	3.136519	23.50017
LCW11-5	344.922	53.17968
LCW1-2	27.22561	59.66566
LCW12-1	290.1437	47.41276
LCW12-2	318.369	65.29958
LCW12-3	22.52973	59.52662
LCW14-3A	51.49178	8.276678
LCW15-1	8.260507	67.66151
LCW15-2A	335.9376	53.62857
LCW15-2B	357.4234	38.75023
LCW15-3	347.9454	70.53462
LCW1-6	36.28444	61.34474
LCW16-1	345.2209	37.20734

LCW16-3	334.6564	45.3068
LCW19-1	43.84077	36.39039
LCW20-1	13.89549	55.97651
LCW20-2	35.29304	67.39265
LCW21-1	347.6512	48.8506
LCW21-3	346.2826	43.55164
LCW2-1B	7.058246	68.8487
LCW22-3	57.72114	55.43755
LCW22-4	56.53775	55.70164
LCW23-1	348.6685	56.90321
LCW23-2	307.7321	57.62334
LCW23-3	19.65498	53.91073
LCW2-4	11.86881	52.83725
LCW24-1A	13.5296	59.36363
LCW24-2	358.1459	50.93789
LCW25-1	42.17518	62.36002
LCW25-2C	69.25724	48.59304
LCW25-3	17.48074	62.51132
LCW25-3	11.86679	40.60689
LCW25-3	17.48074	62.51132
LCW25-3	11.86679	40.60689
LCW28-1	34.91097	48.11296
LCW28-2	27.3302	45.44132
LCW28-3	358.5984	42.54787
LCW3-1	322.1911	36.30918
LCW4-2A	11.12484	60.72558
LCW4-3A	45.38383	69.48673
LCW5-1	33.51134	61.2511
LCW5-2A	4.632745	46.30175
LCW5-4	345.0854	59.85726
LCW5-5	11.43692	45.09821

LCW8-1	23.05015	75.08961
LCW8-2A	359.1402	62.56298
LCW9-1A	38.01448	53.77627
LCW9-1B	65.72837	69.34534
LCW9-1C	14.12879	68.4632
LCW9-2	55.13284	78.55046
LCW9-3	12.34362	88.09047
WC 1-1	38.97104	62.72161
WC 2-1	27.95944	57.62775
WC 2-2	26.35781	66.26618
WC 3-1B	59.165	54.68344
WC 3-4	334.9091	63.48861
WC 3-4	17.87224	69.07079
WC 3-4	17.87224	69.07079
WC 3-4	17.87224	69.07079
WC 4-1A	42.99626	48.95451
WC 5-3	36.88934	70.8727
WC 6-1	67.09303	51.34126

TABLE 2: SITE MEAN DIRECTIONS – ChRMs

LCW MAG STRAT										
SAMPLE NAME	DEMAG	POLARITY	DEC.	INC.	MAD	RANK	LAT	LONG	α	k
LCW 0-1	AF	R	169.1	-28.6	7.8	A	35.65662°	-114.56983°		
LCW 0-2	TH	R	169.3	-55.2	8.3	A				
LCW 0-3	TH/LTD	R	169.1	-37.9	7.4	A				
LCW 0-4	AF	R	160.5	-59.8	1.9	A				
SITE MEAN			**167.3**	**-44.4**					**15.6**	**35.59**
LCW 1-1	AF	AMBIG	109.3	26.7	5.3	D	35.65662°	-114.56983°		
LCW 1-2	TH	R	155.6	-12.4	11.7	B				
LCW 1-4	TH/LTD	R	162.7	-44.6	5.6	A				
LCW 1-5	AF	R	150.2	-18.4	4.8	B				
LCW 1-6	TH	No Pickable Components Great Circle Trend points to reversed				D				
SITE MEAN			**155.6**	**-25.1**					**27.9**	**20.58**
LCW 2-1B	AF	N	45.7	65.3	5.7	C	35.35669°	-114.56941°		
LCW 2-4A	TH	R	167.2	-10.6	11.3	B				
LCW 2-4B	TH/LTD	R	155.1	-23.3	10.3	B				
LCW 2-5A	TH	R	170.4	-27	10.6	B				
LCW 2-5B	AF	AMBIG	25.3	-9.2	5.4	C				
SITE MEAN			**146.6**	**-29.2**					**95.4**	**1.92**
LCW 3-1A	AF	R	174.7	-45.6	2.1	A	35.35669°	-114.56941°		
LCW 3-2	TH/LTD	R	196.5	-57.2	1.5	A				
LCW 3-3	TH	R	200.6	-55.4	4.4	A				
LCW 3-4	AF	R	188	-38.8	2.1	A				
SITE MEAN			**189.0**	**-49.7**					**13.0**	**51.26**
LCW 4-2A	AF	R	130.4	-36.1	5.5	A	35.35667°	-114.56927°		
LCW 4-2B	TH/LTD	R	156	-40.5	4.4	A				
LCW 4-3A	AF	R	147.9	-47.5	3.9	A				

LCW 4-3B	TH	R	148.9	-47.8	4.2	A				
SITE MEAN			**145.4**	**-43.4**					**11.4**	**65.63**
LCW 5-1	AF	R	179.5	-52.9	4.7	A	35.35688°	-114.56882°		
LCW 5-2A	TH	R	184.9	-51.9	5.6	A				
LCW 5-2B	TH/LTD	R	186.8	-56.7	4	A				
LCW 5-3	AF	R	153.2	-60.7	10.5	B				
LCW 5-4	AF	R	167.6	-48.9	3.9	A				
LCW 5-5	TH	R	168.1	-47.9	7.4	A				
SITE MEAN			**173.7**	**-53.7**					**7.2**	**86.56**
LCW 8-1	AF	R	200.4	-55.8	3.9	A	35.35744°	-114.56757°		
LCW 8-2A	TH	R	192.3	-65.9	6.2	A				
LCW 8-2B	AF	R	176.1	-65.8	3.2	A				
LCW 8-3A	TH/LTD	R	181.2	-60.3	4.6	B				
SITE MEAN			**188.3**	**-62.3**					**8.1**	**129.77**
LCW 9-1A	TH	R	220	-34.6	3.9	A	35.35749°	-114.5675°		
LCW 9-1B	TH	R	218.2	-34.3	3.8	A				
LCW 9-1C	TH	R	214.5	-34.8	4.9	A				
LCW 9-2	AF	R	209.7	-36.2	3.1	A				
LCW 9-3	AF	R	212.4	-43.5	2.4	A				
LCW 9-4	TH/LTD	R	216	-34.1	3.7	A				
SITE MEAN			**215.3**	**-36.2**					**3.9**	**303.02**
LCW 10-1	AF	R	180.2	-38.1	8.9	B	35.35748°	-114.56727°		
LCW 10-2A	TH/LTD	R	174.4	-16.7	6.6	B				
LCW 10-2B	TH	R	168	-23.5	6.8	A				
LCW 10-3	TH	R	161.8	-36.4	9.1	A				
LCW 10-4	AF	R	150	-31	2.1	A				
SITE MEAN			**166.9**	**-29.5**					**12.8**	**36.44**
LCW 11-1	TH	R	180.2	-28.5	5	A	35.35762°	-114.5668°		
LCW 11-3	AF	R	181.4	-45.2	3.4	A				

LCW 11-5	TH	R	181.5	-37	6.4	A				
SITE MEAN			**181.0**	**-36.9**					**12.8**	**93.80**
LCW 12-1	AF/LTD	R	187.5	-20.1	9	B				
LCW 12-2	AF/LTD	AMBIG	173.2	5.1	9.6	C	35.35773°	-114.56666°		
LCW 12-3	TH	R	198.6	-17	7.3	A				
SITE MEAN			**186.3**	**-10.9**					**29.0**	**19.11**
LCW 13-1A	AF/LTD	N/A				C	35.35772°	-114.5666°		
LCW 13-2	TH/LTD	R	214.6	-35.3	11.1	B				
SITE MEAN			**214.6**	**-35.3**						
LCW 14-2	AF	A/A				D	35.35766°	-114.56653°		
LCW 14-3A	AF	R	161	-18.8	9.4	B				
SITE MEAN			161.0	-18.8						
LCW 15-1	AF	R	201	-46.6	4.1	B				
LCW 15-2A	TH	R	189.8	-47.6	6.1	A				
LCW 15-2B	TH	R	196.2	-49.9	5.9	A	35.35809°	-114.56563°		
LCW 15-3	AF	R	178.6	-43.9	6.9	B				
LCW 15-7B	TH/LTD	R	197.9	-44.1	2.1	B				
SITE MEAN			**192.6**	**-46.7**					**6.3**	**146.76**
LCW 16-1	TH	R	183.4	-42.4	12.8	A				
LCW 16-2	AF	R	187.7	-35.3	9.8	B	35.35853°	-114.56455°		
LCW 16-3	TH	R	180.5	-33.5	15	B				
SITE MEAN			**182.2**	**-37.1**					**7.4**	**278.00**
LCW 19-1	AF	R	154	-26.7	9.2	B				
LCW 19-2	AF	R	205.1	-35.1	5.8	B	35.35857°	-114.56423°		
LCW 19-3	TH/LTD	R	177.6	-12.1	10.7	B				
SITE MEAN			181.9	-32.0					**35.9**	**12.83**
LCW 20-1	AF	R	158.6	-51	10	B	35.35870°	-114.56425°		
LCW 20-2	AF	R	124.1	-49.4	9.9	B				

LCW 20-3	AF	R	159.5	-59.5	11	B				
LCW 20-5A	AF/LTD	R	174	-11.3	13.3	C				
LCW 20-5B	AF	R	164.3	-53.1	6	B				
LCW 20-6A	TH/LTD	R	153.7	-21.9	8	B				
LCW 20-6C	AF/LTD	R	184.4	67.5	4.4	C				
SITE MEAN			**156.9**	**-42.3**					**19.7**	**12.47**
LCW 21-1	AF	N	27.5	54.6	2.2	A				
LCW 21-2	AF	N	9.8	17.7	10.4	C				
LCW 21-3A	TH/LTD	N	35.2	64.3	5.6	B	35.35868°	-114.56489°		
LCW 21-3B	AF/LTD	AMBIG	50.9	-15.3	2.1	B				
LCW 21-4	TH	R	131.7	-39.5	4.9	A				
SITE MEAN			**20.9**	**48.3**					**22.2**	**10.02**
LCW 22-1	TH	N	46.1	49.6	3.3	A				
LCW 22-2	AF/LTD	N	37.3	38.9	5.1	A				
LCW 22-3	TH	N	51	51.1	3.3	A	35.35950°	-114.56268°		
LCW 22-4A	AF	N	45.7	57.3	1.1	A				
LCW 22-4B	TH	N	39.7	47.3	3	A				
SITE MEAN			**43.5**	**48.9**					**7.2**	**115.13**
LCW 23-1	TH/LTD	N	8.5	27	6.5	B				
LCW 23-2A	AF	N	9.7	51	3	A	35.35940°	-114.5627°		
LCW 23-2B	AF	N	4.5	70	4.2	A				
SITE MEAN			**8.2**	**49.4**					**33.9**	**14.26**
LCW 24-1A	AF	N	348.7	47.6	7.1	A				
LCW 24-1B	AF/LTD	N	16.6	51.9	7.8	A	35.35940°	-114.5627°		
LCW 24-2A	TH/LTD	N	344.3	46.1	3.1	B				
LCW 24-2B	TH	N	11.7	47.5	4.7	A				
SITE MEAN			**359.9**	**49.1**					**12.5**	**54.64**
LCW 25-1	AF	N	7.6	54.9	1.7	A	35.36015°	-114.56274°		
LCW 25-2B	TH/LTD	N	61.3	44	2.8	B				

LCW 25-2C	AF	N	42.1	42.7	1.8	A				
LCW 25-3	TH	N	8.3	42.2	7.9	A				
SITE MEAN			**37.4**	**48.1**					**18.4**	**18.27**
LCW 28-1	AF	N	9.6	33.8	2.4	A				
LCW 28-2	TH	N	32.5	38	7.8	B	35.36009°	-114.55672°		
LCW 28-3	TH/LTD	N	27.3	43	3.4	B				
SITE MEAN			**9.4**	**39.1**					**21.9**	**32.88**

BOUSE INCISION SITE

SAMPLE NAME	DEMAG	POLARITY	DEC.	INC.	MAD	RANK	LAT	LONG	α	k
BC 6-1	AF	R	171.1	-33	10.1	A				
BC 6-2	AF	R	156.5	-24.6	8.7	A	35.360023°	-114.563134°		
BC 6-3	Thermal	R	148.8	-29.9	10	A				
BC 6-4	Thermal	R	166.7	-40	6.5	A				
SITE MEAN			**160.5**	**-32.2**					**12.2**	**58.1**

REVERSAL SITE										
SAMPLE NAME	DEMAG	POLARITY	DEC.	INC.	MAD	RANK	LAT	LONG	α	k
T-1	AF/LTD	R	191.1	-61.5	4	B				
T-2	AF/LTD	R	161.6	-55	6.2	B				
T-3	AF/LTD	R	133.1	-26.4	9.3	B				
T-4	AF/LTD	R	216.7	-32	3.1	B				
T-5	AF/LTD	AMBIG	282.8	61.1	3	B				
T-6	AF/LTD	R	175.5	-16.8	8.6	B				
T-7	AF/LTD	N/A				D				
T-8	AF/LTD	N	37.6	21.1	8.1	B	35.35868°	-114.56489°		
T-9	AF/LTD	N/A				D				
T-10	AF/LTD	N	27	34.5	7.9	A				
T-11	AF/LTD	N	16.9	44.9	6.1	A				
T-12	AF/LTD	N	333	57.4	10.7	B				
T-13	AF/LTD	N	42.1	50.4	6.7	A				
T-14	AF/LTD	N	30.8	67	10	B				
T-15B	AF/LTD	N	56.8	61	8.1	B				

GOLDEN SECTION SITE										
SAMPLE NAME	DEMAG	POLARITY	DEC.	INC.	MAD	RANK	LAT	LONG	α	k
GS 1-1	AF	N	12.6	56.1	10.9	B	35.381872°	-114.574136°		
GS 1-2	AF	N/A				D				
GS 3-1	AF	N	11.8	59.8	2.7	B				
GS 3-2	TH	N	22	1.1	7.5	B				
GS 3-3	AF	N/A				D	35.381872°	-114.574136°		
GS 3-4	TH	AMBIG	209.9	1.3	7.5	C				
GS 3-5	TH	R	200.7	-1.3	8.3	B				
GS 4-1	AF/LTD	R	187.4	-25.8	9.7	A				
GS 4-2	AF/LTD	R	185.4	-32.8	8.5	A	35.381872°	-114.574136°		
GS 4-3	TH	R	204.1	-32	11.2	C				

HIGH WALL WASH SITE										
SAMPLE NAME	DEMAG	POLARITY	DEC.	INC.	MAD	RANK	LAT	LONG	α	k
HWW 1	TH	N	344.1	52.2	5.4	B	35.381872°	-114.574136°		
HWW 2-1	TH	AMBIG	201.8	19.8	6.4	B	35.381872°	-114.574136°		
HWW 3-1	AF/LTD	N/A				D				
HWW 3-2	TH	AMBIG	137.3	46.9	7.6	A	35.381872°	-114.574136°		
HWW 3-3	TH	N	355.2	66.3	6.7	B				
HWW 5-1	AF/LTD	AMBIG	16.9	-33	10.4	C	35.381872°	-114.574136°		
HWW 5-2	TH	R	123.3	-45.7	10.2	A				
HWW 6-1	AF/LTD	R	137.1	-29.5	9.9	B				
HWW 6-2	TH	R	138	-33.2	14.5	C				
HWW 6-6	TH	N	305.3	61.1	3.1	B				
HWW 6-7	AF/LTD	R	198	-17.2	8.5	A	35.381872°	-114.574136°		
HWW 6-8	TH	N	322.5	66.7	5.6	A				
HWW 6-9	TH	N/A				D				
HWW 6-10	TH	N	282.8	68.3	7.9	C				
HWW 6-11	AF/LTD	R				C				
HWW 7-1	AF/LTD	R	197	-52	4.7	B	35.381872°	-114.574136°		
HWW 8-1	AF/LTD	R	177.6	-28.8	8.6	A	35.381872°	-114.574136°		
HWW 8-2	TH	N	304.4	16.5	10.2	B				
HWW 9-1	AF	N	345.9	71	9.3	B				
HWW 9-2	AF/LTD	N	330.7	76	3.1	B				
HWW 9-3	AF	N/A				D				
HWW 9-6	AF	N	348	66.4	4.8	B				
HWW 9-7	TH	N	10.3	65.6	2.7	B	35.381872°	-114.574136°		
HWW 9-8	AF	N	312.7	62	10.7	B				
HWW 9-9	TH	N	1.7	67.4	5.6	C				
HWW 9-10	TH	N	315.3	33.3	8.4	C				
HWW 9-11	TH	N	21.6	43.1	8.5	B				

HWW 10-1	AF	N	295.3	67.9	15	C	35.381872°	-114.574136°		
HWW 10-2	TH	N/A				D				
HWW 11-1	AF	N	4.8	67.9	4.6	B				
HWW 11-2	AF	N	356.6	53.3	2.4	A				
HWW 11-3	AF/LTD	N	334	72.6	11.3	C	35.381872°	-114.574136°		
HWW 11-4	TH	N/A				D				
HWW 11-7	TH	N	26.3	44.9	15	B				
HWW 12-1A	AF	N	53.1	61	6.2	B				
HWW 12-7	TH	N	6.3	56.7	5.2	B				
HWW 12-8	AF	N	23.3	62.5	3.4	A	35.381872°	-114.574136°		
HWW 12-9	TH	N	20.1	64	4.7	C				
HWW 12-10	TH	N	21.7	64	6.3	C				

NORTH WALL BASE

SAMPLE NAME	DEMAG	POLARITY	DEC.	INC.	MAD	RANK	LAT	LONG	α	k
SW-4A	LTD/AF	R	208.3	-15.3	8.9	A				
SW-5B	LTD/AF	R	204.3	-23.8	4.9	A	35.357790°	-114.569417°		
SW-6	LTD/AF	R	218	-30.8	7.3	A				
SW-7	LTD/AF	R	171.9	-30.1	2.8	A				
SITE MEAN			**201.1**	**-26.0**					**22.1**	**18.2**

WOLVERINE CREEK										
SAMPLE NAME	DEMAG	POLARITY	DEC.	INC.	MAD	RANK	LAT	LONG	α	k
WC 1-1	TH	R	167.6	-53.8	8.8	A				
WC 1-2	AF/LTD	R	166.7	-45.3	3.6	A	35.369370°	-114.580258°		
WC 1-3	AF/LTD	R	183.6	-54.4	7	A				
SITE MEAN			**172.2**	**-51.4**					**11.9**	**109.17**
WC 2-1	TH	R	172.9	-46.2	7.2	A				
WC 2-2	TH	R	167.4	-53.9	6.6	A	35.369370°	-114.580258°		
WC 2-4	AF/LTD	R	142.3	-46	4.3	A				
WC 2-5	AF/LTD	R	146.5	-50.7	4.7	A				
SITE MEAN			**174.7**	**-47.1**					**8.1**	**129.07**
WC 3-1B	TH	R	183.1	-50.5	4.1	A				
WC 3-2	AF/LTD	R	166.1	-44.9	4.9	A	35.369370°	-114.580258°		
WC 3-3	AF/LTD	R	164.7	-51.3	4.5	A				
WC 3-4	TH	R	176.2	-50.3	3.4	A				
SITE MEAN			**172.4**	**-49.5**					**7.2**	**161.95**
WC 4-1A	TH	R	177.4	-40.3	3.7	A				
WC 4-1B	TH	R	186.8	-38.1	9.7	B	35.369370°	-114.580258°		
WC 4-2A	TH	R	176.4	-49.4	8.6	B				
WC 4-3	AF/LTD	R	174	-45.6	5	A				
SITE MEAN			**177.0**	**-48.0**					**8.2**	**127.66**
WC 5-1	AF/LTD	R	209	-58.3	4	A				
WC 5-2	AF/LTD	R	181.6	-62.9	4.2	A	35.369370°	-114.580258°		
WC 5-3	TH	R	180.8	-56.8	6.6	A				
SITE MEAN			**190.7**	**-60.0**					**13.4**	**85.24**
WC 6-1A	AF/LTD	R	186.4	-62.8	1.9	A				
WC 6-1B	TH	R	202	-57.1	5.8	A	35.369370°	-114.580258°		
WC 6-2	AF/LTD	R	201.7	-71.1	1.8	A				
SITE MEAN			**196.9**	**-62.2**					**15.9**	**61.00**

WC 7-1	AF/LTD	R	182	-59.8	1.9	A	35.369370°	-114.580258°		
WC 7-2	AF/LTD	R	194.8	-55.6	4	A				
SITE MEAN			**186.6**	**-58.6**					**7.1**	**303.90**

Description of Table 2 data columns

DEMAG: Type of demagnetization (TH=Thermal, AF=Alternating field, LTD= Low temperature demagnetization), POLARITY: Magnetic polarity (R=Reverse, N=Normal), DEC: Magnetic declination, INC: Magnetic inclination, MAD: Mean angular deviation, RANK: Fidelity of magnetic components, LAT: Sample site latitude, LONG: Sample site longitude, α: Alpha 95 value, k: Precision parameter.

TABLE 3: LCW-ASH2 ASH DATA

SAMPLE	37 DECAY FACTOR	39 DECAY FACTOR	J	± J	40Ar*/ 39ArK	± 1σ	AGE (Ma)	± 1σ (no J)	± 1σ (with J)	K/Ca	± 1σ	%40Ar *	± 1σ
LCWASH2 #13	3.792578	1.00048	0.0007	0.000000764	12.109	0.177	15.286	0.222	0.223	19.6	7.0	90.5	1.3
LCWASH2 #13	3.795601	1.00048	0.0007	0.000000764	12.215	0.085	15.419	0.107	0.108	52.6	20.5	98.9	0.7
LCWASH2 #13	3.803325	1.00048	0.0007	0.000000764	12.787	0.040	16.138	0.051	0.054	55.1	6.4	99.7	0.4
LCWASH2 #13	3.794975	1.00048	0.0007	0.000000764	12.796	0.076	16.150	0.095	0.096	109.1	76.3	98.3	0.6
LCWASH2 #13	3.800401	1.00048	0.0007	0.000000764	12.797	0.066	16.151	0.083	0.084	60.2	18.2	99.2	0.5
LCWASH2 #13	3.796226	1.00048	0.0007	0.000000764	12.832	0.052	16.194	0.065	0.068	59.4	15.1	98.5	0.5
LCWASH2 #13	3.789557	1.00048	0.0007	0.000000764	12.930	0.073	16.317	0.091	0.093	23.6	2.9	97.5	0.5
LCWASH2 #13	3.790182	1.00048	0.0007	0.000000764	13.223	0.110	16.685	0.138	0.139	62.0	35.7	99.3	0.8
LCWASH2 #13	3.799252	1.00048	0.0007	0.000000764	13.316	0.074	16.802	0.093	0.095	38.5	7.7	98.0	0.5
LCWASH2 #13	3.798000	1.00048	0.0007	0.000000764	13.339	0.154	16.832	0.194	0.195	24.6	7.8	97.9	1.1
LCWASH2 #13	3.801602	1.00048	0.0007	0.000000764	13.594	0.059	17.151	0.074	0.076	50.2	11.6	99.3	0.4
LCWASH2 #13	3.798626	1.00048	0.0007	0.000000764	13.655	0.191	17.228	0.240	0.240	33.5	19.1	100.3	1.3

LCWASH2 #13	3.794349	1.00048	0.0007	0.000000764	13.666	0.093	17.243	0.116	0.118	23.2	5.1	97.7	0.6
LCWASH2 #13	3.797374	1.00048	0.0007	0.000000764	13.785	0.076	17.392	0.095	0.097	26.1	5.9	99.6	0.6
LCWASH2 #13	3.791952	1.00048	0.0007	0.000000764	14.137	0.084	17.833	0.105	0.107	37.1	8.8	99.1	0.5
LCWASH2 #13	3.802228	1.00048	0.0007	0.000000764	14.641	0.074	18.466	0.093	0.095	28.6	3.8	92.2	0.5
LCWASH2 #13	3.791327	1.00048	0.0007	0.000000764	68.881	0.376	85.274	0.454	0.463	23.3	8.5	98.5	0.4
LCWASH2 #13	3.800975	1.00048	0.0007	0.000000764	1081.8	3.0	1020.1	2.1	2.3	105.5	36.1	100.0	0.2
LCWASH2 #13	3.819766	1.00048	0.0007	0.000000765	11.205	0.063	14.141	0.079	0.080	157.4	190.3	98.6	0.6
LCWASH2 #13	3.812427	1.00048	0.0007	0.000000765	12.190	0.085	15.379	0.107	0.108	300.8	567.3	98.8	0.6
LCWASH2 #13	3.841446	1.00048	0.0007	0.000000765	12.221	0.048	15.418	0.060	0.062	43.6	6.2	99.6	0.4
LCWASH2 #13	3.841974	1.00048	0.0007	0.000000765	12.247	0.042	15.451	0.053	0.056	41.9	5.0	99.6	0.4
LCWASH2 #13	3.817878	1.00048	0.0007	0.000000765	12.722	0.070	16.047	0.087	0.089	104.3	77.3	99.7	0.5
LCWASH2 #13	3.826962	1.00048	0.0007	0.000000765	12.757	0.061	16.092	0.076	0.078	334.8	561.6	98.7	0.5
LCWASH2 #13	3.823914	1.00048	0.0007	0.000000765	12.788	0.049	16.130	0.061	0.063	58.0	8.1	94.5	0.4
LCWASH2 #13	3.842555	1.00048	0.0007	0.000000765	12.792	0.043	16.136	0.054	0.057	73.5	10.5	93.8	0.4

LCWASH2 #13	3.824544	1.00048	0.0007	0.000000765	12.797	0.060	16.142	0.075	0.077	85.1	30.2	99.9	0.5
LCWASH2 #13	3.815466	1.00048	0.0007	0.000000765	12.883	0.076	16.249	0.096	0.097	212.0	366.0	99.8	0.6
LCWASH2 #13	3.810647	1.00048	0.0007	0.000000765	13.258	0.141	16.721	0.177	0.178	53.3	45.4	97.4	1.0
LCWASH2 #13	3.813056	1.00048	0.0007	0.000000765	13.284	0.100	16.754	0.126	0.127	45.8	19.1	98.4	0.7
LCWASH2 #13	3.804579	1.00048	0.0007	0.000000765	13.319	0.161	16.797	0.202	0.202	44.6	40.0	97.3	1.1
LCWASH2 #13	3.814837	1.00048	0.0007	0.000000765	13.424	0.103	16.929	0.129	0.130	68.0	34.6	98.9	0.7
LCWASH2 #13	3.827593	1.00048	0.0007	0.000000765	13.446	0.080	16.957	0.100	0.102	~~-1008.1~~	7878.4	96.3	0.6
LCWASH2 #13	3.805207	1.00048	0.0007	0.000000765	13.463	0.110	16.978	0.139	0.140	204.8	436.7	99.4	0.8
LCWASH2 #13	3.806984	1.00048	0.0007	0.000000765	13.474	0.078	16.992	0.098	0.099	27.0	4.1	97.9	0.5
LCWASH2 #13	3.813684	1.00048	0.0007	0.000000765	13.560	0.068	17.099	0.085	0.087	18.2	2.2	97.9	0.5
LCWASH2 #13	3.822811	1.00048	0.0007	0.000000765	13.570	0.118	17.112	0.148	0.150	~~-176.4~~	388.8	98.9	0.8
LCWASH2 #13	3.828224	1.00048	0.0007	0.000000765	13.585	0.070	17.130	0.087	0.089	31.6	5.3	98.8	0.5
LCWASH2 #13	3.828855	1.00048	0.0007	0.000000765	13.612	0.078	17.165	0.097	0.099	65.5	30.1	98.8	0.5
LCWASH2 #13	3.810019	1.00048	0.0007	0.000000765	13.626	0.073	17.183	0.091	0.093	23.2	4.2	98.7	0.5

LCWASH2 #13	3.811275	1.00048	0.0007	0.000000765	13.634	0.108	17.192	0.135	0.137	~~666.3~~	6501.3	98.9	0.7
LCWASH2 #13	3.807612	1.00048	0.0007	0.000000765	13.646	0.084	17.207	0.106	0.108	27.8	5.5	98.6	0.6
LCWASH2 #13	3.816724	1.00048	0.0007	0.000000765	13.659	0.078	17.223	0.097	0.099	24.6	3.4	99.3	0.6
LCWASH2 #13	3.825175	1.00048	0.0007	0.000000765	13.660	0.056	17.226	0.070	0.072	17.4	1.3	99.5	0.4
LCWASH2 #13	3.830012	1.00048	0.0007	0.000000765	13.673	0.127	17.242	0.159	0.161	97.5	58.3	70.7	0.6
LCWASH2 #13	3.840813	1.00048	0.0007	0.000000765	13.681	0.085	17.251	0.107	0.109	33.7	8.1	99.8	0.6
LCWASH2 #13	3.820921	1.00048	0.0007	0.000000765	13.684	0.195	17.255	0.244	0.245	~~340.5~~	2441.1	98.4	1.4
LCWASH2 #13	3.818507	1.00048	0.0007	0.000000765	13.700	0.087	17.276	0.109	0.111	55.2	29.2	99.4	0.6
LCWASH2 #13	3.825805	1.00048	0.0007	0.000000765	13.718	0.057	17.298	0.072	0.074	25.9	3.0	99.2	0.4
LCWASH2 #13	3.819137	1.00048	0.0007	0.000000765	13.724	0.084	17.306	0.106	0.107	162.5	243.7	99.7	0.6
LCWASH2 #13	3.808240	1.00048	0.0007	0.000000765	13.737	0.148	17.322	0.186	0.187	19.8	5.3	96.2	1.0
LCWASH2 #13	3.816095	1.00048	0.0007	0.000000765	13.737	0.074	17.322	0.093	0.095	22.8	3.5	99.0	0.5
LCWASH2 #13	3.831275	1.00048	0.0007	0.000000765	13.781	0.083	17.378	0.104	0.106	28.2	7.7	99.0	0.6
LCWASH2 #13	3.831907	1.00048	0.0007	0.000000765	13.802	0.090	17.404	0.113	0.115	89.9	87.6	99.2	0.6

LCWASH2 #13	3.821551	1.00048	0.0007	0.000000765	13.808	0.093	17.411	0.116	0.118	22.5	4.2	100.7	0.7
LCWASH2 #13	3.822181	1.00048	0.0007	0.000000765	13.854	0.109	17.469	0.136	0.138	45.0	22.7	101.0	0.7
LCWASH2 #13	3.830644	1.00048	0.0007	0.000000765	13.921	0.080	17.553	0.100	0.102	392.3	1323.9	98.3	0.6
LCWASH2 #13	3.806357	1.00048	0.0007	0.000000765	14.091	0.067	17.766	0.084	0.087	95.5	51.4	99.6	0.5
LCWASH2 #13	3.809391	1.00048	0.0007	0.000000765	14.149	0.091	17.839	0.114	0.115	74.1	57.4	98.7	0.6
LCWASH2 #13	3.803952	1.00048	0.0007	0.000000765	14.297	0.705	18.024	0.884	0.885	1.0	0.1	100.4	4.9

TABLE 4: LCW-ASH3 ASH DATA

SAMPLE	37 DECAY FACTOR	39 DECAY FACTOR	J	± J	40Ar*/ 39ArK	± 1σ	AGE (Ma)	± 1σ (no J)	± 1σ (with J)	K/Ca	± 1σ	%40Ar *	± 1σ
LCWASH3 #8	11.272037	1.00086	0.0007	0.000000767	11.847	0.059	14.940	0.074	0.076	36.8	7.7	98.2	0.6
LCWASH3 #8	11.295443	1.00086	0.0007	0.000000767	11.917	0.032	15.028	0.040	0.043	49.1	4.9	98.3	0.3
LCWASH3 #8	11.285517	1.00086	0.0007	0.000000767	12.170	0.051	15.346	0.064	0.067	88.7	50.6	97.5	0.5
LCWASH3 #8	11.309262	1.00087	0.0007	0.000000767	12.219	0.060	15.408	0.075	0.077	132.4	112.7	98.1	0.5
LCWASH3 #8	11.312991	1.00087	0.0007	0.000000767	12.246	0.056	15.442	0.070	0.072	101.5	80.0	98.4	0.5

LCWASH3 #8	11.314700	1.00087	0.0007	0.000000767	12.258	0.045	15.457	0.057	0.059	44.2	14.1	98.5	0.4
LCWASH3 #8	11.293736	1.00086	0.0007	0.000000767	12.364	0.035	15.590	0.044	0.047	59.4	4.6	97.9	0.3
LCWASH3 #8	11.288773	1.00086	0.0007	0.000000767	12.442	0.048	15.687	0.060	0.063	39.2	10.1	98.9	0.4
LCWASH3 #8	11.287222	1.00086	0.0007	0.000000767	12.463	0.049	15.714	0.062	0.064	57.3	19.7	98.9	0.4
LCWASH3 #8	11.260584	1.00086	0.0007	0.000000767	12.486	0.050	15.743	0.063	0.065	134.7	159.6	98.6	0.4
LCWASH3 #8	11.268786	1.00086	0.0007	0.000000767	12.541	0.038	15.812	0.048	0.051	57.3	13.3	99.1	0.4
LCWASH3 #8	11.283967	1.00086	0.0007	0.000000767	12.557	0.039	15.832	0.049	0.052	46.4	9.1	98.5	0.3
LCWASH3 #8	11.303981	1.00087	0.0007	0.000000767	12.561	0.052	15.837	0.065	0.068	236.7	330.2	98.7	0.5
LCWASH3 #8	11.255481	1.00086	0.0007	0.000000767	12.606	0.045	15.894	0.057	0.059	46.9	13.1	97.8	0.4
LCWASH3 #8	11.280557	1.00086	0.0007	0.000000767	12.615	0.061	15.905	0.077	0.079	58.0	29.6	97.9	0.5
LCWASH3 #8	11.267083	1.00086	0.0007	0.000000767	12.621	0.036	15.913	0.045	0.048	60.2	11.1	98.6	0.3
LCWASH3 #8	11.317965	1.00087	0.0007	0.000000767	12.624	0.043	15.917	0.054	0.057	34.0	7.2	99.8	0.4
LCWASH3 #8	11.253935	1.00086	0.0007	0.000000767	12.648	0.048	15.947	0.060	0.062	71.3	35.2	98.5	0.4
LCWASH3 #8	11.263988	1.00086	0.0007	0.000000767	12.672	0.033	15.976	0.042	0.045	64.0	13.8	98.7	0.3

LCWASH3 #8	11.292030	1.00086	0.0007	0.000000767	12.700	0.031	16.012	0.039	0.042	72.6	12.8	99.2	0.3
LCWASH3 #8	11.258728	1.00086	0.0007	0.000000767	12.736	0.045	16.057	0.056	0.059	93.2	67.2	99.1	0.4
LCWASH3 #8	11.262286	1.00086	0.0007	0.000000767	12.742	0.036	16.064	0.045	0.048	102.8	50.2	99.5	0.3
LCWASH3 #8	11.305844	1.00087	0.0007	0.000000767	12.802	0.085	16.139	0.107	0.108	167.3	343.8	100.4	0.7
LCWASH3 #8	11.277148	1.00086	0.0007	0.000000767	12.803	0.046	16.141	0.058	0.061	44.9	18.7	99.6	0.4
LCWASH3 #8	11.278852	1.00086	0.0007	0.000000767	12.814	0.040	16.155	0.050	0.053	43.7	9.4	99.6	0.4
LCWASH3 #8	11.302273	1.00087	0.0007	0.000000767	12.916	0.061	16.283	0.076	0.078	110.3	105.5	99.9	0.5
LCWASH3 #8	11.300410	1.00087	0.0007	0.000000767	13.246	0.111	16.696	0.139	0.141	~~-17994.1~~	5664987.7	96.8	0.8

TABLE 5: RC15-LCW-111 ASH DATA

SAMPLE	37 DECAY FACTOR	39 DECAY FACTOR	J	± J	40Ar*/ 39ArK	± 1σ	AGE (Ma)	± 1σ (no J)	± 1σ (with J)	K/Ca	± 1σ	%40Ar*	± 1σ
RC15-LCW-111 #10	10.621249	1.00084	0.0007	0.000000904	4.377	0.630	5.489	0.788	0.788	9.3	6.5	59.6	8.6
RC15-LCW-111 #10	10.706213	1.00085	0.0007	0.000000904	5.361	0.674	6.720	0.843	0.843	~~-7.1~~	5.9	71.1	8.9
RC15-LCW-111 #10	10.655153	1.00084	0.0007	0.000000904	5.671	0.306	7.108	0.382	0.382	15.1	10.6	75.6	4.0

RC15-LCW-111 #10	10.673906	1.00084	0.0007	0.000000904	6.260	0.226	7.845	0.283	0.283	~~-35.7~~	51.8	76.8	2.7
RC15-LCW-111 #10	10.597493	1.00084	0.0007	0.000000904	6.377	0.717	7.992	0.897	0.897	~~-17.8~~	23.6	63.4	7.1
RC15-LCW-111 #10	10.680653	1.00085	0.0007	0.000000904	6.662	0.397	8.347	0.497	0.497	34.1	62.2	79.0	4.7
RC15-LCW-111 #10	10.733456	1.00085	0.0007	0.000000904	6.441	0.173	8.071	0.216	0.217	134.2	366.9	76.6	2.0
RC15-LCW-111 #10	10.619498	1.00084	0.0007	0.000000904	7.564	0.324	9.475	0.405	0.405	11.6	10.4	77.8	3.3
RC15-LCW-111 #10	10.651641	1.00084	0.0007	0.000000904	7.698	0.617	9.642	0.771	0.771	9.2	11.9	85.9	6.8
RC15-LCW-111 #10	10.599240	1.00084	0.0007	0.000000904	7.853	0.333	9.835	0.416	0.416	24.0	41.4	76.3	3.2
RC15-LCW-111 #10	10.697686	1.00085	0.0007	0.000000904	8.146	0.422	10.201	0.527	0.527	4.7	1.3	83.6	4.3
RC15-LCW-111 #10	10.617748	1.00084	0.0007	0.000000904	8.171	0.473	10.232	0.591	0.591	6.8	4.7	62.3	3.6
RC15-LCW-111 #10	10.614540	1.00084	0.0007	0.000000904	8.526	0.340	10.676	0.425	0.425	~~-29.6~~	84.0	80.4	3.2
RC15-LCW-111 #10	10.672146	1.00084	0.0007	0.000000904	8.792	0.401	11.008	0.500	0.501	~~-6.7~~	4.4	96.4	4.4
RC15-LCW-111 #10	10.612790	1.00084	0.0007	0.000000904	8.812	0.436	11.034	0.544	0.544	~~-54.3~~	321.4	77.4	3.8
RC15-LCW-111 #10	10.668628	1.00084	0.0007	0.000000904	8.879	0.459	11.117	0.573	0.573	~~-7.4~~	6.0	80.4	4.1
RC15-LCW-111 #10	10.639942	1.00084	0.0007	0.000000904	9.293	0.348	11.634	0.434	0.434	21.2	27.2	85.5	3.2

RC15-LCW-111 #10	10.819317	1.00085	0.0007	0.000000904	9.552	0.142	11.957	0.178	0.178	14.1	4.3	88.4	1.3
RC15-LCW-111 #10	10.643158	1.00084	0.0007	0.000000904	9.835	0.278	12.310	0.347	0.348	~~-45.6~~	95.5	91.1	2.5
RC15-LCW-111 #10	10.694160	1.00085	0.0007	0.000000904	10.136	0.302	12.685	0.377	0.377	4.9	1.5	85.1	2.5
RC15-LCW-111 #10	10.623000	1.00084	0.0007	0.000000904	10.223	0.328	12.793	0.410	0.410	4.6	1.4	85.8	2.7
RC15-LCW-111 #10	10.677132	1.00084	0.0007	0.000000904	10.305	0.212	12.896	0.265	0.265	18.3	14.2	93.9	1.9
RC15-LCW-111 #10	10.784891	1.00085	0.0007	0.000000904	10.339	0.510	12.938	0.636	0.636	5.3	3.3	68.2	3.3
RC15-LCW-111 #10	10.644912	1.00084	0.0007	0.000000904	10.402	0.306	13.016	0.381	0.382	~~-37.9~~	74.3	92.1	2.7
RC15-LCW-111 #10	10.602590	1.00084	0.0007	0.000000904	10.557	0.489	13.210	0.610	0.610	12.2	25.5	85.0	3.9
RC15-LCW-111 #9	10.846849	1.00085	0.0007	0.000000842	10.609	0.200	13.285	0.249	0.249	21.7	15.4	70.4	1.3
RC15-LCW-111 #10	10.611041	1.00084	0.0007	0.000000904	10.750	0.184	13.451	0.230	0.231	35.6	60.1	86.3	1.4
RC15-LCW-111 #10	10.783113	1.00085	0.0007	0.000000904	10.833	0.400	13.554	0.499	0.499	~~-35.5~~	116.0	89.6	3.3
RC15-LCW-111 #10	10.646667	1.00084	0.0007	0.000000904	10.835	0.453	13.557	0.565	0.565	~~-66.0~~	460.5	92.0	3.8
RC15-LCW-111 #10	10.716366	1.00085	0.0007	0.000000904	11.054	0.536	13.830	0.668	0.668	11.8	14.7	83.2	4.0
RC15-LCW-111 #9	10.838210	1.00085	0.0007	0.000000842	11.076	0.344	13.868	0.429	0.429	~~-6.8~~	4.3	69.4	2.1

RC15-LCW-111 #9	10.817534	1.00085	0.0007	0.000000842	11.102	0.178	13.900	0.222	0.223	14.1	7.1	85.7	1.3
RC15-LCW-111 #10	10.731687	1.00085	0.0007	0.000000904	11.133	0.321	13.928	0.400	0.400	~~-10.6~~	9.3	92.4	2.6
RC15-LCW-111 #9	10.839996	1.00085	0.0007	0.000000842	11.213	0.424	14.039	0.529	0.529	~~-683.9~~	63121.9	85.8	3.2
RC15-LCW-111 #9	10.843571	1.00085	0.0007	0.000000842	11.242	0.154	14.075	0.192	0.193	~~-178.0~~	1228.6	97.2	1.3
RC15-LCW-111 #10	10.653397	1.00084	0.0007	0.000000904	11.292	0.239	14.126	0.298	0.299	128.3	815.5	96.0	2.0
RC15-LCW-111 #10	10.822588	1.00085	0.0007	0.000000904	11.480	0.546	14.360	0.681	0.681	9.5	12.8	83.3	3.9
RC15-LCW-111 #10	10.656910	1.00084	0.0007	0.000000904	11.627	0.412	14.544	0.513	0.514	42.6	103.5	68.2	2.4
RC15-LCW-111 #9	10.815751	1.00085	0.0007	0.000000842	11.637	0.316	14.567	0.393	0.394	5.9	2.8	90.7	2.4
RC15-LCW-111 #10	10.789929	1.00085	0.0007	0.000000904	11.710	0.088	14.647	0.110	0.111	41.7	33.5	96.1	0.7
RC15-LCW-111 #10	10.704448	1.00085	0.0007	0.000000904	11.720	0.246	14.660	0.306	0.307	~~-134.6~~	790.7	98.4	2.0
RC15-LCW-111 #9	10.807137	1.00085	0.0007	0.000000842	11.720	0.322	14.671	0.402	0.402	17.8	25.4	86.6	2.3
RC15-LCW-111 #9	10.810701	1.00085	0.0007	0.000000842	11.786	0.285	14.753	0.355	0.355	26.7	38.6	73.0	1.7
RC15-LCW-111 #9	10.802387	1.00085	0.0007	0.000000842	11.805	0.264	14.776	0.329	0.330	27.2	26.4	75.5	1.7
RC15-LCW-111 #9	10.851916	1.00085	0.0007	0.000000842	11.864	0.286	14.850	0.356	0.357	8.1	4.1	89.6	2.1

RC15-LCW-111 #9	10.808919	1.00085	0.0007	0.000000842	12.055	0.376	15.088	0.469	0.469	~~-11.8~~	14.0	82.8	2.5
RC15-LCW-111 #10	10.791708	1.00085	0.0007	0.000000904	12.170	0.087	15.219	0.108	0.110	13.1	2.8	98.4	0.7
RC15-LCW-111 #10	10.781336	1.00085	0.0007	0.000000904	12.197	0.191	15.254	0.238	0.239	~~-108.4~~	612.2	95.5	1.5
RC15-LCW-111 #10	10.778078	1.00085	0.0007	0.000000904	12.221	0.079	15.284	0.099	0.101	84.1	75.2	94.8	0.6
RC15-LCW-111 #10	10.636434	1.00084	0.0007	0.000000904	12.221	0.147	15.284	0.184	0.185	13.9	3.6	96.0	1.1
RC15-LCW-111 #10	10.729918	1.00085	0.0007	0.000000904	12.270	0.142	15.345	0.177	0.178	~~-29.1~~	40.9	98.4	1.1
RC15-LCW-111 #10	10.721372	1.00085	0.0007	0.000000904	12.288	0.129	15.368	0.160	0.162	13.7	5.6	98.6	1.0
RC15-LCW-111 #10	10.690928	1.00085	0.0007	0.000000904	12.289	0.111	15.368	0.138	0.139	~~-184.5~~	1056.0	89.3	0.8
RC15-LCW-111 #10	10.626211	1.00084	0.0007	0.000000904	12.405	0.387	15.513	0.482	0.482	26.4	71.5	90.8	2.8
RC15-LCW-111 #10	10.678892	1.00084	0.0007	0.000000904	12.406	0.172	15.514	0.214	0.215	~~-59.1~~	140.0	99.1	1.3
RC15-LCW-111 #10	10.660131	1.00084	0.0007	0.000000904	12.443	0.346	15.560	0.430	0.431	14.4	18.2	93.0	2.5
RC15-LCW-111 #10	10.663646	1.00084	0.0007	0.000000904	12.445	0.373	15.563	0.465	0.465	~~-133.1~~	1170.2	93.8	2.8
RC15-LCW-111 #10	10.724908	1.00085	0.0007	0.000000904	12.455	0.094	15.575	0.117	0.119	2.6	0.6	97.3	0.7
RC15-LCW-111 #10	10.719605	1.00085	0.0007	0.000000904	12.466	0.352	15.589	0.438	0.438	8.6	6.8	93.6	2.6

RC15-LCW-111 #10	10.687404	1.00085	0.0007	0.000000904	12.483	0.231	15.610	0.287	0.288	~~-10.7~~	7.1	98.9	1.8
RC15-LCW-111 #10	10.707978	1.00085	0.0007	0.000000904	12.532	0.455	15.671	0.567	0.567	~~-4.2~~	2.5	94.2	3.4
RC15-LCW-111 #10	10.634681	1.00084	0.0007	0.000000904	12.548	0.456	15.690	0.568	0.569	14.8	19.4	94.1	3.4
RC15-LCW-111 #10	10.795415	1.00085	0.0007	0.000000904	12.615	0.131	15.774	0.162	0.164	~~-30.6~~	25.6	97.7	1.0
RC15-LCW-111 #9	10.833000	1.00085	0.0007	0.000000842	12.617	0.273	15.788	0.340	0.341	~~-63.8~~	201.9	96.4	2.0
RC15-LCW-111 #10	10.682413	1.00085	0.0007	0.000000904	12.666	0.242	15.838	0.301	0.301	~~-48.7~~	110.4	94.0	1.7
RC15-LCW-111 #10	10.609292	1.00084	0.0007	0.000000904	12.679	0.469	15.853	0.584	0.585	17.2	32.2	86.7	3.2
RC15-LCW-111 #10	10.723140	1.00085	0.0007	0.000000904	12.726	0.153	15.913	0.191	0.192	8.2	2.1	99.0	1.1
RC15-LCW-111 #10	10.774525	1.00085	0.0007	0.000000904	12.784	0.221	15.984	0.275	0.276	24.3	21.7	96.1	1.6
RC15-LCW-111 #9	10.826157	1.00085	0.0007	0.000000842	12.823	0.403	16.045	0.502	0.503	28.8	73.9	70.4	2.2
RC15-LCW-111 #9	10.827941	1.00085	0.0007	0.000000842	12.907	0.451	16.150	0.562	0.562	4.9	2.1	80.6	2.8
RC15-LCW-111 #9	10.841784	1.00085	0.0007	0.000000842	12.913	0.213	16.157	0.265	0.266	8.3	4.5	87.2	1.4
RC15-LCW-111 #10	10.714599	1.00085	0.0007	0.000000904	12.984	0.236	16.234	0.293	0.294	11.6	8.2	94.2	1.7
RC15-LCW-111 #10	10.627963	1.00084	0.0007	0.000000904	13.049	0.160	16.315	0.199	0.200	~~-25.6~~	28.6	99.1	1.1

RC15-LCW-111 #10	10.605940	1.00084	0.0007	0.000000904	13.061	0.453	16.329	0.564	0.565	17.4	31.1	80.2	2.7
RC15-LCW-111 #10	10.800607	1.00085	0.0007	0.000000904	13.094	0.077	16.371	0.096	0.098	16.1	3.5	98.9	0.5
RC15-LCW-111 #10	10.661889	1.00084	0.0007	0.000000904	13.301	0.117	16.628	0.146	0.147	20.6	11.9	95.7	0.8
RC15-LCW-111 #10	10.793635	1.00085	0.0007	0.000000904	13.338	0.165	16.674	0.205	0.206	~~-159.7~~	915.6	92.7	1.1
RC15-LCW-111 #10	10.631468	1.00084	0.0007	0.000000904	13.460	0.211	16.826	0.262	0.263	88.2	441.0	91.1	1.4
RC15-LCW-111 #10	10.798826	1.00085	0.0007	0.000000904	13.618	0.085	17.023	0.106	0.108	41.1	30.9	99.5	0.6
RC15-LCW-111 #10	10.728149	1.00085	0.0007	0.000000904	13.734	0.415	17.167	0.516	0.517	17.2	37.1	91.3	2.7
RC15-LCW-111 #10	10.689166	1.00085	0.0007	0.000000904	13.784	0.108	17.228	0.135	0.137	260.8	1938.8	96.9	0.7
RC15-LCW-111 #10	10.769642	1.00085	0.0007	0.000000904	13.798	0.121	17.247	0.151	0.153	372.3	4468.5	99.5	0.8
RC15-LCW-111 #9	10.834786	1.00085	0.0007	0.000000842	13.889	0.333	17.373	0.415	0.416	5.9	3.1	75.5	1.8
RC15-LCW-111 #10	10.629715	1.00084	0.0007	0.000000904	13.913	0.307	17.389	0.381	0.382	~~-11.5~~	15.8	105.4	2.3
RC15-LCW-111 #9	10.850127	1.00085	0.0007	0.000000842	13.915	0.135	17.404	0.168	0.169	18.7	6.3	79.8	0.8
RC15-LCW-111 #10	10.786669	1.00085	0.0007	0.000000904	13.985	0.078	17.479	0.097	0.099	57.2	54.4	93.7	0.5
RC15-LCW-111 #10	10.695923	1.00085	0.0007	0.000000904	14.131	0.228	17.661	0.283	0.284	4.9	1.0	99.1	1.5

RC15-LCW-111 #10	10.670387	1.00084	0.0007	0.000000904	14.248	0.336	17.805	0.417	0.418	126.4	1220.7	104.5	2.4
RC15-LCW-111 #10	10.638188	1.00084	0.0007	0.000000904	14.337	0.235	17.917	0.292	0.293	~~-36.7~~	46.0	95.3	1.5
RC15-LCW-111 #10	10.776301	1.00085	0.0007	0.000000904	14.672	0.142	18.333	0.177	0.179	28.3	25.1	94.5	0.9
RC15-LCW-111 #10	10.824372	1.00085	0.0007	0.000000904	15.522	0.424	19.389	0.526	0.527	16.1	26.3	102.0	2.6
RC15-LCW-111 #10	10.685642	1.00085	0.0007	0.000000904	22.267	0.312	27.751	0.386	0.387	16.5	9.3	81.2	1.1
RC15-LCW-111 #9	10.813968	1.00085	0.0007	0.000000842	52.906	0.349	65.299	0.423	0.430	~~-31.3~~	34.4	98.6	0.5
RC15-LCW-111 #9	10.803871	1.00085	0.0007	0.000000842	54.749	0.269	67.531	0.326	0.336	125.3	292.9	95.5	0.4
RC15-LCW-111 #10	10.604337	1.00084	0.0007	0.000000904	68.006	0.626	83.448	0.750	0.758	~~-9.7~~	10.2	97.3	0.6
RC15-LCW-111 #10	10.711215	1.00085	0.0007	0.000000904	99.764	0.612	121.135	0.719	0.735	11.6	9.2	99.5	0.5
RC15-LCW-111 #9	10.848488	1.00085	0.0007	0.000000842	414.831	2.165	457.998	2.111	2.166	22.0	29.8	99.6	0.3
RC15-LCW-111 #10	10.771269	1.00085	0.0007	0.000000904	877.240	4.726	859.936	3.685	3.791	~~-15.8~~	9.7	99.9	0.2
RC15-LCW-111 #10	10.712833	1.00085	0.0007	0.000000904	1021.436	3.291	969.005	2.416	2.604	76.0	136.4	100.0	0.2

FIGURES

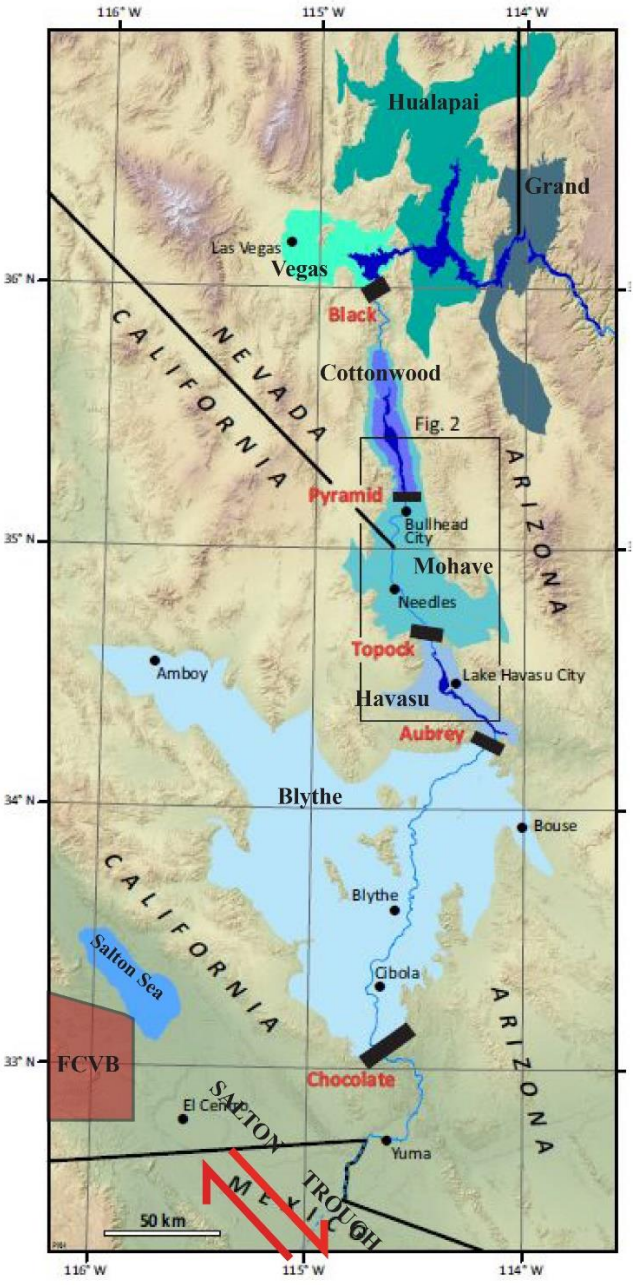

FIGURE 1: Lower Colorado Corridor Map

Map illustrating the extent of mapped paleo-Lake sediments within the Lower Colorado River Corridor. Paleo lakes Vegas, Hualapai, and Grand represent pre-Colorado River sediments; while Cottonwood, Mohave, Havasu, Blythe, and Fish Creek-Vallecito Basin (FCVB) represent syn-Colorado River aged sediments. Black bars show locations of paleo-divides between valleys. (Modified from Pearthree and House, 2014)

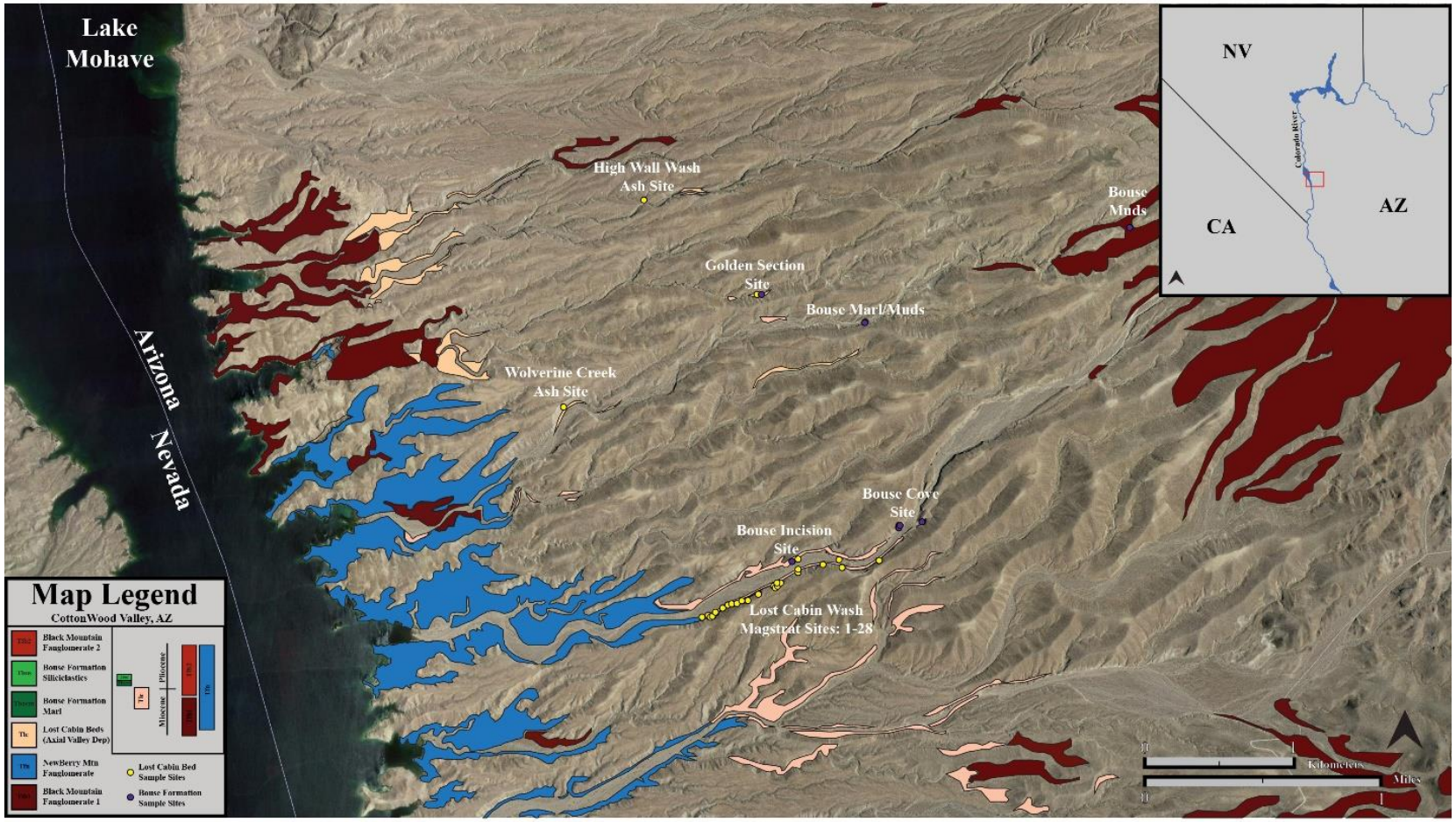

FIGURE 2: Pre-Bouse Sediment Map

Arial map of mapped Cottonwood Valley sediments from this study. Blue polygons represent granitic fanglomerate sediments fed from the Newberry Mountains to the west. Maroon polygons represent volcanic fanglomerate sediments shed from the Black Mountains to the east. Tan polygons represent the fine-grained axial valley Lost Cabin beds.
(Modified from House et al., unpublished)

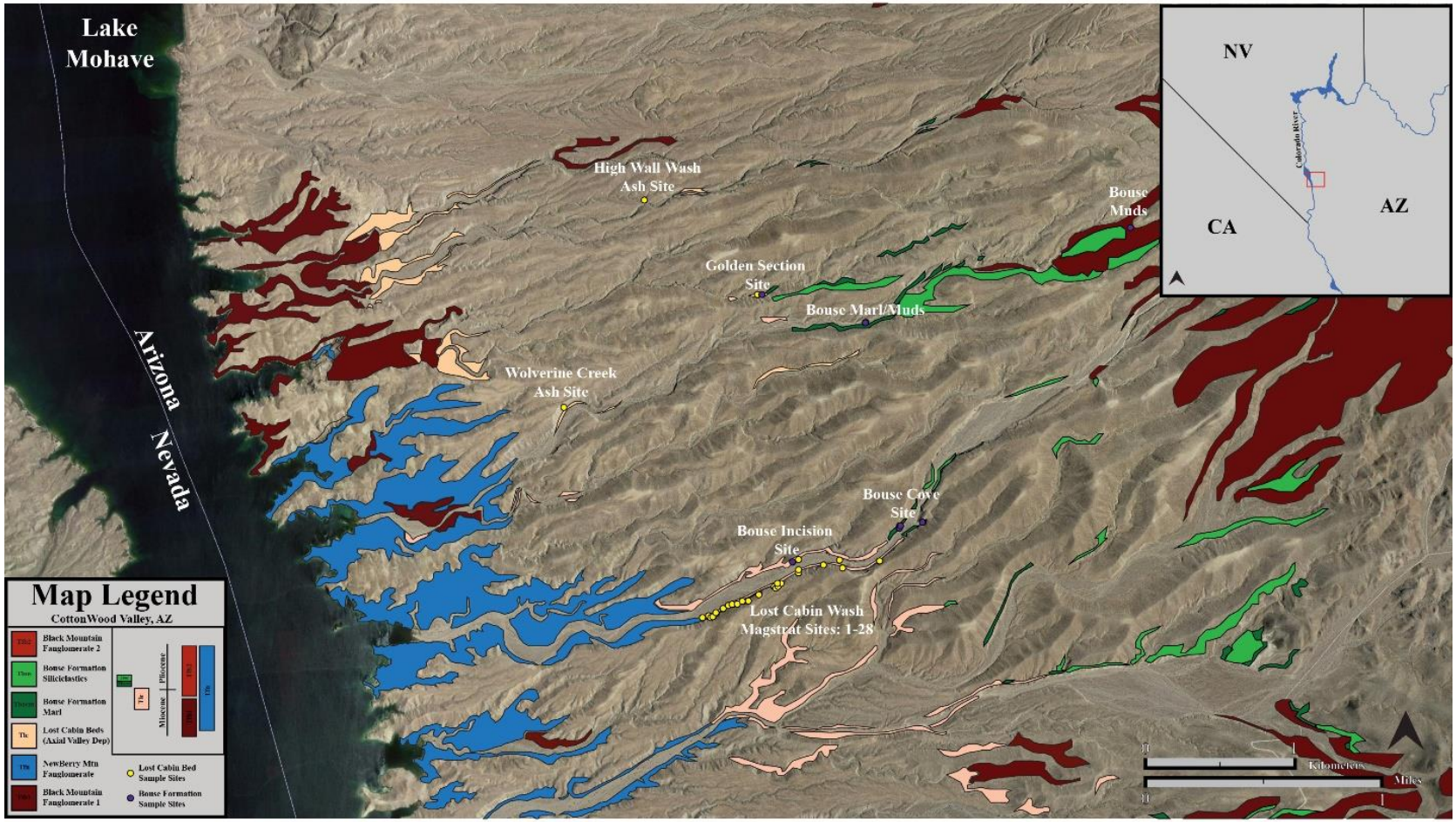

FIGURE 3: Syn-Bouse Sediment Map

Arial map of mapped Cottonwood Valley sediments from this study. Dark green polygons represent Bouse Marl deposits. Light green polygons represent Bouse siliciclastic (sandstone, siltstone, mudstone) deposits. (Modified from House et al., unpublished)

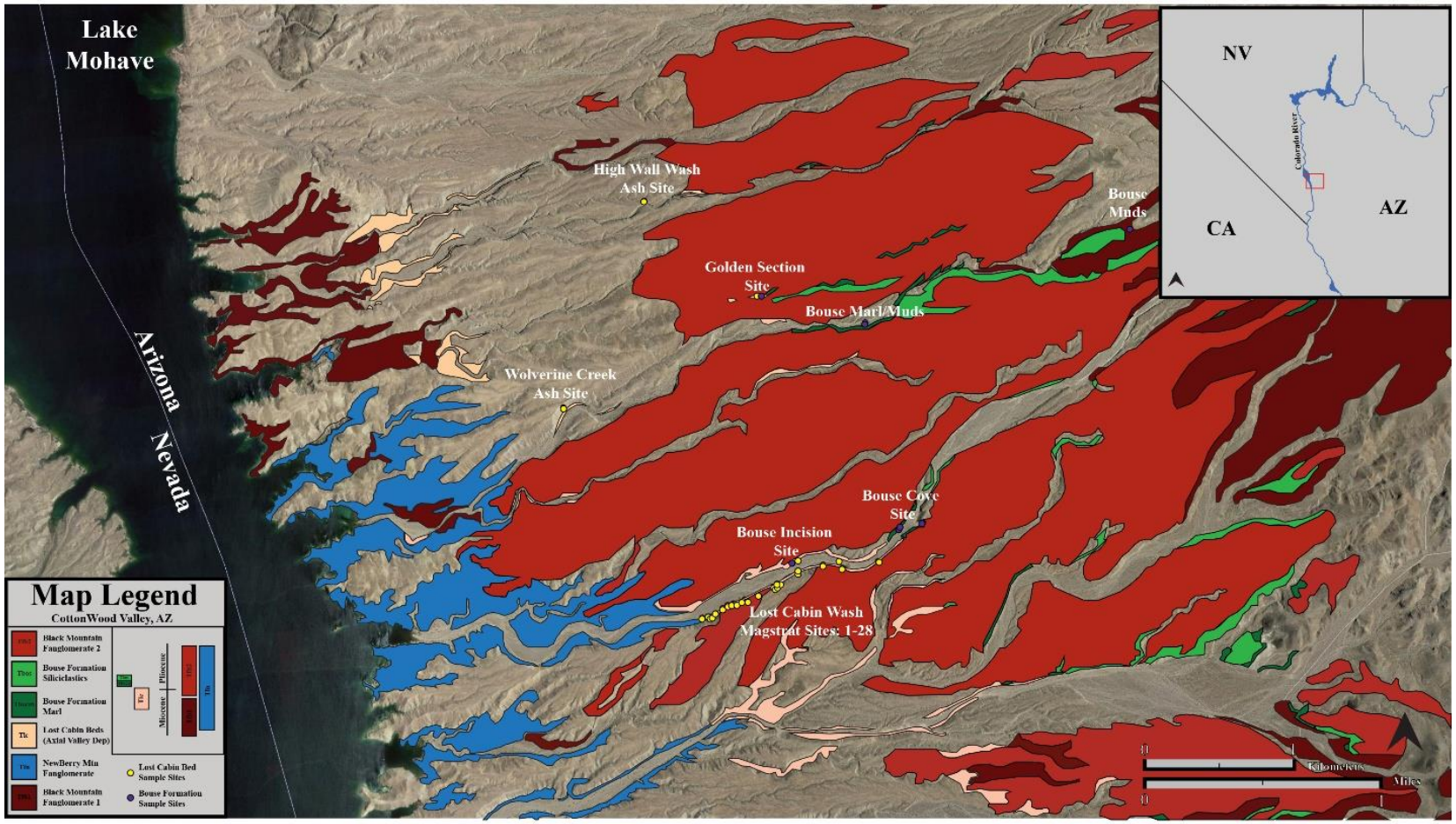

FIGURE 4: Post-Bouse Sediment Map

Arial map of mapped Cottonwood Valley sediments from this study. Red polygons represent post-Bouse deposition of volcanic fanglomerate sediments from the Black Mountains to the east. (Modified from House et al., unpublished)

FIGURE 5: Sample Site Locality Map

Arial map of Cottonwood Valley sample site locations from this study. Yellow circles represent pre-Bouse Lost Cabin bed paleomagnetic sample sites, while purple circles represent Bouse-aged paleomagnetic sample sites.

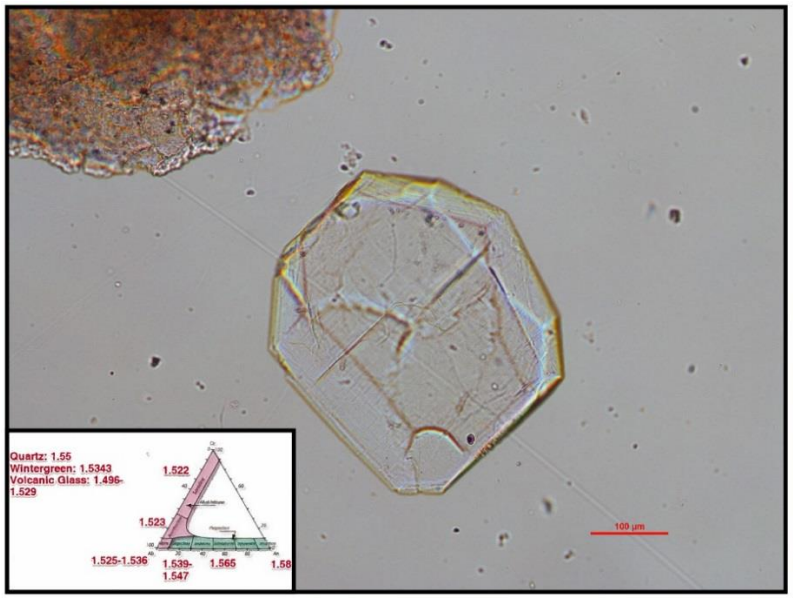

FIGURE 6A: Pristine Sanidine Grain Example
Example of pristine sanidine grain from LCW-ASH2 used for $^{40}Ar/^{39}Ar$ age determination. Note the distinct yellow Becke line on the grains rim, caused by the difference in refractive index between the sanidine (1.522) & wintergreen immersion oil (1.5343).

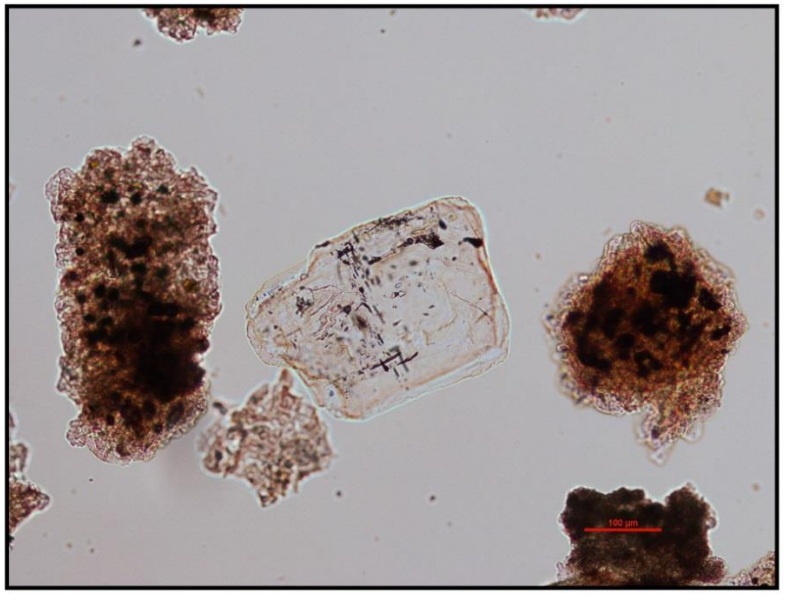

FIGURE 6B: Defective Sanidine Grain Example
Example of defective sanidine grain that was avoided $^{40}Ar/^{39}Ar$ age determination. Note the black glass inclusions that seemingly follow cleavage planes and defect sites.

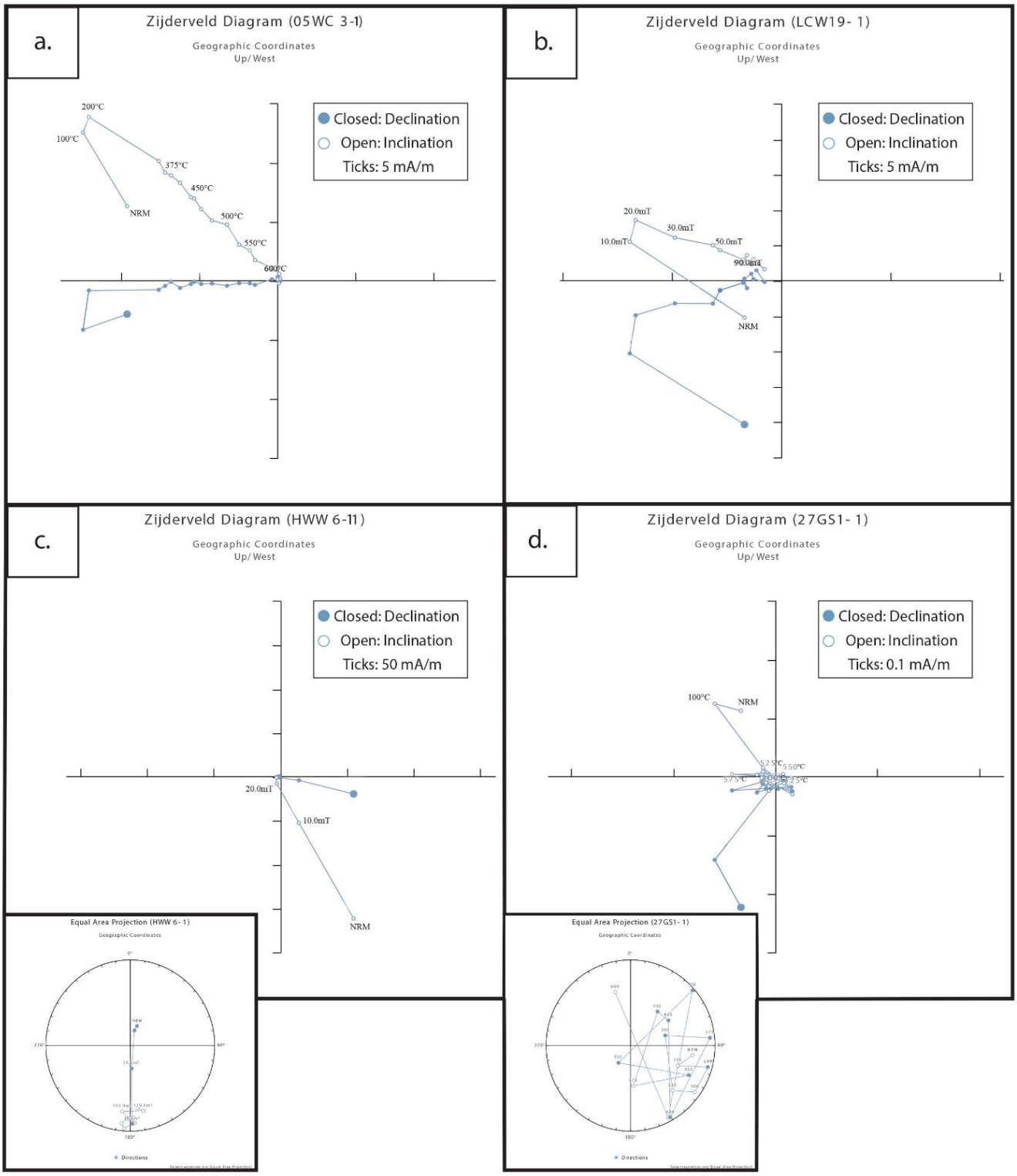

FIGURE 7: Representative Zijderveld Diagrams

Representative Zijderveld (1967) diagrams and equal area projections used for this study. Closed circles represent the horizontal (declination) vector projection. Open circles represent the vertical (inclination) vector projection. Demagnetization steps are in Celsius and milliTesla. a) Class "A" data. b) Class "B" data. c) Class "C" data. d) Class "D" data.

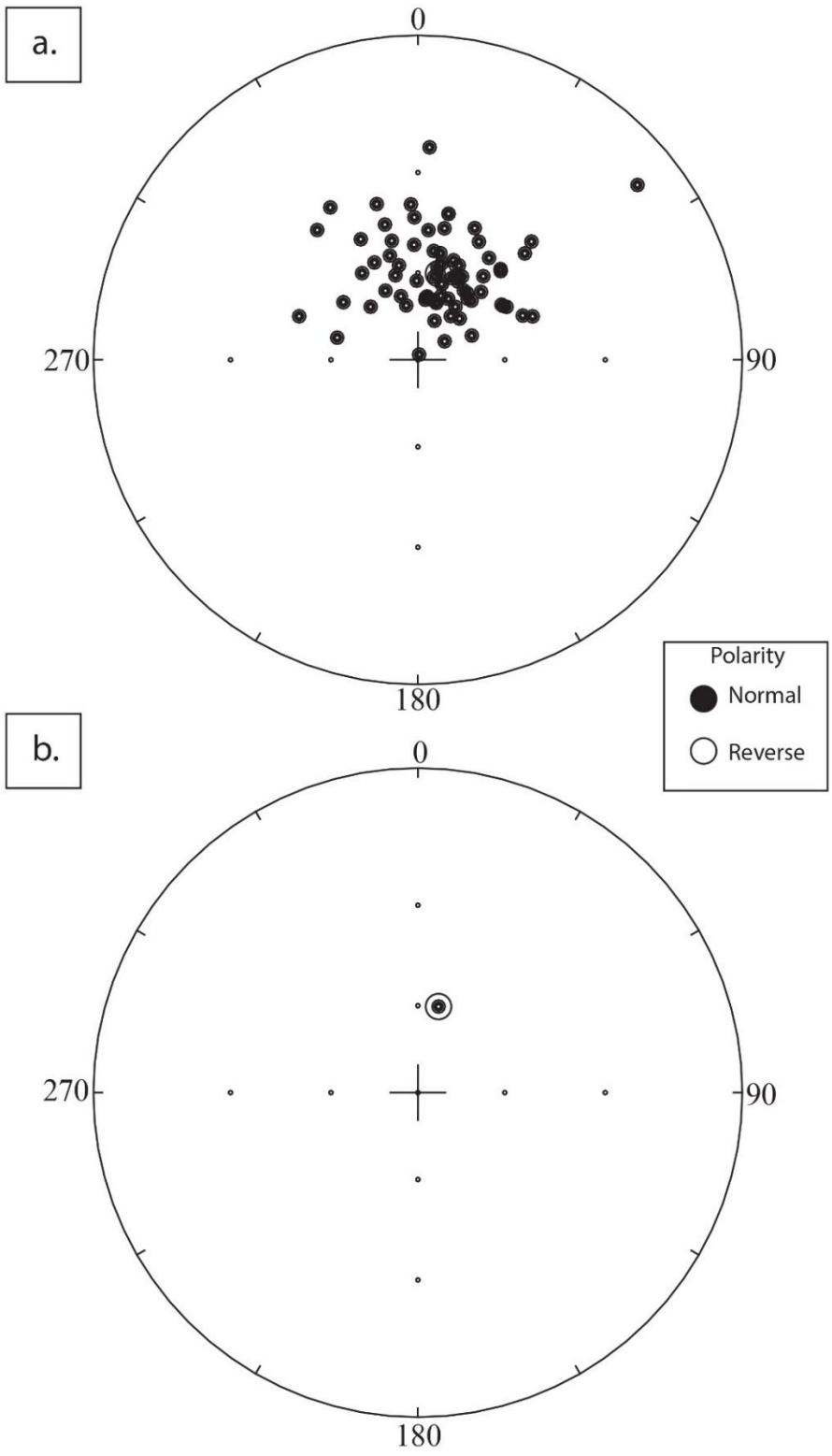

FIGURE 8: VRM Equal Area Plots

a) Equal area projection of all VRM components from sample sites. b) Mean direction of VRM components with associated α_{95} cone of confidence. Closed circles represent normal polarity.

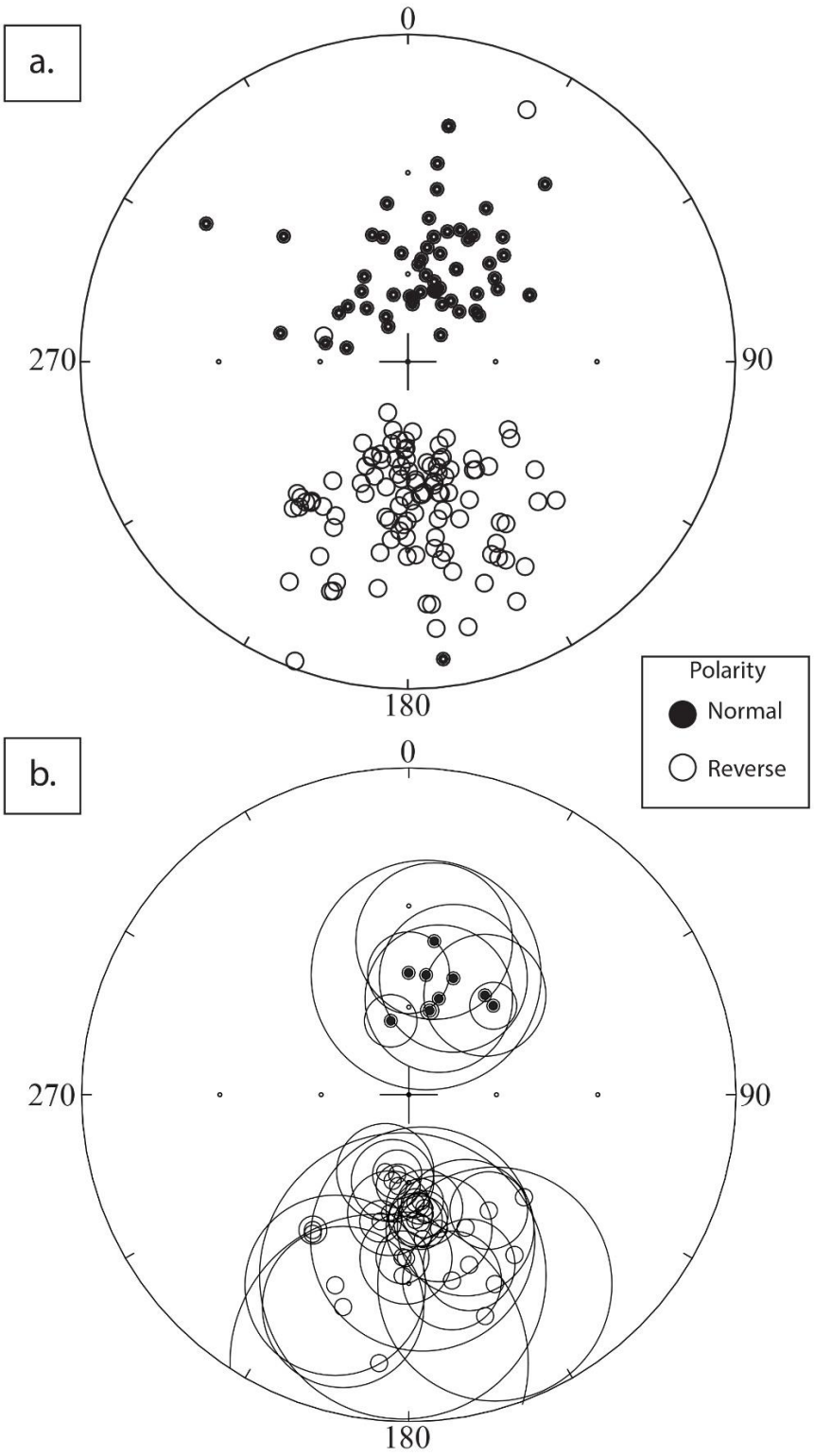

FIGURE 9: ChRM Equal Area Plots

a) Equal area projection of all sample ChRM components. b) ChRM site means with associated α_{95} cones of confidence. Closed circles represent normal polarity, open circles represent reverse polarity.

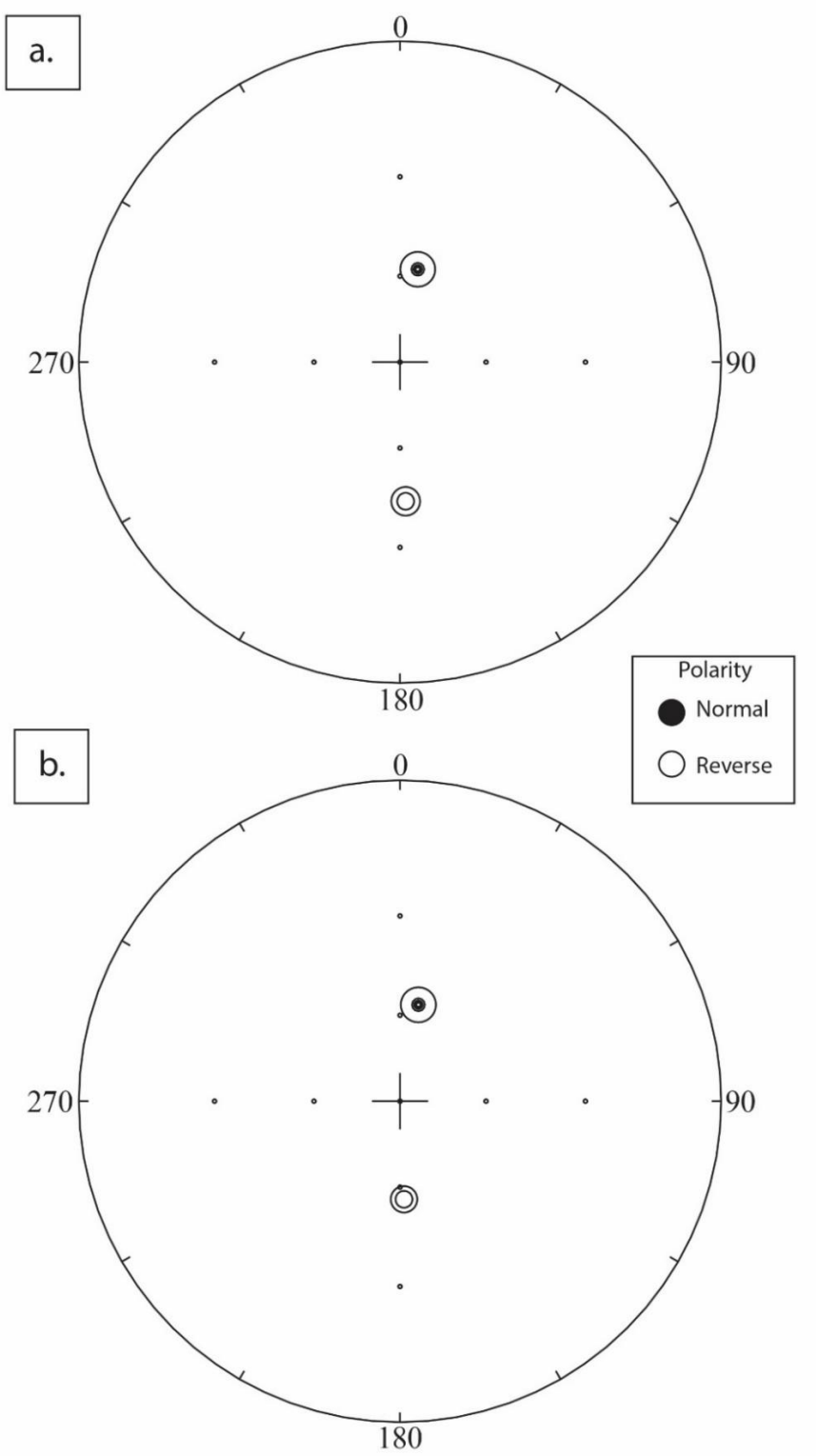

FIGURE 10: Uncorrected and Corrected Site Mean Equal Area Plots

a) Equal area projection with mean directions of normal and reverse ChRM components from all sample sites with associated α_{95} cones of confidence. b) Mean direction of ChRM components after Tauxe et al. (2004) E/I correction. Closed circles represent normal polarity, open circles represent reverse polarity.

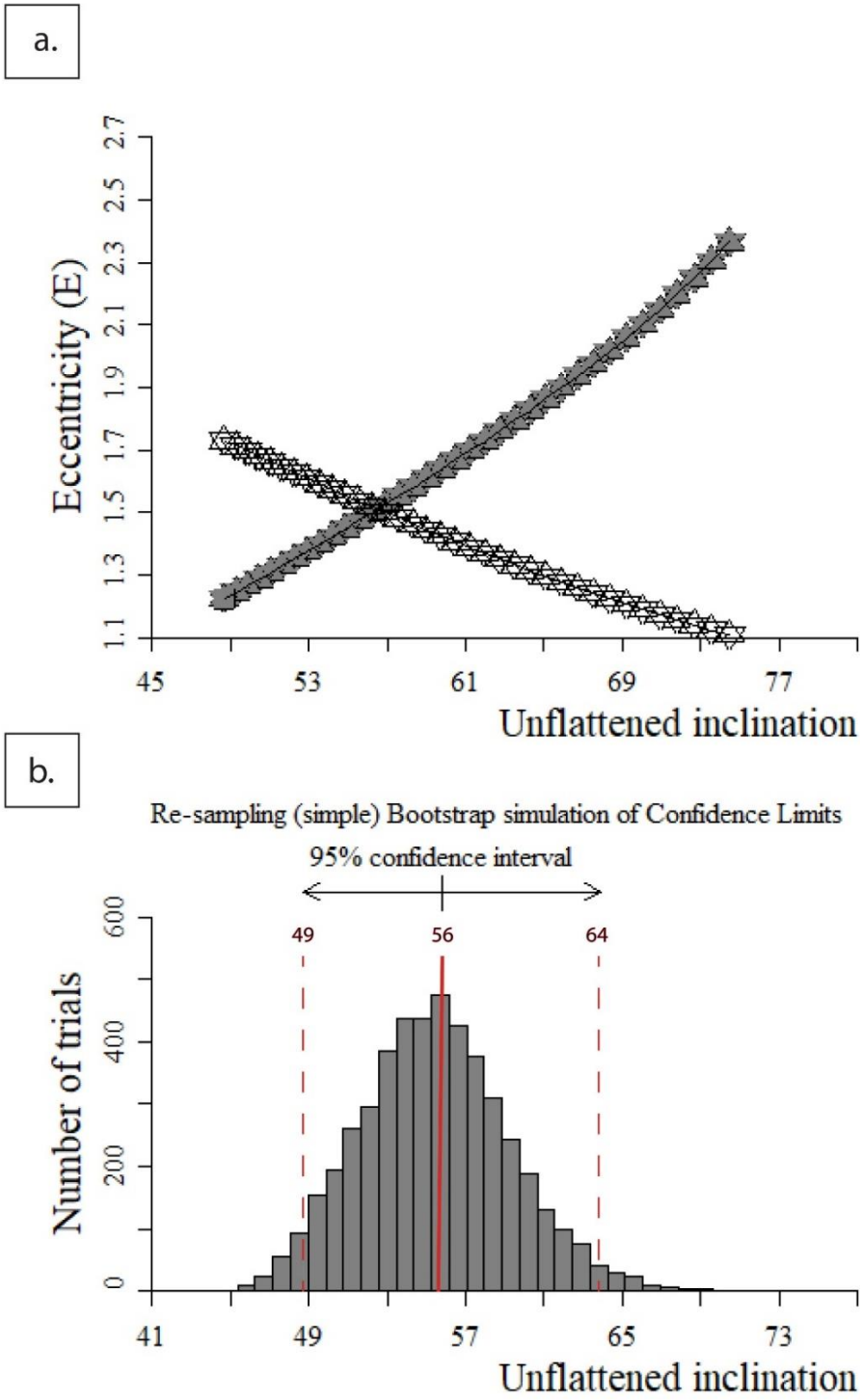

FIGURE 11: Elongation / Inclination Unflattening

Results of elongation/inclination correction method of Tauxe (2004) using normal and reverse directions. a) Open stars represent the TK03.GAD field model, while the closed stars represent the results of 5000 bootstrapped paleomagnetic inclinations 8. Intersection point between the model and data represents the corrected inclination. b) Distribution of corrected inclination with 95% c.i. values.

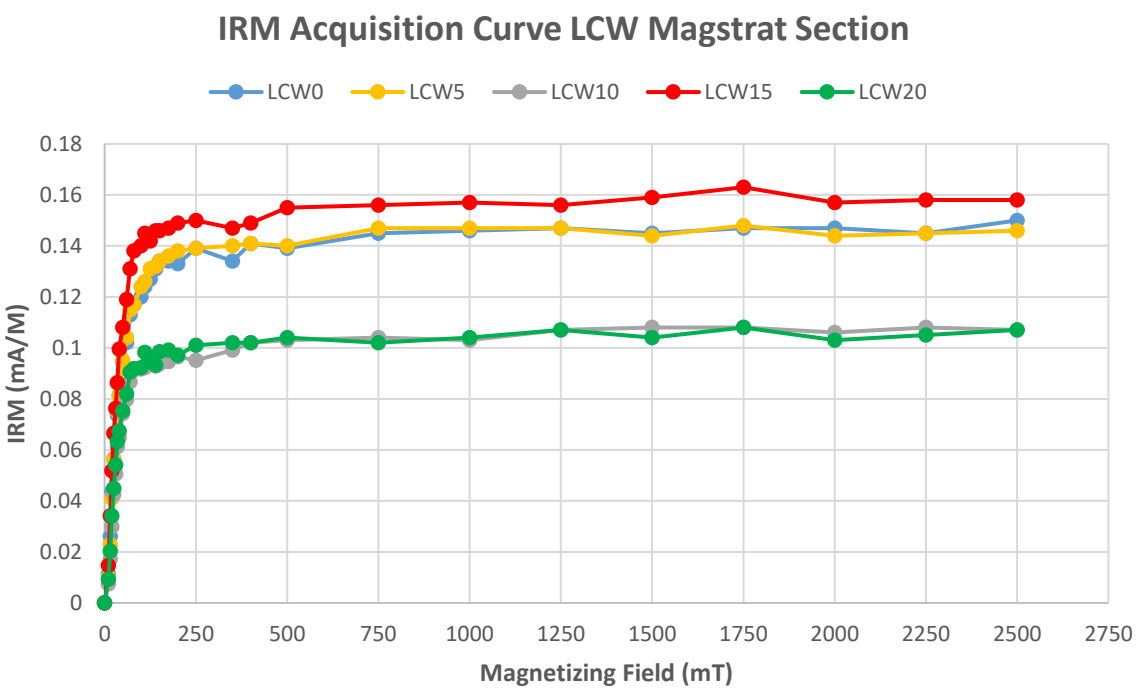

FIGURE 12: Lost Cabin Wash IRM Acquisition Curves

Isothermal Remanent Magnetization (IRM) acquisition curves for Lost Cabin Wash section samples. IRM saturation values are in milliamps/meter (mA/M), with increasing field values measured in milliTesla (mT).

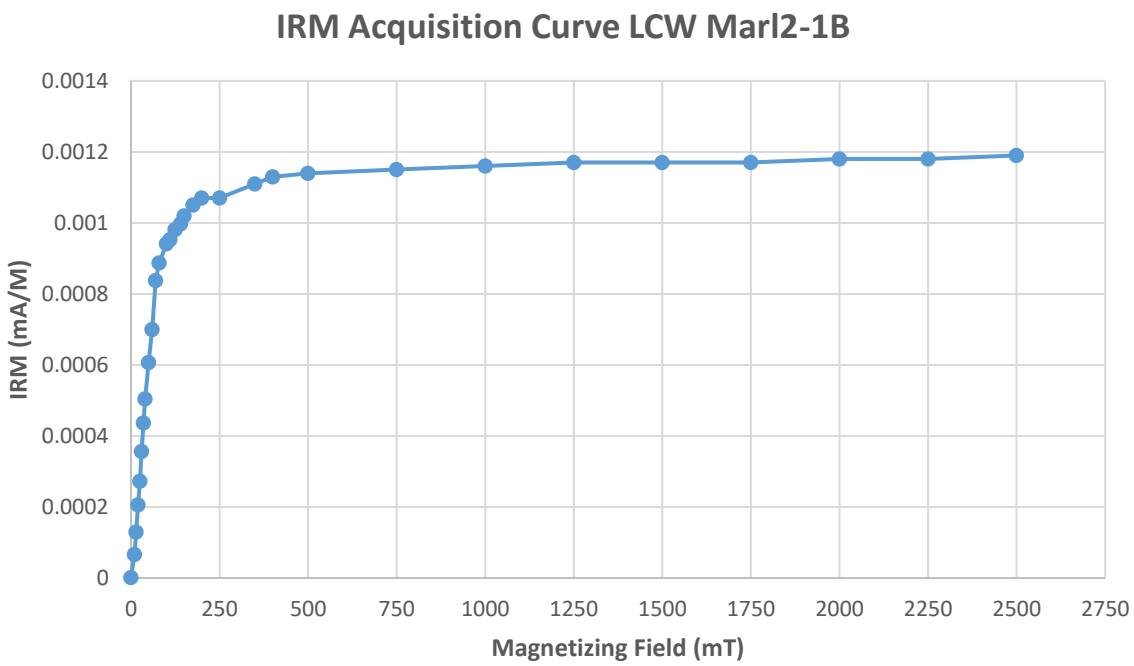

FIGURE 13: Bouse Marl IRM Acquisition Curves

Isothermal Remanent Magnetization (IRM) acquisition curve for Bouse Marl sample M2-1B. IRM saturation values are in milliamps/meter (mA/M), with increasing field values measured in milliTesla (mT).

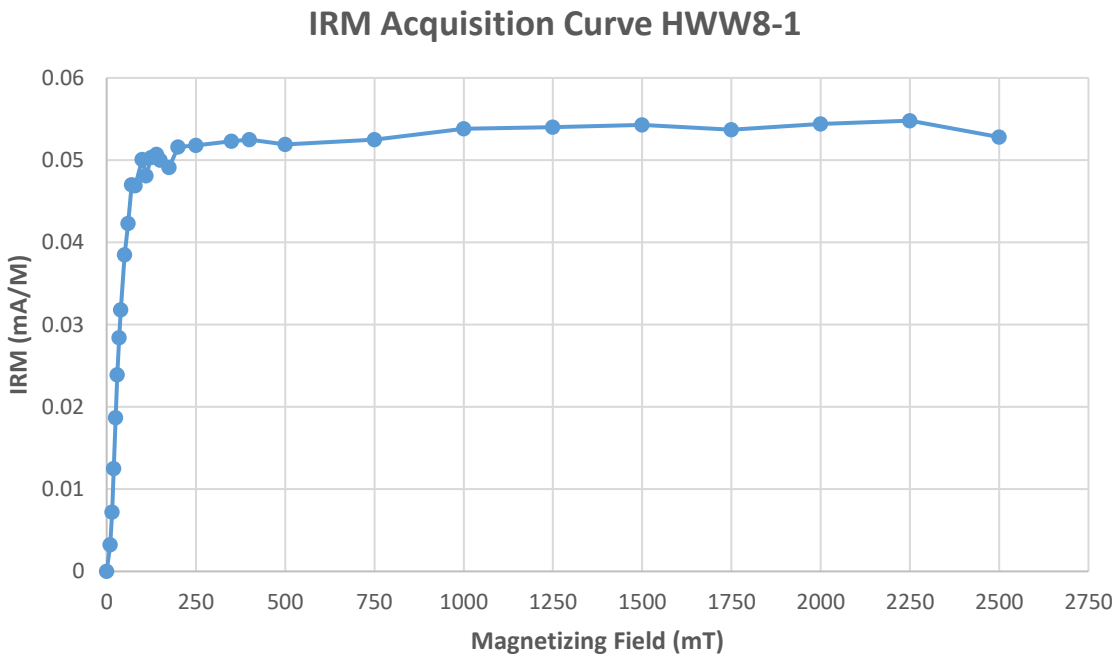

FIGURE 14: High Wall Wash IRM Acquisition Curves

Isothermal Remanent Magnetization (IRM) acquisition curve for High Wall Wash ash sample HWW8-1. IRM saturation values are in milliamps/meter (mA/M), with increasing field values measured in milliTesla (mT).

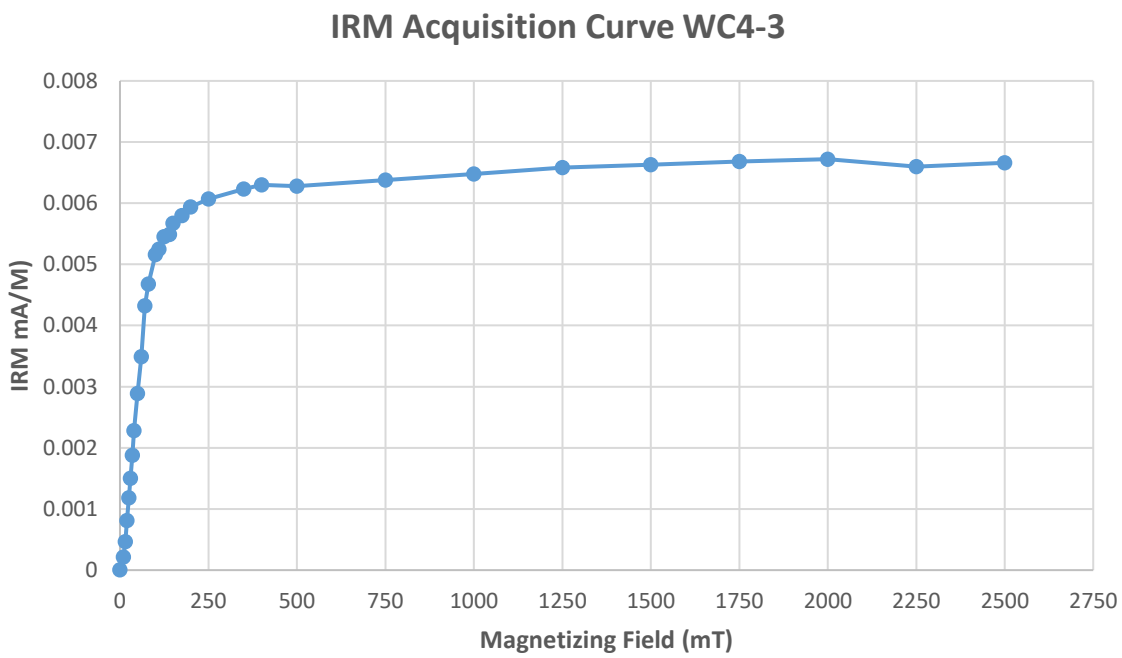

FIGURE 15: Wolverine Creek IRM Acquisition Curves

Isothermal Remanent Magnetization (IRM) acquisition curve for Wolverine Creek ash sample WC4-3. IRM saturation values are in milliamps/meter (mA/M), with increasing field values measured in milliTesla (mT).

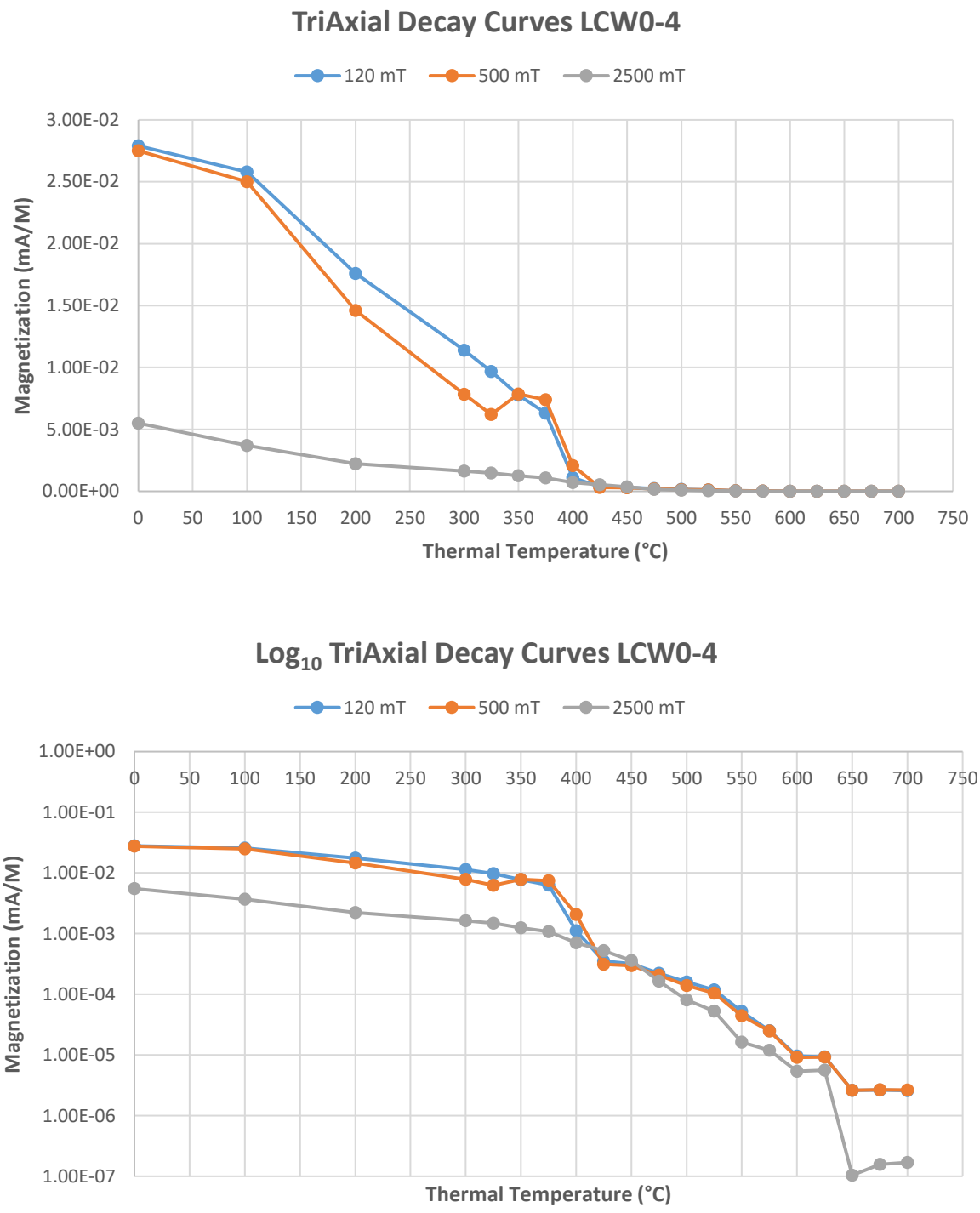

FIGURE 16: Lost Cabin Wash 0-4 Triaxial Decay Diagrams
Triaxial Lowrie (1990) plot of Lost Cabin Wash sample LCW0-4. Magnetic components are divided into soft (120 mT), medium (500 mT), and hard (2500 mT) coercivity spectra. Total sample magnetization is measured in milliamps/meter (mA/M) and is plotted against increasing temperature step measured in degrees Celsius (C°). Lowrie plot is plotted by standard conventions (top) and logarithmic (bottom) to aid in interpretation of components.

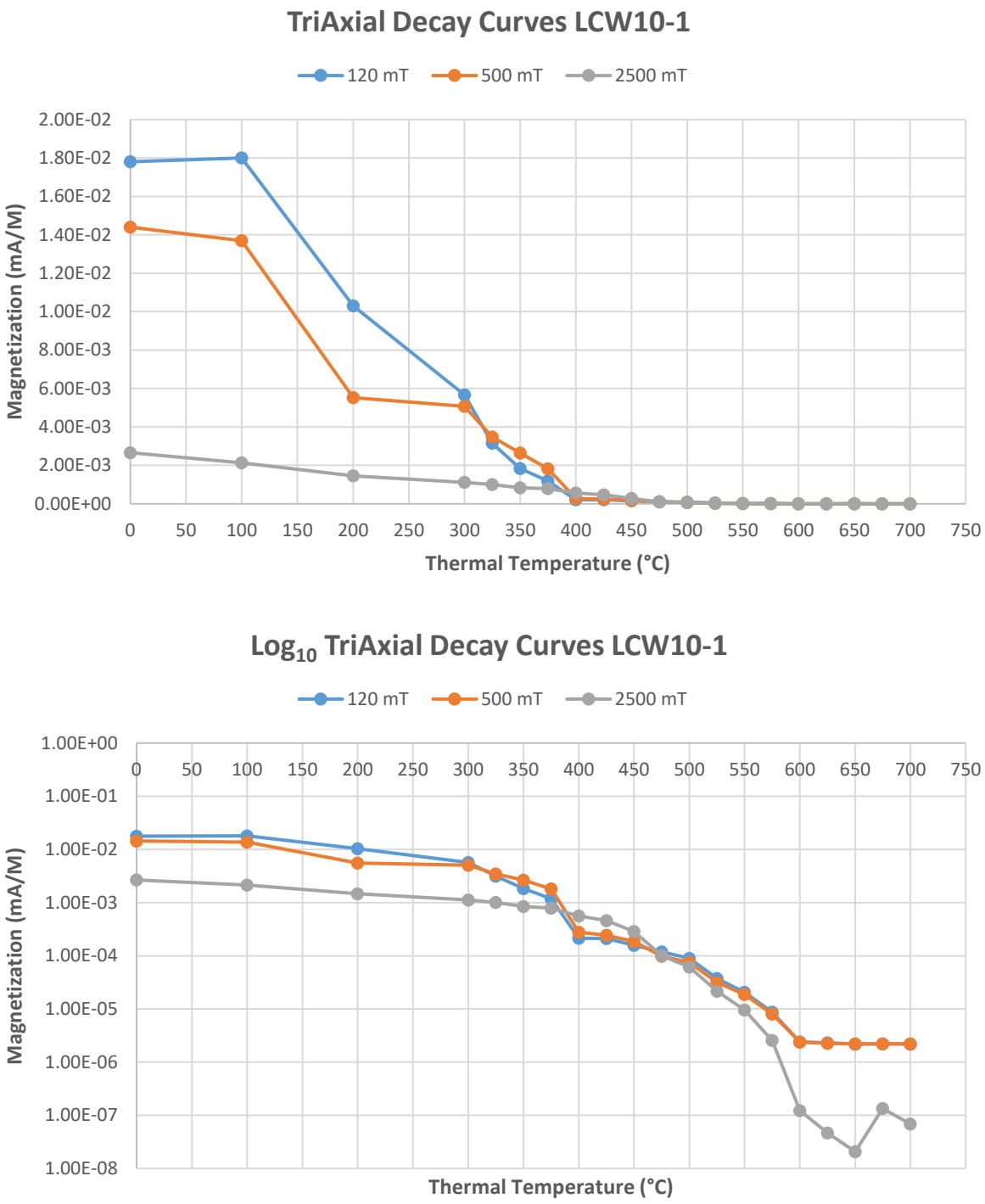

FIGURE 17: Lost Cabin Wash 10-1 Triaxial Decay Diagrams
Triaxial Lowrie (1990) plot of Lost Cabin Wash sample LCW10-1. Magnetic components are divided into soft (120 mT), medium (500 mT), and hard (2500 mT) coercivity spectra. Total sample magnetization is measured in milliamps/meter (mA/M) and is plotted against increasing temperature step measured in degrees Celsius (C°). Lowrie plot is plotted by standard conventions (top) and logarithmic (bottom) to aid in interpretation of components.

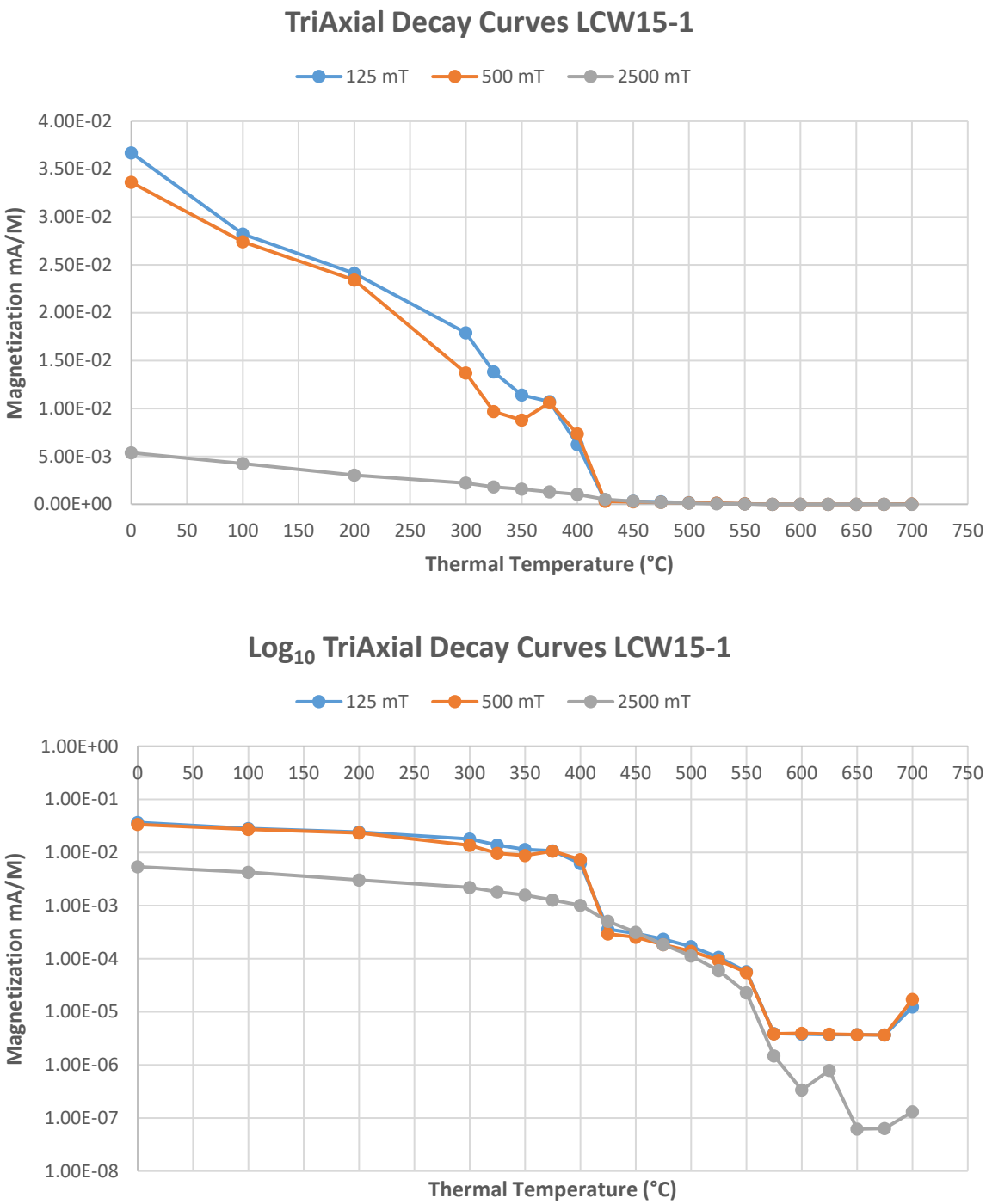

FIGURE 18: Lost Cabin Wash 15-1 Triaxial Decay Diagrams
Triaxial Lowrie (1990) plot of Lost Cabin Wash sample LCW15-1. Magnetic components are divided into soft (120 mT), medium (500 mT), and hard (2500 mT) coercivity spectra. Total sample magnetization is measured in milliamps/meter (mA/M) and is plotted with against increasing temperature step measured in degrees Celsius (C°). Lowrie plot is plotted by standard conventions (top) and logarithmic (bottom) to aid in interpretation of components.

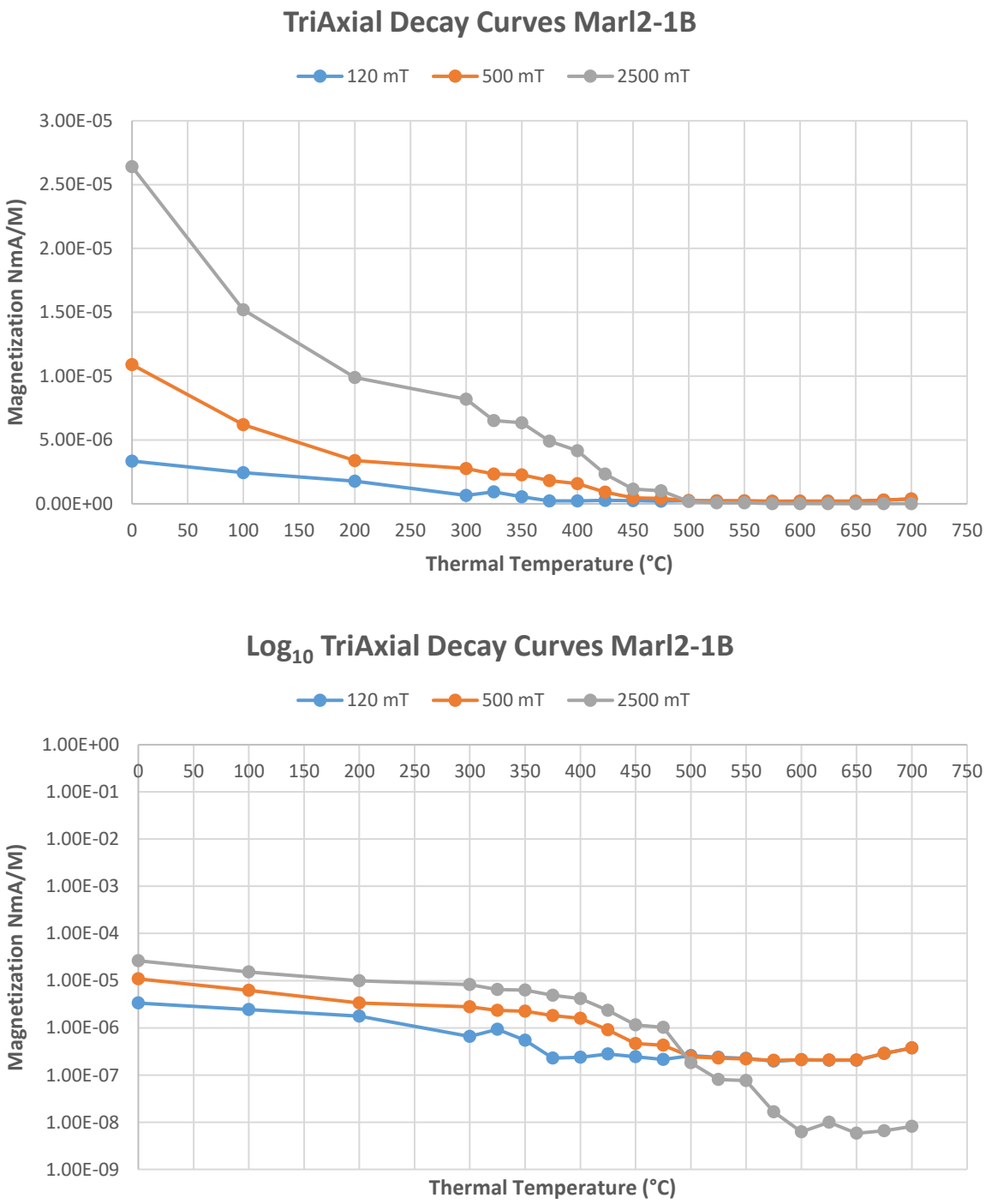

FIGURE 19: Bouse Marl 2-1B Triaxial Decay Diagrams
Triaxial Lowrie (1990) plot of Bouse Marl sample Marl2-1B. Magnetic components are divided into soft (120 mT), medium (500 mT), and hard (2500 mT) coercivity spectra. Total sample magnetization is measured in milliamps/meter (mA/M) and is plotted against increasing temperature step measured in degrees Celsius (C°). Lowrie plot is plotted by standard conventions (top) and logarithmic (bottom) to aid in interpretation of components.

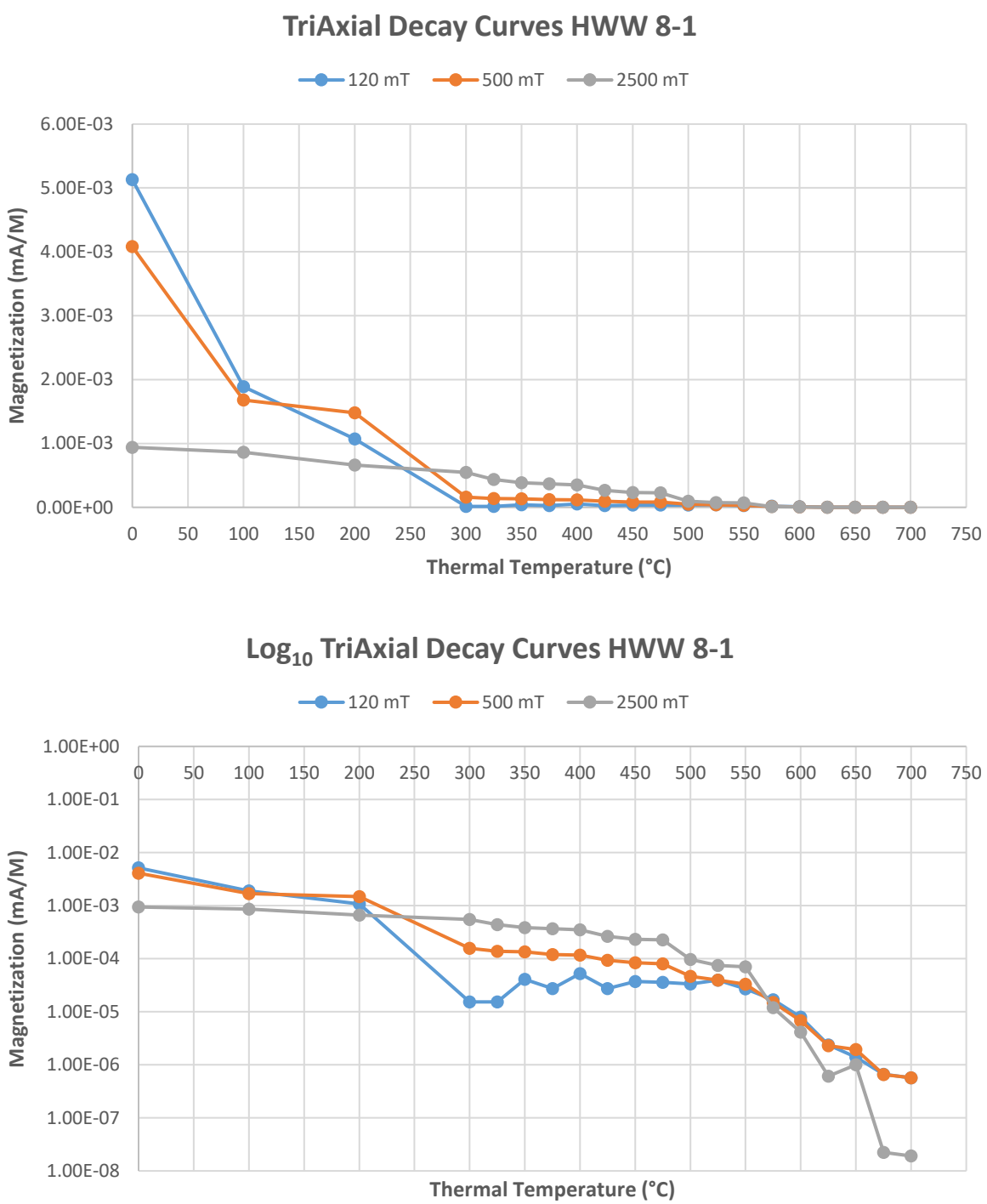

FIGURE 20: High Wall Wash 8-1 Triaxial Decay Diagrams

Triaxial Lowrie (1990) plot of High Wall Wash sample HWW8-1. Magnetic components are divided into soft (120 mT), medium (500 mT), and hard (2500 mT) coercivity spectra. Total sample magnetization is measured in milliamps/meter (mA/M) and is plotted against increasing temperature step measured in degrees Celsius (C°). Lowrie plot is plotted by standard conventions (top) and logarithmic (bottom) to aid in interpretation of components.

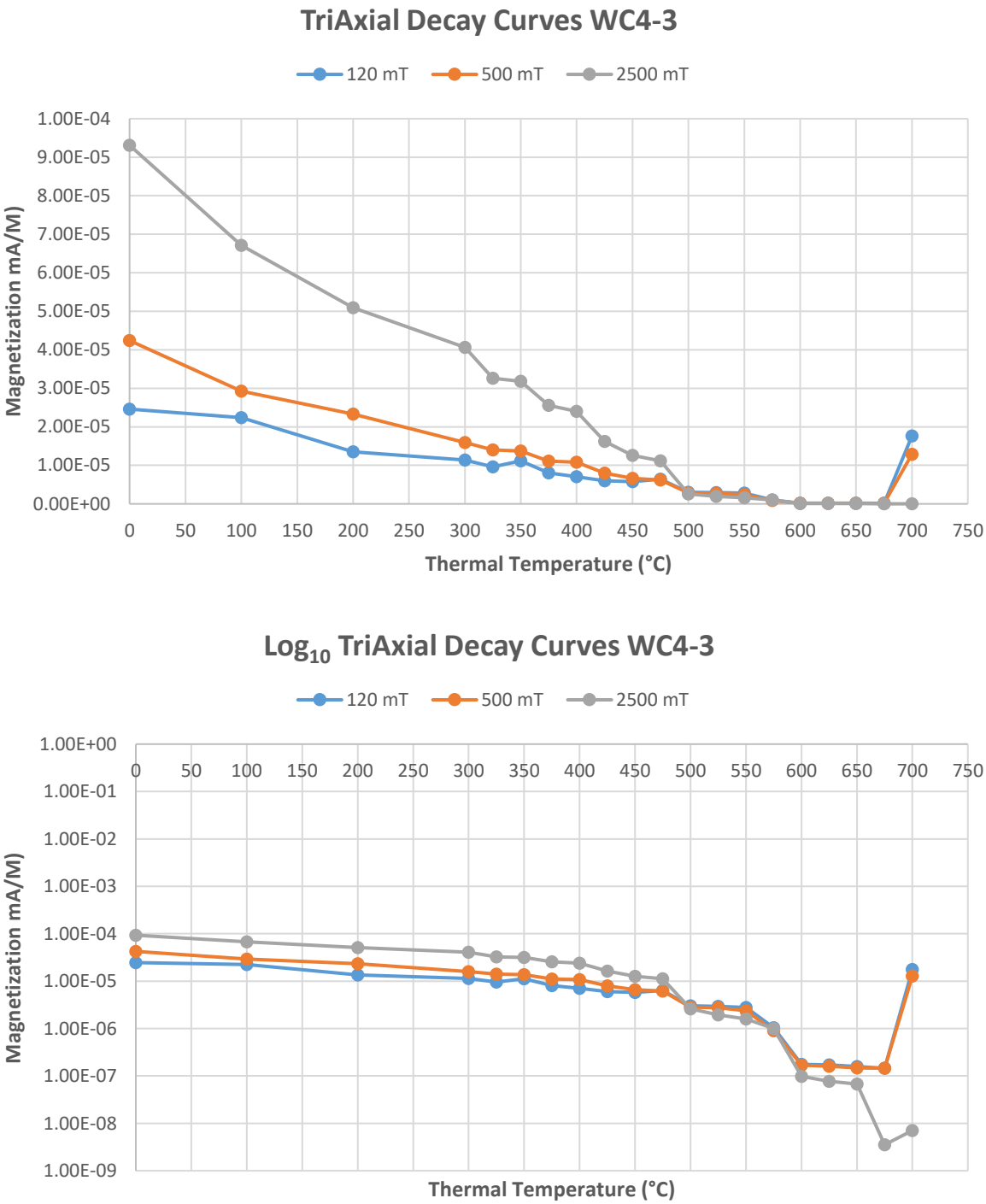

FIGURE 21: Wolverine Creek 4-3Triaxial Decay Diagrams
Triaxial Lowrie (1990) plot of Wolverine Creek sample WC4-3. Magnetic components are divided into soft (120 mT), medium (500 mT), and hard (2500 mT) coercivity spectra. Total sample magnetization is measured in milliamps/meter (mA/M) and is plotted against increasing temperature step measured in degrees Celsius (C°). Lowrie plot is plotted by standard conventions (top) and logarithmic (bottom) to aid in interpretation of components.

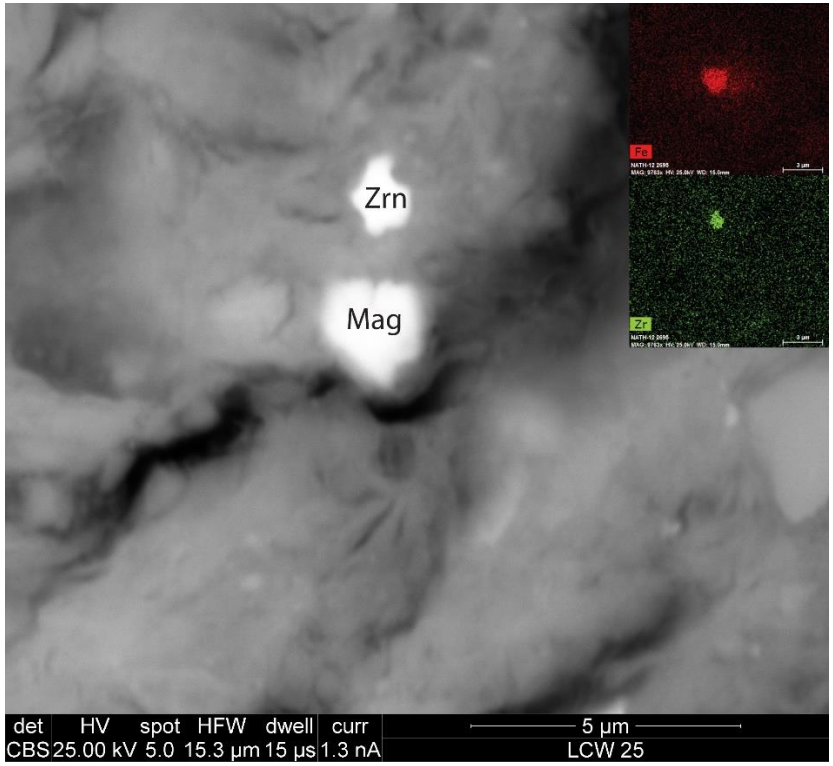

FIGURE 23: Potential Single Domain Magnetite
SEM photomicrograph showing lower range magnetite grain (~2µm) within a Lost Cabin wash thin section. The sample was close to the accepted stable Single Domain (SD) magnetite grain size of ~1µm. EDX image on top right shows concentration of Fe (magnetite) in red, and Zr (Zircon) in green.

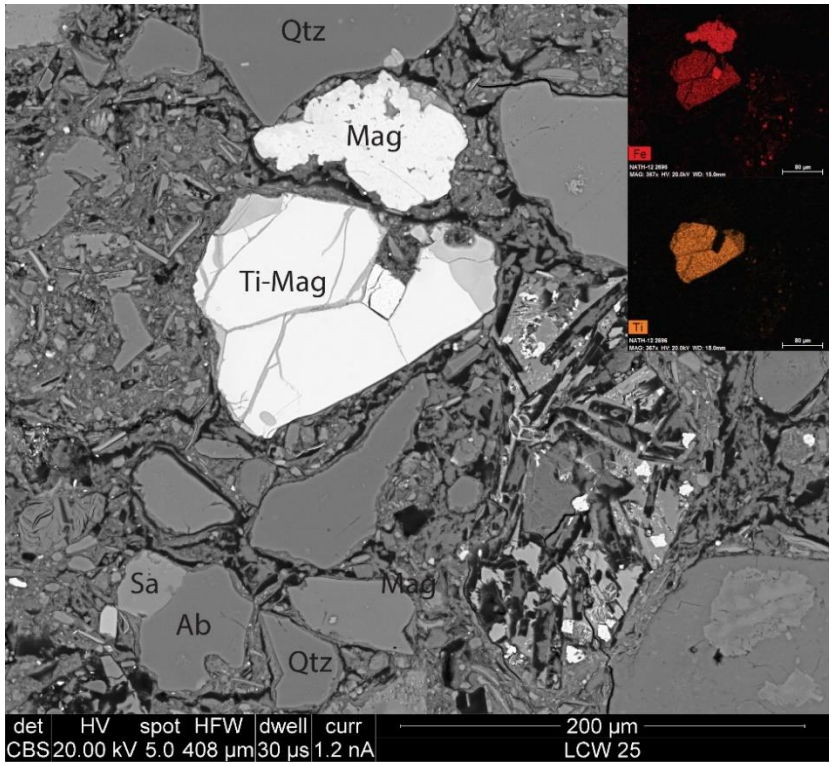

FIGURE 22: Magnetite and Titanomagnetite Grains
SEM photomicrograph showing the variable magnetic mineralogy within a Lost Cabin wash thin section sample. Note the large (~100 µm) titanomagnetite grain with exsolved ilmenite, in addition to the two grains of pure magnetite. EDX image on top right shows concentration of Fe (pure magnetite) in red, and Ti (Titanomagnetite) in orange.

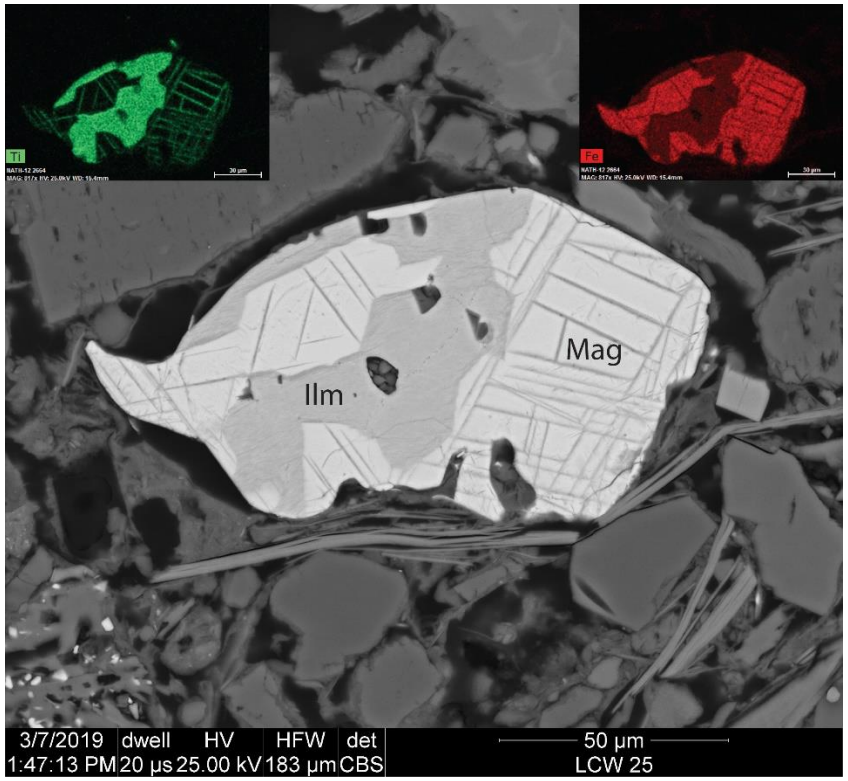

FIGURE 24: Exsolved Ilmenite and Magnetite Grain
SEM photomicrograph illustrating a large (>150 µm) titanomagnetite grain from the Lost Cabin bed magstrat section that shows extensive exsolution between endmember Ilmenite and Magnetite. EDX image on top right/left shows concentration of Fe (pure magnetite) in red, and Ti (Ilmenite) in green, respectively.

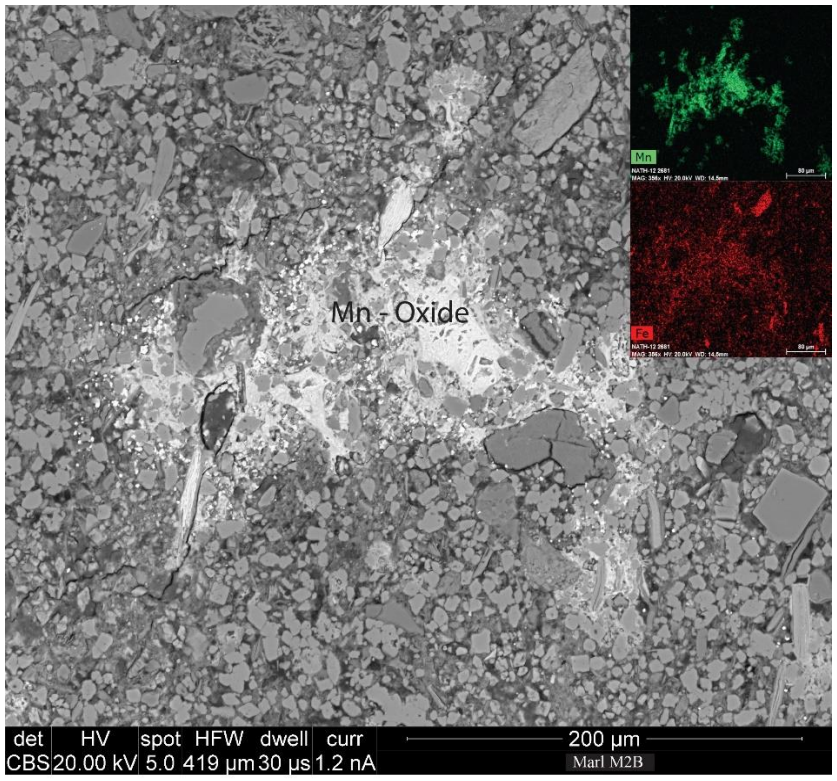

FIGURE 25: Secondary Manganese Oxide
SEM photomicrograph of Bouse Marl sample showing an example of secondary manganese oxides. While not a carrier of magnetic remenance, this oxide illustrates the extent of secondary diagenetic alteration within the marls from meteoric fluids. EDX image on top right shows concentration of Fe in red, and Mn in green.

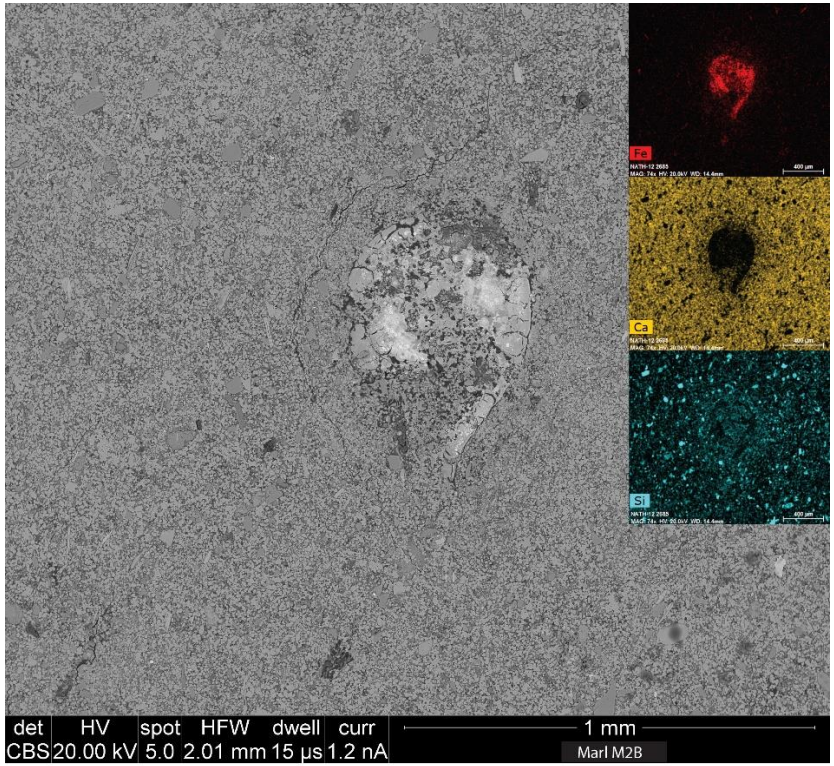

FIGURE 27: Bouse Marl Pore Mineralization
SEM photomicrograph of a Bouse Marl sample showing an example of a ~0.5 mm altered pore zone. EDX image on top right shows concentration of Fe (Magnetite/Fe-clays) in red, Ca (Calcite) in yellow, and Si (Quartz/Feldspars) in blue. EDX reveals a concentration of interpreted secondary iron within the altered pore.

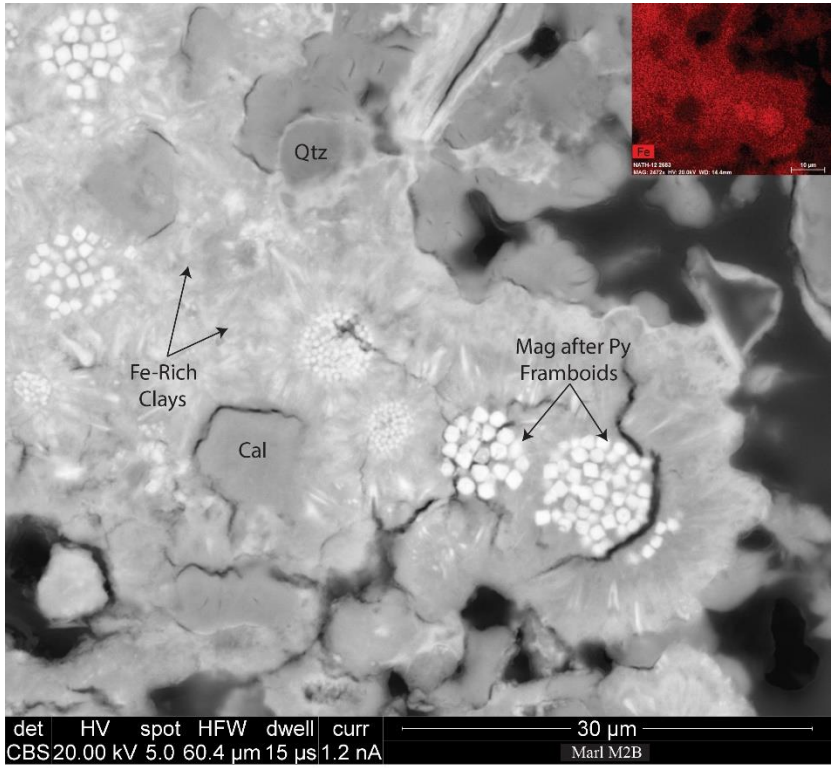

FIGURE 26: Magnetite after Pyrite Framboids
SEM photomicrograph of the altered pore space from (Fig. 26). The Fe-rich zone was predominantly filled with rounded concentrations of framboids and surrounded by radiating textures of Fe-rich clays. EDX image on top right shows concentration of Fe within framboids, with no sign of sulfur. This points to a possible diagenetic alteration of authigenic pyrite to magnetite.

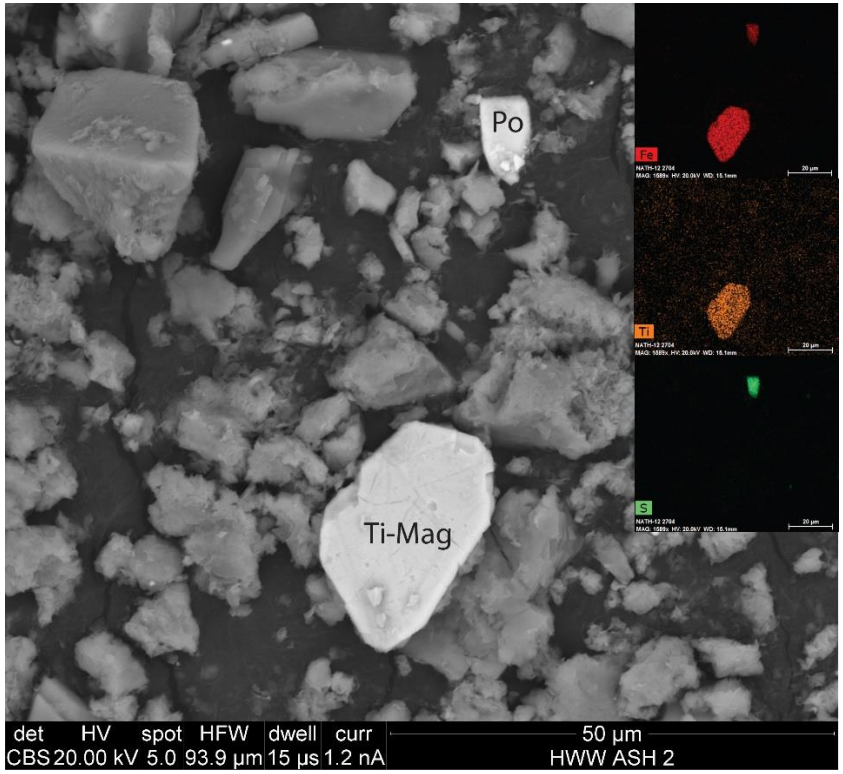

FIGURE 29: Pyrrhotite and Titanomagnetite Grains
SEM photomicrograph of High Wall Wash detrital sample illustrating the predominate magnetic carriers within the samples. EDX image on top right shows concentration of Fe in red, Ti (Titanomagnetite) in orange, and S (pyrrhotite).

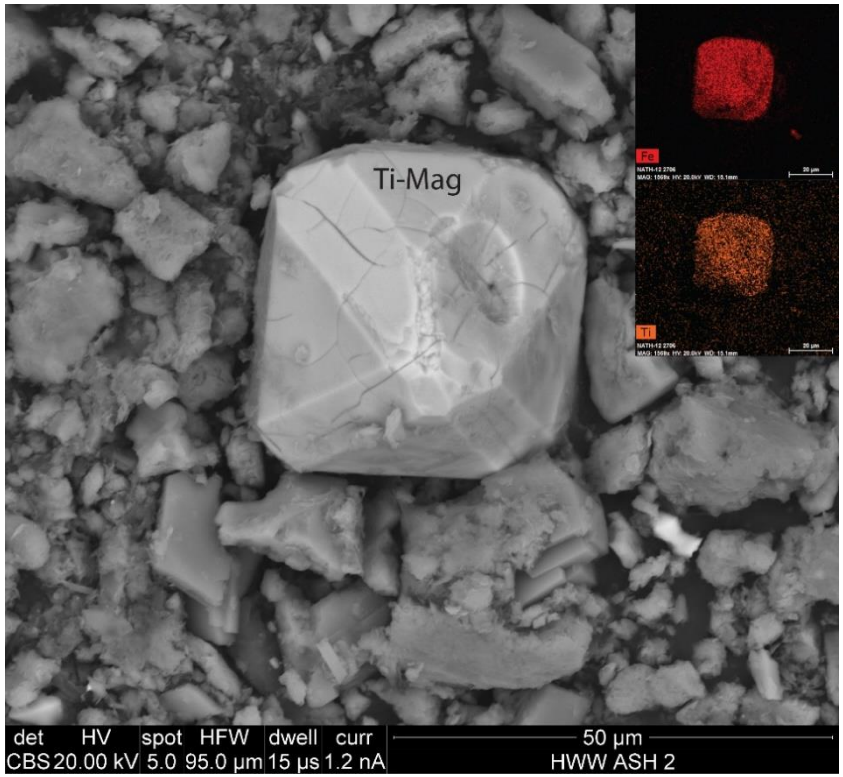

FIGURE 28: Euhedral Titanomagnetite Grain
SEM photomicrograph of High Wall Wash detrital sample showing a large (~25µm) primary euhedral Titanomagnetite grain. EDX image on top right shows concentration of Fe in red, and Ti in orange.

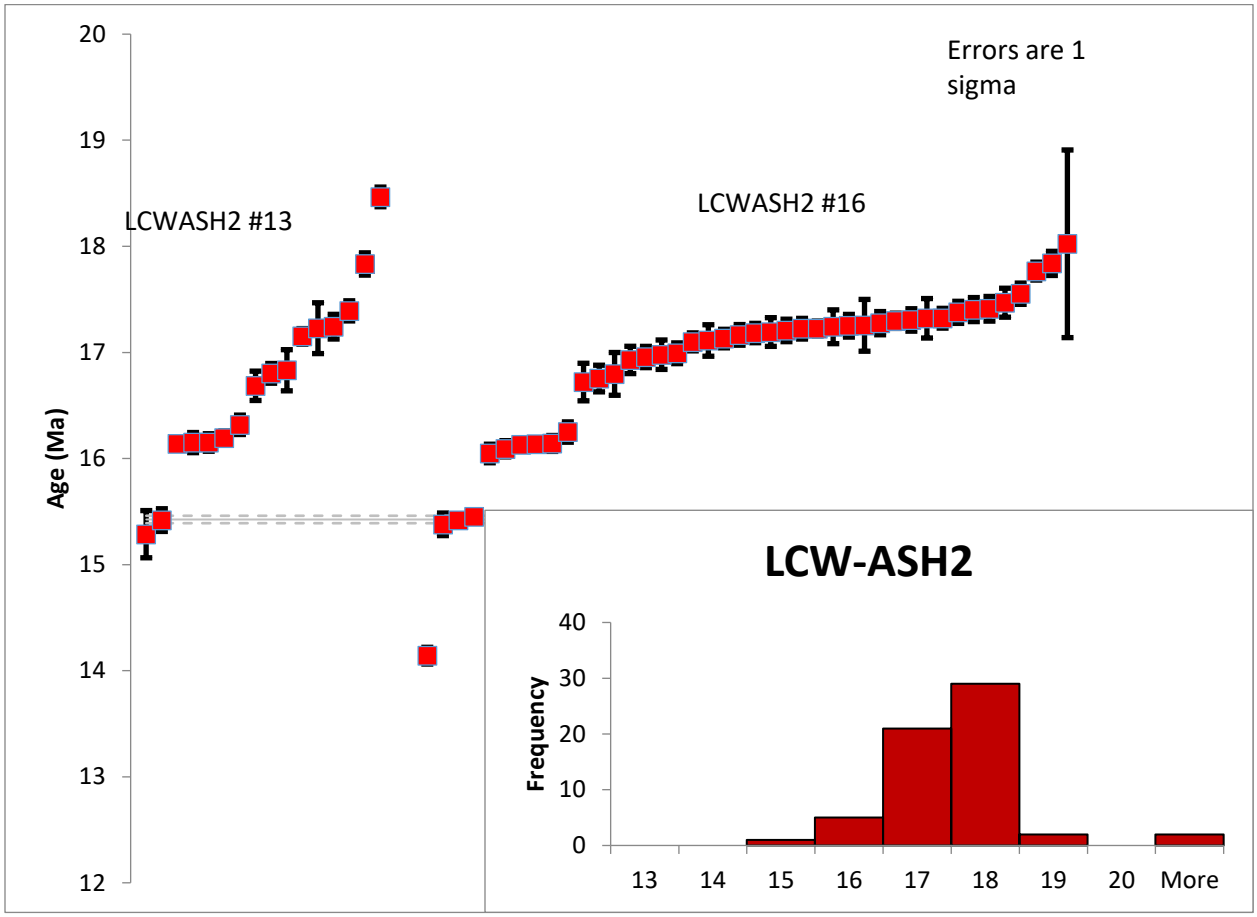

FIGURE 30: LCW-ASH2 Single-Grain $^{40}Ar/^{39}Ar$ Ages

$^{40}Ar/^{39}Ar$ ages from single-grain sanidine analysis of Lost Cabin bed ash sample LCW-ASH2. All samples show associated errors bars at 1 sigma resolution. Histogram shows relative frequency of single grain ages from total sample population.

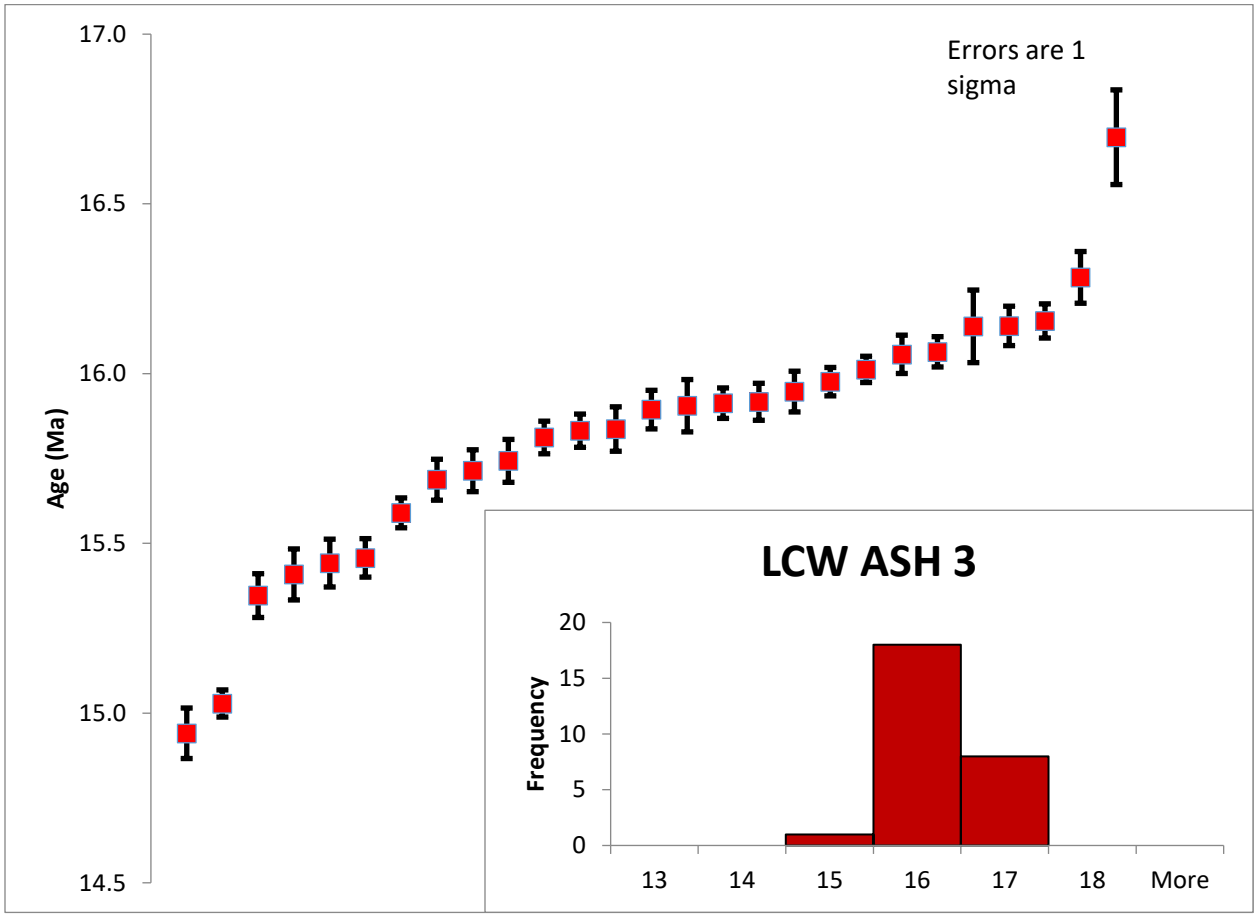

FIGURE 31: LCW-ASH3 Single-Grain $^{40}Ar/^{39}Ar$ Ages

$^{40}Ar/^{39}Ar$ ages from single-grain sanidine analysis of Lost Cabin bed ash sample LCW-ASH3. All samples show associated errors bars at 1 sigma resolution. Histogram shows relative frequency of single grain ages from total sample population.

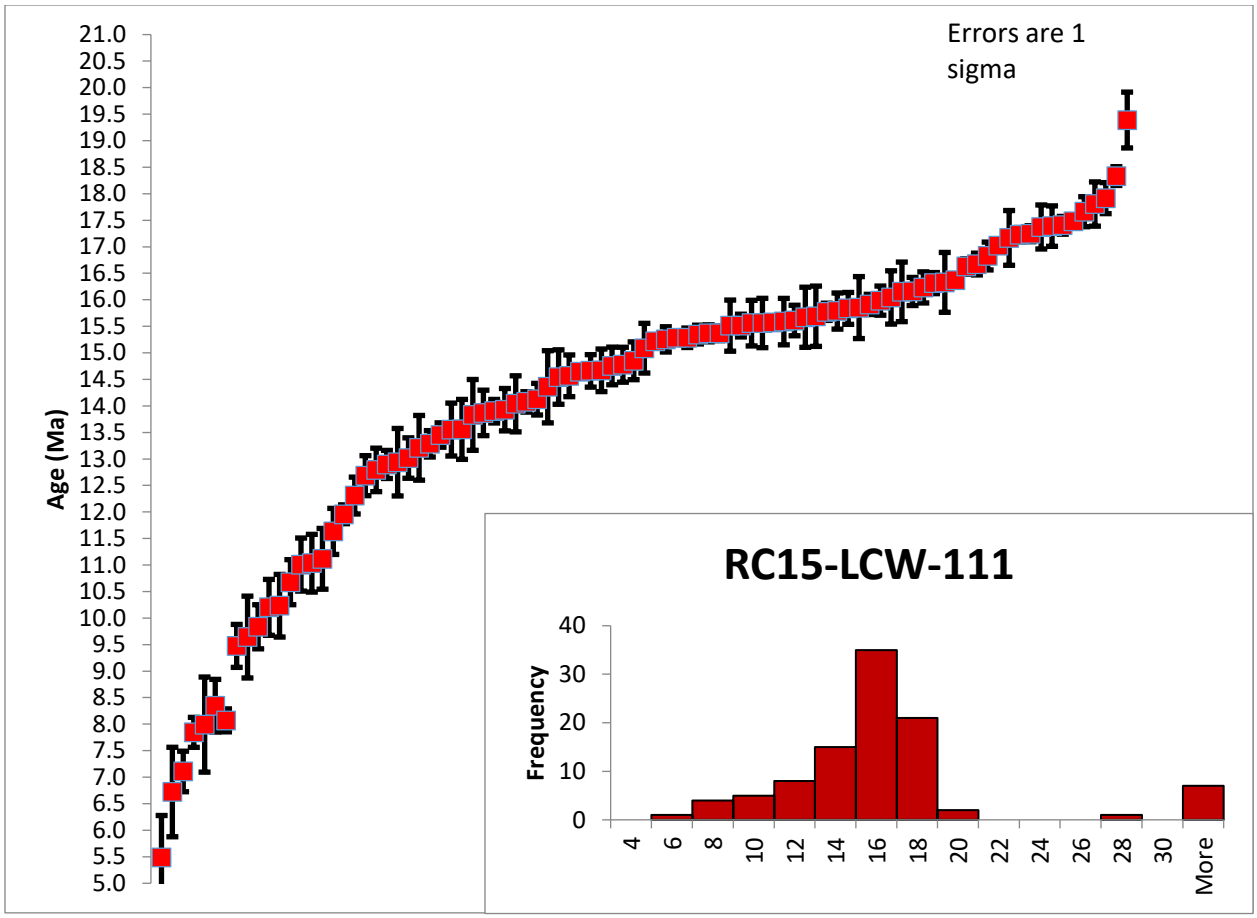

FIGURE 32: RC15-LCW-111 Single-Grain $^{40}Ar/^{39}Ar$ Ages

$^{40}Ar/^{39}Ar$ ages from single-grain sanidine analysis of Lost Cabin bed ash sample RC15-LCW-111. All samples show associated errors bars at 1 sigma resolution. Histogram shows relative frequency of single grain ages from total sample population.

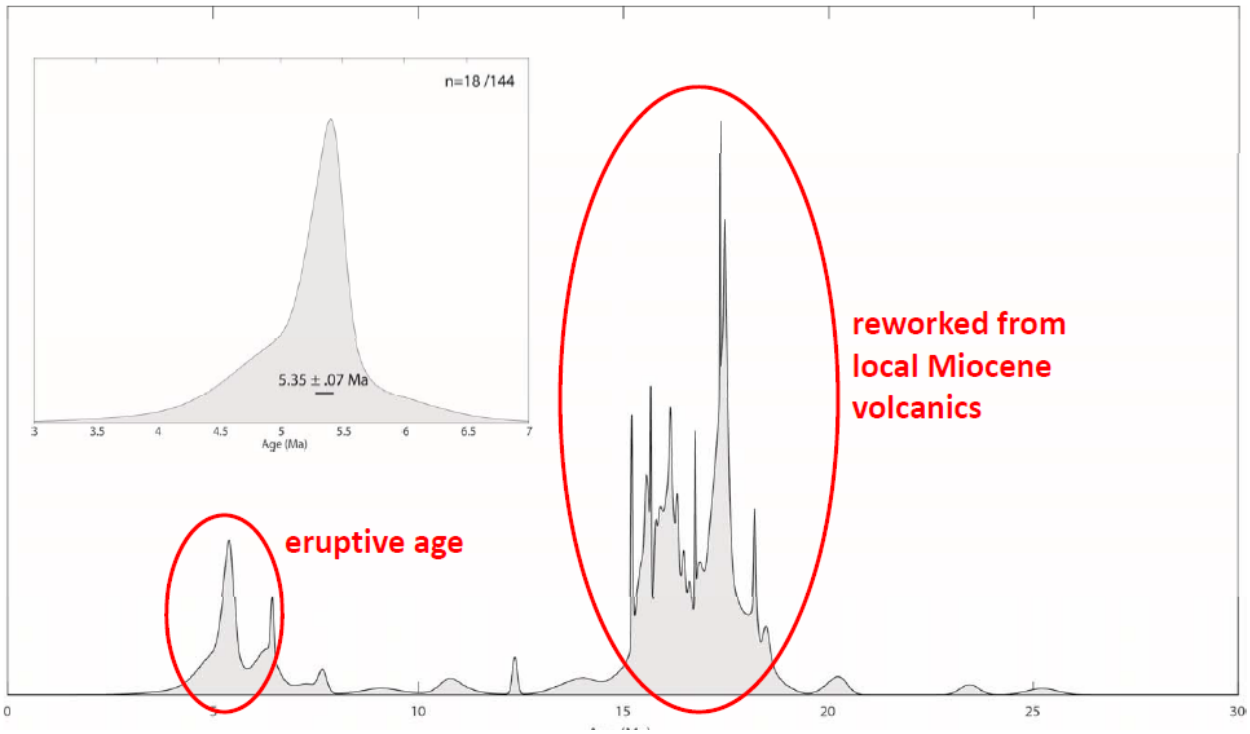

FIGURE 33: High Wall Wash $^{40}Ar/^{39}Ar$ Age Distribution
Histogram showing relative frequency of single-grain sanidine $^{40}Ar/^{39}Ar$ ages from High Wall Wash ash site. ~15 – 18 Ma distribution interpreted as being reworked from local Miocene volcanism, while younger 5.35 ± 0.7 population (18/144 grains) interpreted as a younger late Miocene ash fall event. Figure from Ryan Crow (personal correspondence, 2018).

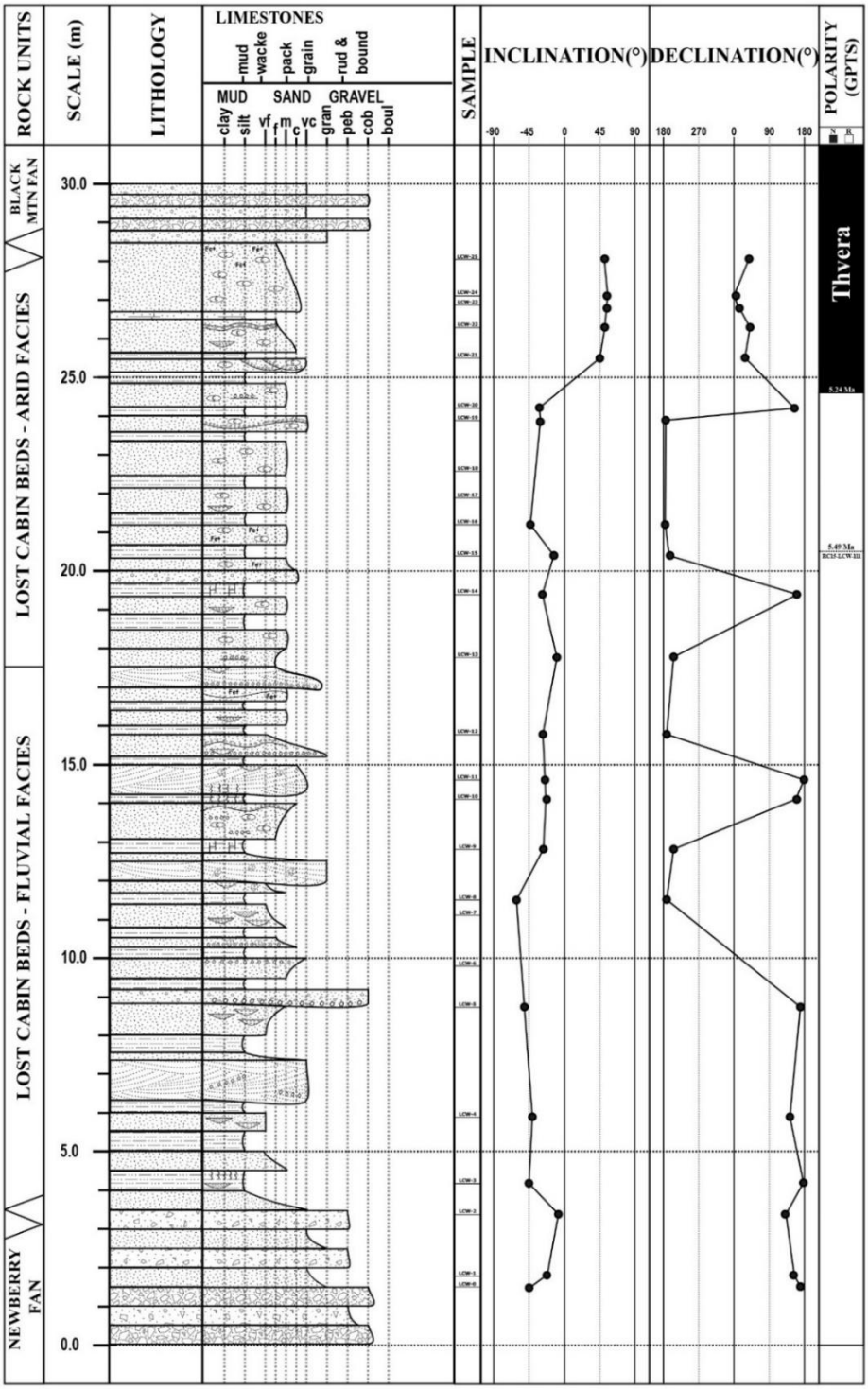

FIGURE 34: Lost Cabin Wash Stratigraphy with Sample Site Polarity

Stratigraphic compilation of Lost Cabin bed section. All sample sites are labeled from bottom to top and are tied to plotted declination and inclination values. Rock unit descriptions illustrate the gradation of Newberry Mtn fanglomerate to the coarse-grain fluvial facies of Lost Cabin beds, before shifting to the fine-grained paleosol/carbonate nodule arid facies of upper section.

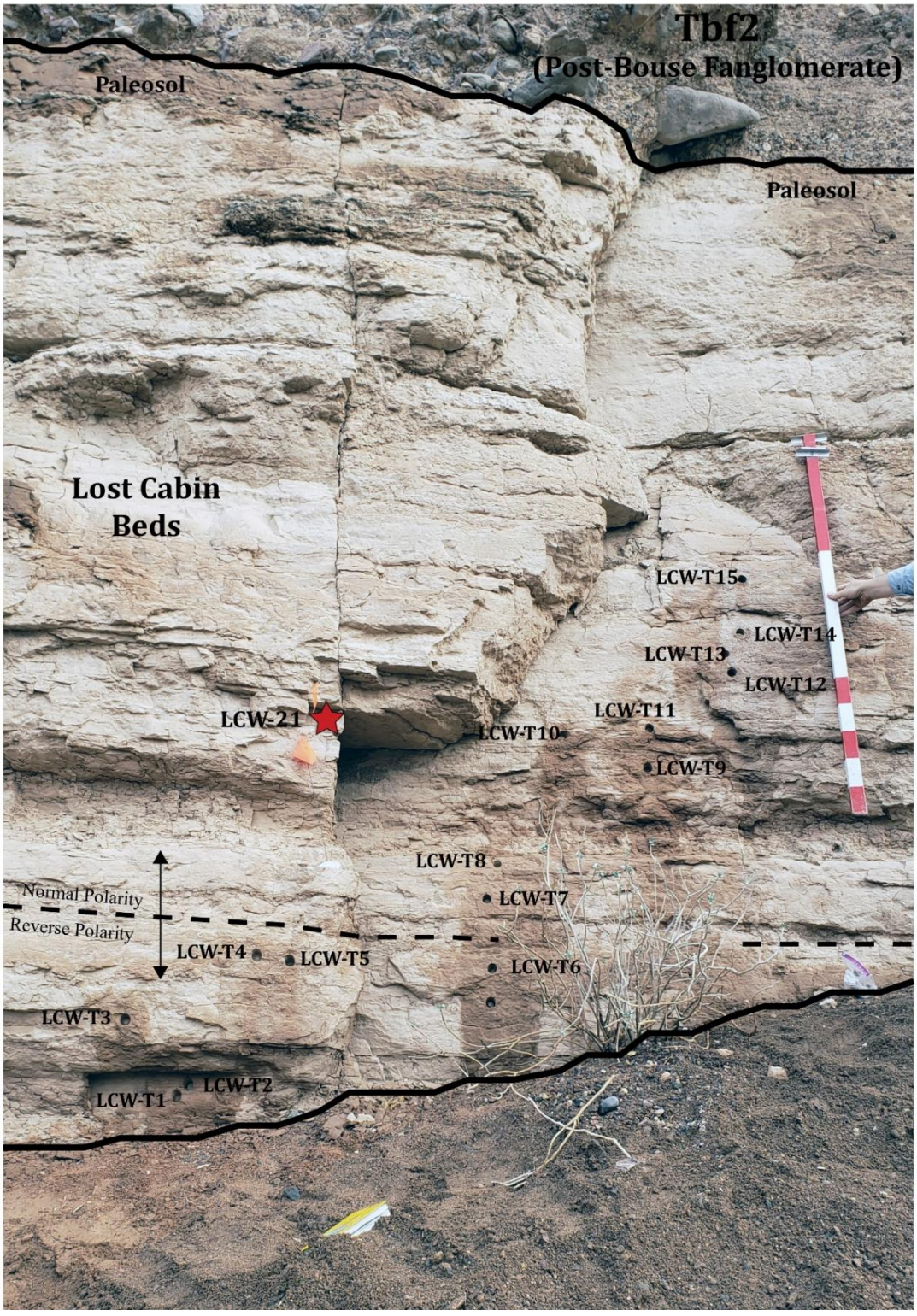

FIGURE 35: Lost Cabin Wash Reversal Site
Sample site localities of the Lost Cabin Wash section's transition/reversal site. Dashed line shows reversal elevation with normal polarity above and reverse polarity below.

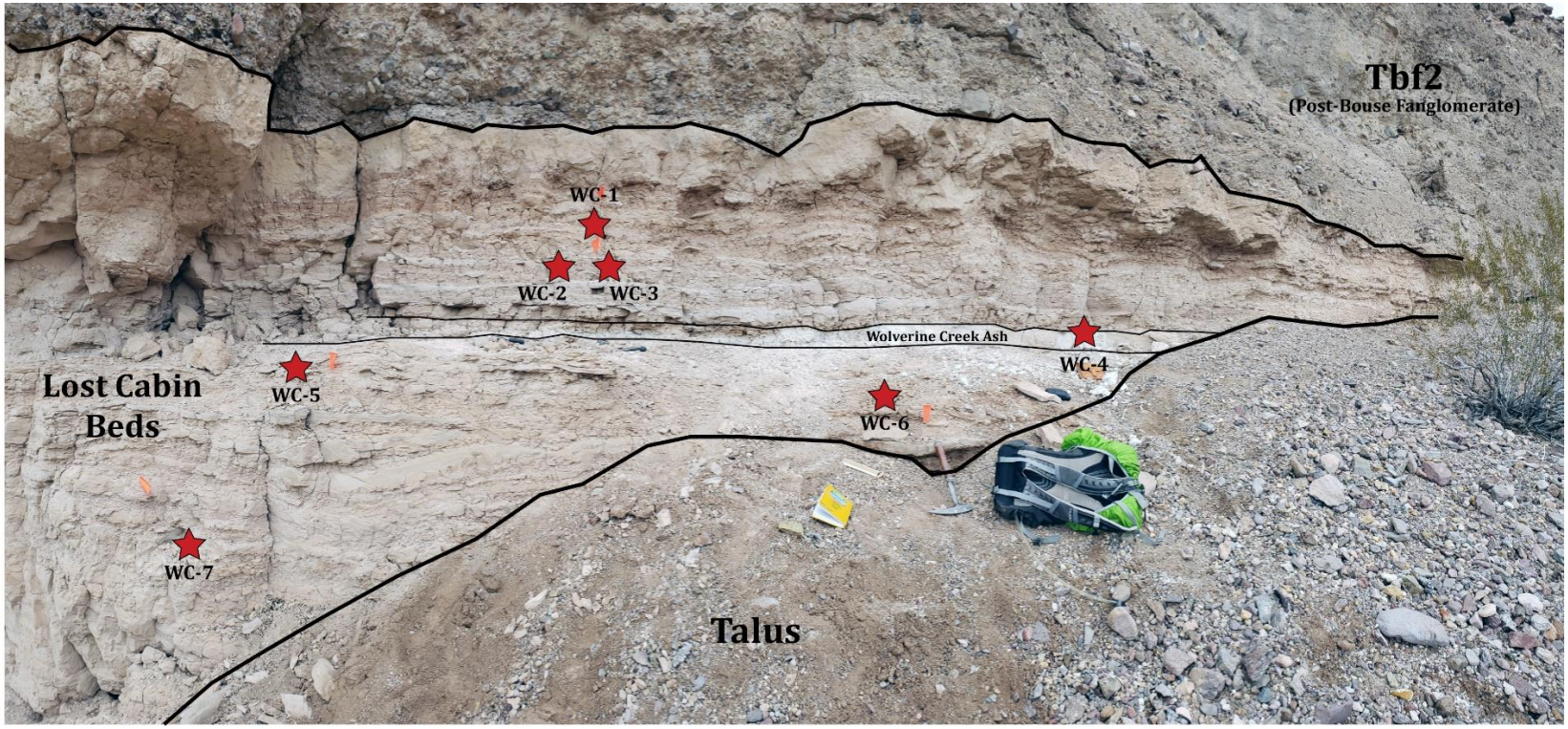

FIGURE 36: Wolverine Creek Ash Site

Sample site localities of the Wolverine Creek ash site. The ash bed was previously dated via tephrochronology with an age of 5.59 ± 0.05 Ma (House et al., 2008), which would lie within the C3r reverse polarity subchron of the Gilbert Chron. All seven sample sites yielded reverse polarity above and below the Wolverine Creek ash bed.

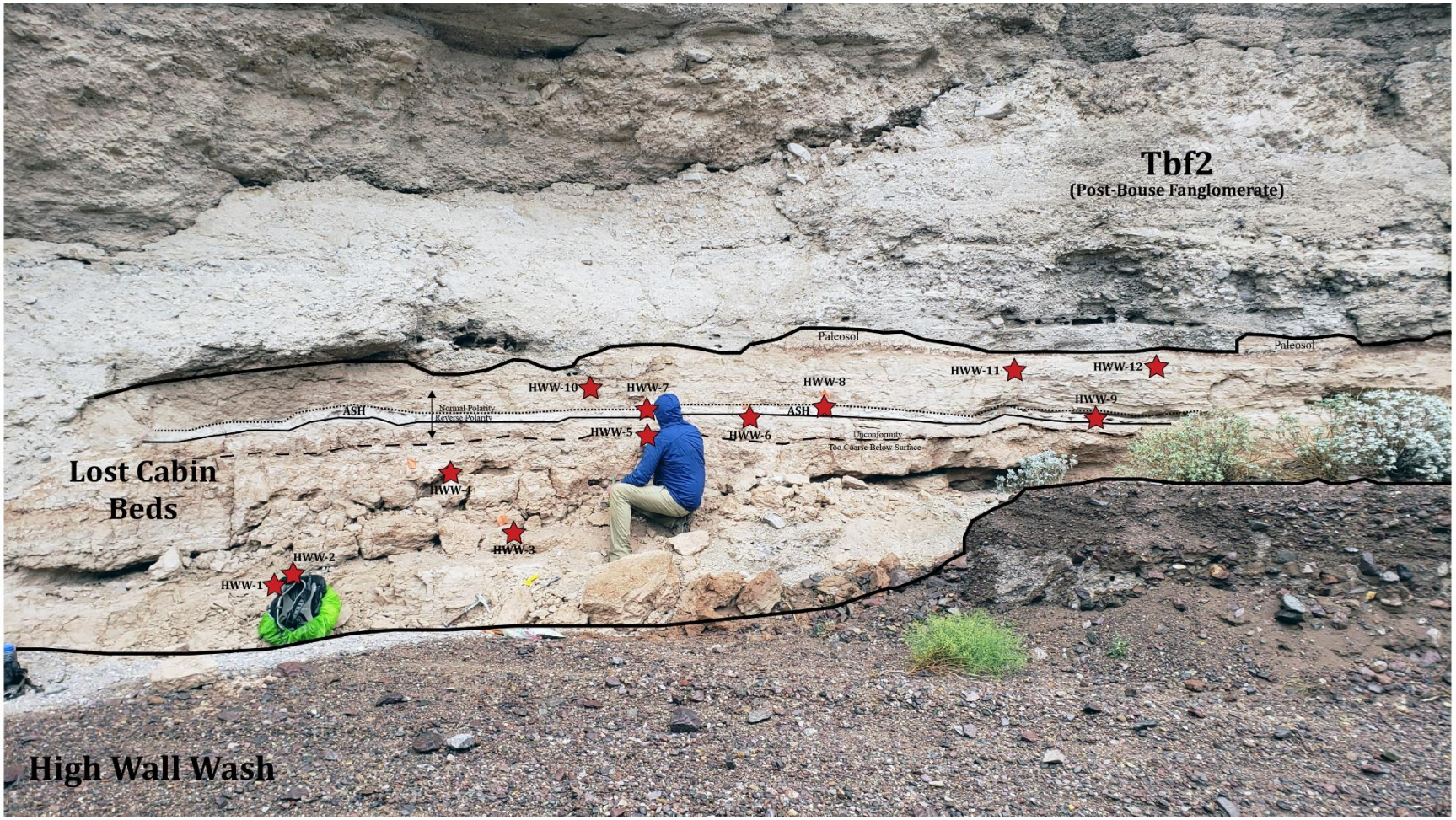

FIGURE 37: High Wall Wash Ash Site

Sample site localities of the Wolverine Creek ash site. The ash bed was previously dated via $^{40}Ar/^{39}Ar$ single-grain sanidine analysis with an age of 5.35 ± 0.7 Ma. This site yielded complex results, in which AF demagnetization proved to be the best method to unblock directions from the primary magnetic DRM carriers, pyrrhotite and titanomagnetite. Dashed line shows interpreted reversal site which lies directly above the ash bed in sample HWW-7. It is interpreted that a CRM normal polarity chemical overprint exists in hematite which resulted from sediment exposure as evident by the paleosol observed above the site.

FIGURE 38: Golden Section Site

Sample site localities of the Golden Section site. This site is unique in being the only location within the CV that shows the stratigraphic relationship in which Lost Cabin beds are found directly below Bouse Marl deposits. A total of five sample from 2 sites yielded a reverse polarity. The Lost Cabin beds in this locality are 30 m above reverse polarity Lost Cabin bed sediments in LCW and contain no facies indicators of arid climate such as carbonate nodules. The uppermost beds were found to contain thin layers of green mud, a lithologic indicator of Bouse aged fluvial sediments.

FIGURE 39: Bouse Fluvial Incision Site

Sample site localities of the Bouse fluvial incision site that was found in LCW. The site exhibits an unconformable contact with the underlying Lost Cabin beds. The base of the channel features a basal lag, that contained a detrital cobble of Bouse Marl. This relationship suggests that the incision deposits record a time of post-marl/lacustrine deposition. A total of four samples from one site have yielded a reverse polarity indicating a subchron of reverse polarity during the draining of paleo-Lake Mohave.

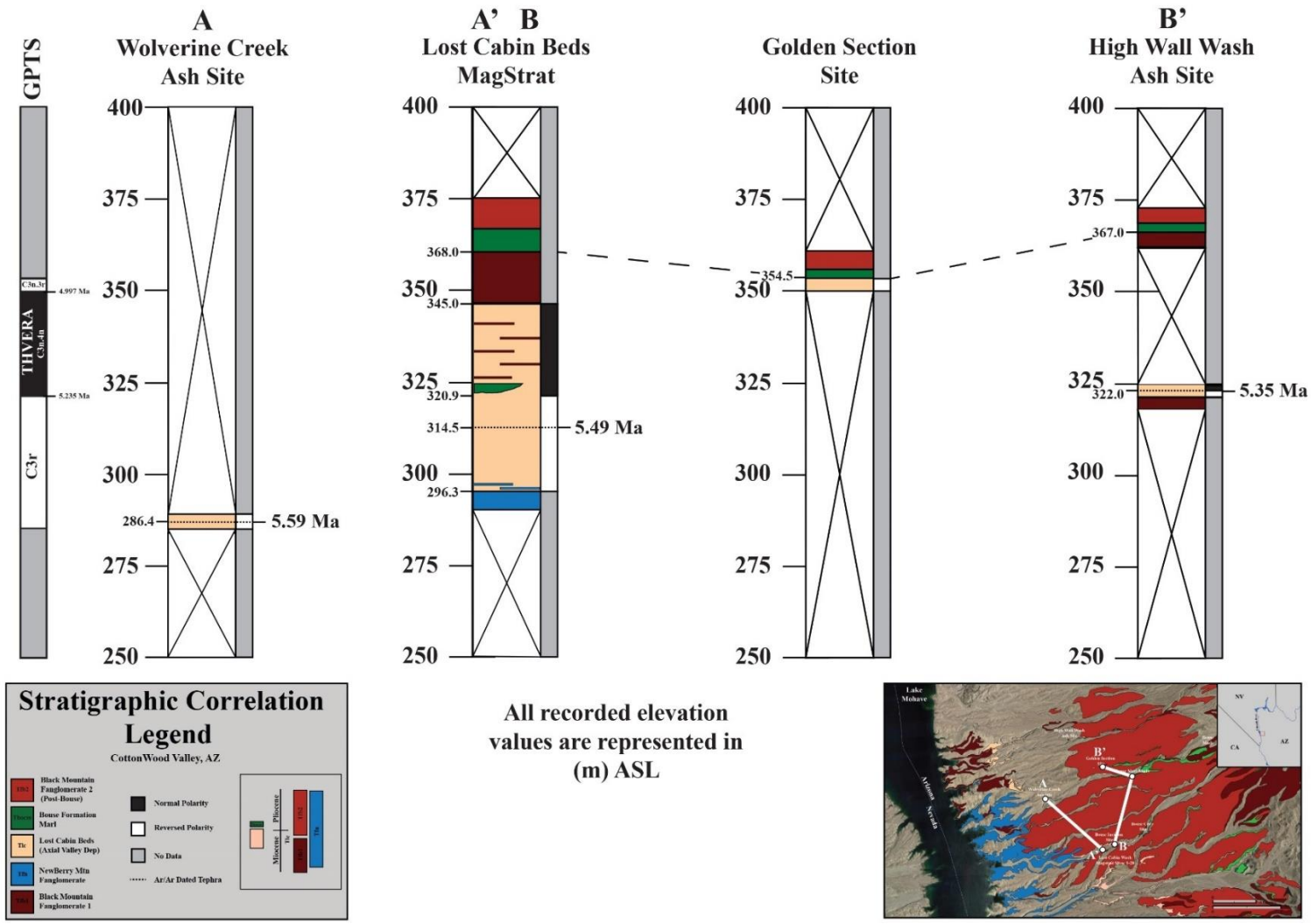

FIGURE 40: Magnetostratigraphy Correlation of Sample Sites

Stratigraphic correlation of all sample sites within the CV. All elevation data was measured via HPGPS and is presented in m above sea level. All three ash beds are labeled with dashed line and displayed with age and elevation data. Polarity reversals are indicated by magnetic polarity bars in which black represents normal polarity and white represents reverse polarity. All polarity results are tied to the Geomagnetic Polarity Timescale (GPTS) with subchron/chron data provided from Ogg (2012).

APPENDIX
UNABRIDGED LOST CABIN WASH STRATIGRAPHIC COLUMN:

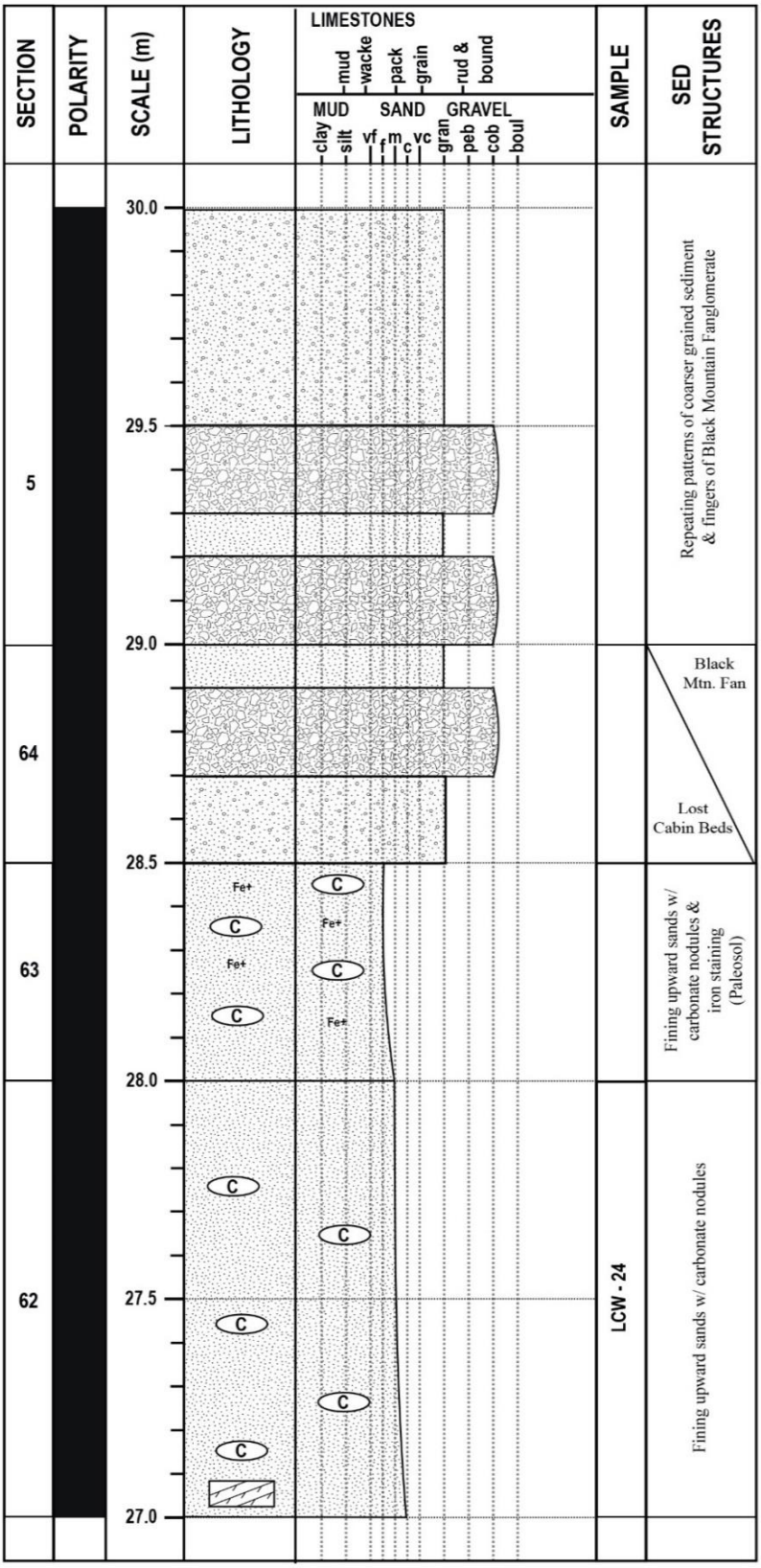

SECTION
POLARITY
SCALE (m)
LITHOLOGY
LIMESTONES
mud
wacke
pack
grain
rud & bound
MUD
SAND
GRAVEL
clay
silt
vf
f
m
c
vc
gran
peb
cob
boul
SAMPLE
SED STRUCTURES
61
60
59
58
57
56
27.0
26.5
26.0
25.5
25.0
24.5
24.0
LCW - 23
Blocky sands w/ carbonate nodules
Soil Carbonate layer
LCW - 22
Blocky & laminar bedded sands w/ coarse grained lens channels, wavy mud beds, & carbonate nodules
LCW - 21
LCW- ASH 7
Coarsening upward sands w/ minor coarse grained crossbeds & carbonate nodules
Blocky sand beds and minor silts w/ laminar sheet-like coarse layers & abundant carbonate nodules
LCW - 20
LCW- ASH 6.5
Laminar silts w/ thin stringers of ash beds

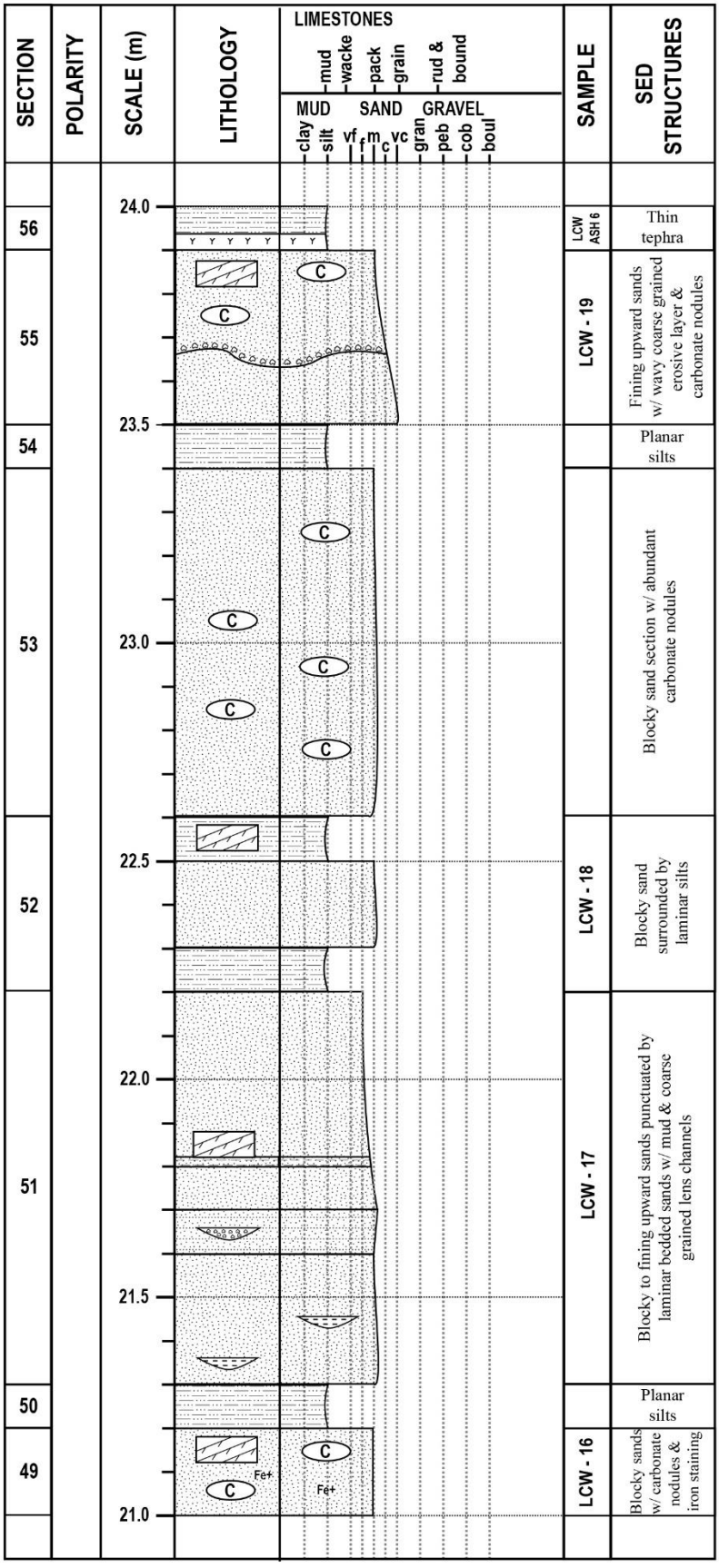
SECTION
POLARITY
SCALE (m)
LITHOLOGY
LIMESTONES
mud
wacke
pack
grain
rud &
bound
MUD
SAND
GRAVEL
clay
silt
vf
f
m
c
vc
gran
peb
cob
boul
SAMPLE
SED STRUCTURES
56
55
54
53
52
51
50
49
24.0
23.5
23.0
22.5
22.0
21.5
21.0
LCW ASH 6
Thin tephra
LCW - 19
Fining upward sands w/ wavy coarse grained erosive layer & carbonate nodules
Planar silts
Blocky sand section w/ abundant carbonate nodules
LCW - 18
Blocky sand surrounded by laminar silts
LCW - 17
Blocky to fining upward sands punctuated by laminar bedded sands w/ mud & coarse grained lens channels
Planar silts
LCW - 16
Blocky sands w/ carbonate nodules & iron staining
C
Fe+

SECTION
POLARITY
SCALE (m)
LITHOLOGY
LIMESTONES
mud
wacke
pack
grain
rud &
bound
MUD
SAND
GRAVEL
clay
silt
vf
f
m
c
vc
gran
peb
cob
boul
SAMPLE
SED STRUCTURES
49
48
47
46
45
44
43
21.0
20.5
20.0
19.5
19.0
18.5
18.0
Fe+
C
LCW - 15
CROW ASH
LCW - 14
Erosive base followed by fining upward sands w/ coarse sheet-like layers, carbonate nodules, & iron staining
Thin tephra covered by silt bed w/ mud cracks
Blocky sand w/ carbonate nodules & iron staining
Coarse sands punctuated by silt beds w/ mud cracks
Fining upward sands w/ coarse lens channels & abundant carbonate nodules near top
Planar silts
Blocky sands w/ abundant carbonate nodules

SECTION
POLARITY
SCALE (m)
LITHOLOGY
LIMESTONES
mud
wacke
pack
grain
rud &
bound
MUD
SAND
GRAVEL
clay
silt
vf
f
m
c
vc
gran
peb
cob
boul
SAMPLE
SED STRUCTURES
43
42
41
40
39
38
37
36
35
34
18.0
17.5
17.0
16.5
16.0
15.5
15.0
Fe+
Fe+
LCW - 13
Erosive crossbedded base followed by fining upward sands
Blocky sands that fine upward & are cut by muddy lens channels
Erosive base w/ corase lag followed by planar sands & crossbedded sands
Blocky sands w/ wavy diagenetic iron banding near top
Planar silts
Silts followed by blocky sands w/ coarse lens channels
LCW - 12
Erosive base w/ thick coarse basal lag, fining upwards into planar sheeted sands
Repeating silts & blocky sands w/ muddy lens channels

SECTION
POLARITY
SCALE (m)
LITHOLOGY
LIMESTONES
mud
wacke
pack
grain
rud & bound
MUD
SAND
GRAVEL
clay
silt
vf
f
m
c
vc
gran
peb
cob
boul
SAMPLE
SED STRUCTURES
15.0
14.5
14.0
13.5
13.0
12.5
12.0
34
33
32
31
30
29
28
27
26
C
LCW - 11
LCW - 10
LCW - ASH 5
LCW - 9
Crossbedded unit w/ muddy lens channels
Erosive crossbedded unit w/ volcanic clasts
Coarsening upward sequence of silts to sands w/ vertical burrowing
Coarsening upward sequence of muds to silts w/ vertical burrowing
Blocky sands w/ sheet-like coarse layers & carbonate nodules
Blocky sands w/ carbonate nodules and 0.5 cm tephra bed
Blocky sands w/ sheet-like coarse layers & carbonate nodules
Thick bedded silts w/ apparent mud cracks
Abundant crossbedded sands w/ volcanic & tephra cobbles

SECTION
POLARITY
SCALE (m)
LITHOLOGY
LIMESTONES
mud
wacke
pack
grain
rud &
bound
MUD
SAND
GRAVEL
clay
silt
vf
f
m
c
vc
gran
peb
cob
boul
SAMPLE
SED STRUCTURES
26
25
24
23
22
21
20
12.0
11.5
11.0
10.5
10.0
9.5
9.0
LCW - 8
LCW - ASH 4
LCW - ASH 3
LCW - 7
LCW - 6
Repeating pattern of sandy silts & blocky sands with muddy lens channels & abundant volcanic / tephra cobbles
Blocky sand w/ thin wavy tephra bed
Erosive basal contact w/ volcanic clasts followed by silt bed and blocky sandy unit w/ coarse, sandy, and muddy lens channels
Silts punctuated by blocky sand unit w/ coarse lens channels
Blocky sand w/ punctuated sheet-like pulses of coarse sediment
Large silt bed w/ coarse lens channels and volcanic cobbles
Wavy channel w/coarse lag

SECTION
POLARITY
SCALE (m)
LITHOLOGY
LIMESTONES
mud
wacke
pack
grain
rud &
bound
MUD
SAND
GRAVEL
clay
silt
vf
f
m
c
vc
gran
peb
cob
boul
SAMPLE
SED STRUCTURES
20
19
18
17
16
15
14
13
12
11
9.0
8.5
8.0
7.5
7.0
6.5
6.0
LCW - 5
LCW ASH - 1
LCW ASH - 2
Volcanic cobbles
Erosive wavy contact w/ coarse lag
Wavy bedded unit w/ wavy coarse gradded channel and a large mud filled channel
Blocky sands
Planar bedded silts
Erosive planar contact w/ gradded bedding
Mud lens & abundant vertical burrowing
Heavy fluvial crossbedding with gradded bedding, small tephra bed with detrital ash boulders
Vertical burrowing
Coarse lens channels w/ vertical burrowing

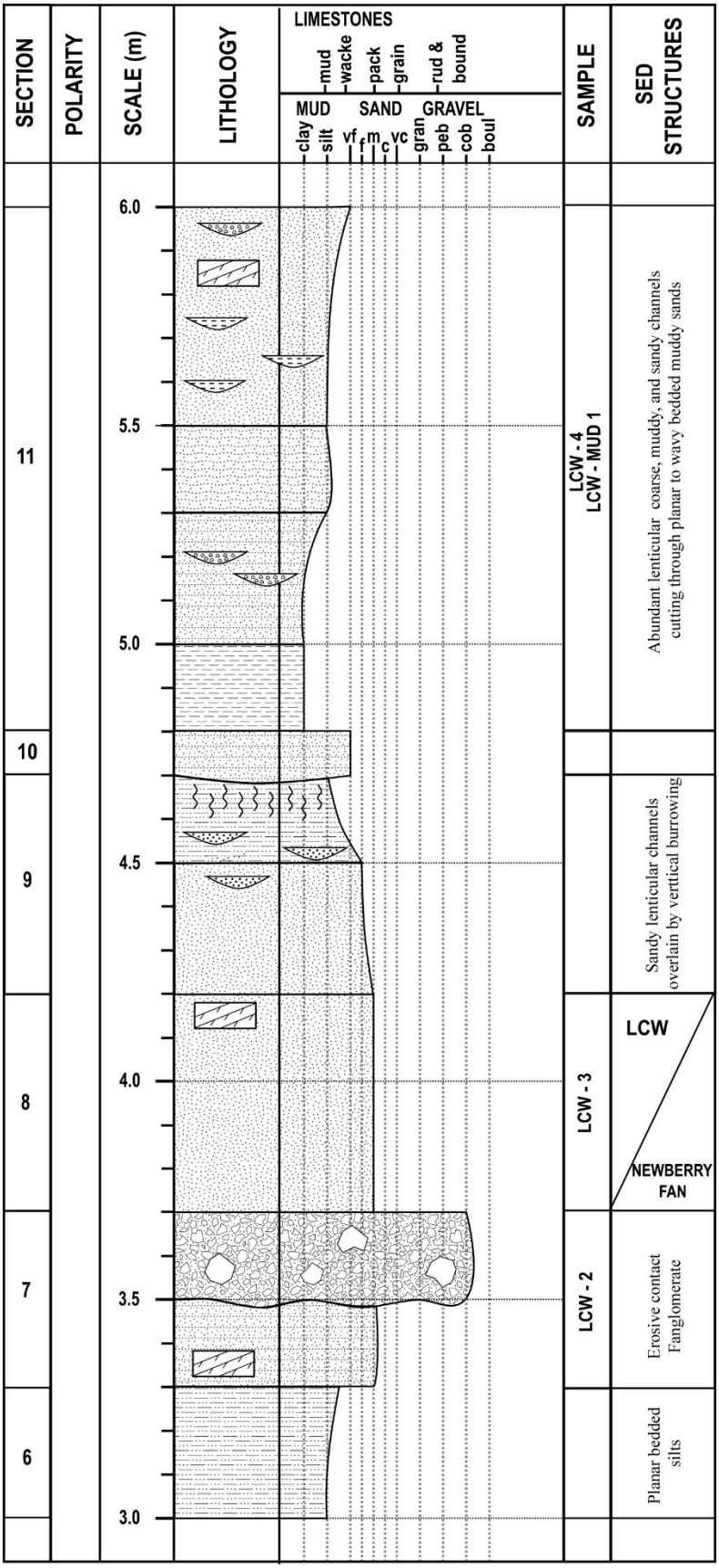
SECTION
POLARITY
SCALE (m)
LITHOLOGY
LIMESTONES
mud
wacke
pack
grain
rud &
bound
MUD
SAND
GRAVEL
clay
silt
vf
f
m
c
vc
gran
peb
cob
boul
SAMPLE
SED STRUCTURES
11
10
9
8
7
6
6.0
5.5
5.0
4.5
4.0
3.5
3.0
LCW - 4
LCW - MUD 1
Abundant lenticular coarse, muddy, and sandy channels cutting through planar to wavy bedded muddy sands
Sandy lenticular channels overlain by verttical burrowing
LCW - 3
LCW
NEWBERRY FAN
LCW - 2
Erosive contact
Fanglomerate
Planar bedded silts

SECTION
POLARITY
SCALE (m)
LITHOLOGY
LIMESTONES
mud
wacke
pack
grain
rud &
bound
MUD
SAND
GRAVEL
clay
silt
vf
f
m
c
vc
gran
peb
cob
boul
SAMPLE
SED STRUCTURES
5
4
3
2
1
3.0
2.5
2.0
1.5
1.0
0.5
0.0
LCW - 1
LCW - 0
Repeating Eining Upward Sequences
Eining Upward Sequence
Eining Upward Sequence
Erosive contact with fining upward grain size